Development and Simulation of a Cylindrical Cusped-Field Thruster and a Diagnostics Tool for Plasma-Materials Interactions

by

Anthony Pang

B.E., Mechanical Engineering, The City College of the City University of New York (2011)

Submitted to the Department of Aeronautics and Astronautics
in partial fulfillment of the requirements for the degree of

Master of Science in Aeronautics and Astronautics

at the

MASSACHUSETTS INSTITUTE OF TECHNOLOGY

June 2013

Author ....
Department of Aeronautics and Astronautics
23 May 2013

Certified by ....
Manuel Martinez-Sanchez
Professor of Aeronautics and Astronautics
Thesis Supervisor

Accepted by ....
Eytan H. Modiano
Professor of Aeronautics and Astronautics
Chair, Graduate Program Committee

Development and Simulation of a Cylindrical Cusped-Field Thruster and a Diagnostics Tool for Plasma-Materials Interactions

by

Anthony Pang

Submitted to the Department of Aeronautics and Astronautics
on 23 May 2013, in partial fulfillment of the
requirements for the degree of
Master of Science in Aeronautics and Astronautics

Abstract

A low power, Hall-effect type plasma thruster known as the MIT-Cylindrical Cusped-Field Thruster (MIT-CCFT) has been developed and simulated using a fully-kinetic plasma model, the Plasma Thruster particle-in-cell (PTpic) model. Similar to the Diverging Cusped-Field Thruster (DCFT) previously developed in the Massachusetts Institute of Technology Space Propulsion Laboratory, this thruster uses cusped magnetic fields aligned in alternating polarity in order to confine electrons, thus slowing their flow to the anode and readily ionizing neutral gas, which is then electrostatically accelerated by the anode. The design methodology for the CCFT will be discussed, with significant emphasis on the effects of magnetic topology on thruster performance. In particular, while the topology is similar to that of the DCFT in that it also confines the discharge plasma away from the channel walls to limit wall erosion, the CCFT was also designed to minimize plume divergence.

To predict the CCFTs performance and plasma dynamics, the design has been modeled and simulated with PTpic. From multiple simulations of the CCFT under different operating conditions, the thruster performance and plume characteristics were found and compared to past simulations of the DCFT. Specifically, the predicted nominal total efficiency ranged from 25 to 35 percent, providing 4-9 mN of thrust at a fixed xenon mass flow rate of 4.0 sccm, whilst consuming 90-400 W of power and with a corresponding nominal specific impulse of 1050 to 1800 s. Preliminary observations of the particle moments suggest that the magnetic confinement of the plasma isolates erosion of the channel walls of the discharge chamber to the ring cusps locations. In addition, in contrast to the DCFT, the CCFT does not have a hollow conic plume; instead, its beam profile is similar to that of traditional Hall-effect thrusters.

To supplement the efforts for optimizing longevity of the cusped-field thruster, a new diagnostic tool for erosion studies, novel to the electric propulsion community, has been implemented and has undergone preliminary validation. Ion beam analysis (IBA) allows for in-situ measurements of both composition and profile of the surfaces of the discharge region of a plasma thruster during operation. The technique has been independently tested on individual coupons with the use of the Cambridge Laboratory for Accelerator Study of Surfaces (CLASS) tandem ion accelerator. The coupons, which are composed of materials with known sputtering rates and/or are commonly used as insulator material, are exposed to helicon-generated plasma to simulate the sputtering/re-deposition found in thruster discharge region. Through comparison of ion beam analysis traces taken before and after plasma exposure, the effective erosion rates were found and validated against simulated results.

Thesis Supervisor: Manuel Martinez-Sanchez
Title: Professor of Aeronautics and Astronautics

Acknowledgments

Logistically, this work was supported by the National Science Foundation through the NSF Graduate Research Fellowship Program and by the Air Force Office of Scientific Research.

However, even with fiscal support, the work presented in this thesis could not have been possible without significant contributions from countless colleagues, advisers, and friends. First, I want to thank Professor Martinez-Sanchez for offering me this challenging and exciting opportunity, and the leeway to pursue it. Without his mentorship and support, this academic adventure could have easily ended up a misadventure. I would also like to thank Professor Lozano for, among many other things, being one of the best instructors, in the lab and in the classroom, that I've ever had.

Other significant contributors to the successful completion of this thesis and the fruition of the CCFT include: Stephen Gildea, for teaching me everything I know about PTpic; Taylor Matlock, for giving me much of the inspiration and motivation for building the CCFT and teaching me everything I know about plasma thruster experimentation; Regina Sullivan, for giving me a crash-course on ion beam analysis, teaching me how to operate a particle accelerator in a week, and generally making Chapter 5 possible; Todd Billings, the MIT Aero/Astro technical instructor, and my UROPs, Dennis Prieto and William Waste, for helping me build the CCFT; and my primary Astrovac lab partners, Louis Boulanger and Jaume Caville, who help me convert a hunk of metal in the vacuum chamber into an operating cusped-field thruster.

I would also like to thank all of my friends and colleagues in the SPL. I drove you all crazy but you still gave me thoughtful discussions on space propulsion and you all showed up at the pig roast. Special thanks to: Louis and Carla, who had to put up with having me as an officemate for the last two years; Steve and Louis (again!), for valiantly trying to keep me fit twice a week; Fernando, for helping me remember Electric Circuits 101 at least one a week in the lab; and Tom, for always taking the time to answer all of my questions about the cluster and troubleshooting my computer/coding problems.

I would also like to thank my friends, GA^3 execs, and roommates for making my time in Cambridge memorable. In particular, I want to acknowledge Patrick, Simon, Wei, Hang, Jay, Luis, Pedro, and Dan Rothenberg, who kept me sane. There simply weren't enough Settler of Catan games, trivia games, Pirates of the Charles events, or IHOP trips but we'll remedy that someday.

Last, but not least, I dedicate the thesis to my loving parents, my grandparents, sister Xin, and brother-in-law Brandon. I've been blessed with a family who taught me the value of education and have never wavered in supporting me, no matter where my dreams take me.

Contents

List of Figures

List of Tables

Chapter 1

Introduction

In-space propulsion has traditionally been dichotomized into broad categories: chemical propulsion and electric propulsion. Generally, these two types of propulsion have been utilized in distinct theaters of space missions. Through harvesting the chemical energy of its propellants and at the cost of specific impulse, chemical thrusters are able to create high enough levels of thrust (newton to kilo-newton) to perform missions which necessitate fast orbit and plane changes, and rapid orbital maneuvers. However, the lower specific impulse of these devices results in higher propellant mass, which could add significant costs to the mission.

Electric propulsion devices generate thrust via the use of electric energy to accelerate the propellant. In contrast, while most electric propulsion devices are generally incapable of generating thrusts exceeding 1 N, they possess specific impulses significantly higher than those found in chemical propulsion (thousands of seconds, opposed to the low hundreds found in typical chemical devices such as monopropellants, bipropellants, and cold-gas thrusters). Specific impulse can be defined as the relationship between thrust and the amount of propellant used per unit time, and represented in the following equation:

$$I_{sp} = \frac{T}{g\dot{m}} \tag{1.1}$$

where T is the thrust, g is the gravitational acceleration of the Earth, and $\dot{m}$

is the mass flow rate of the propellant. From this ratio, it is apparent that high specific impulse results in relatively high thrust obtained with low fuel consumption. Currently, there are many missions, such as deep space missions and long-term drag cancellation for geostationary satellites, which require high specific impulse (> 1000 seconds) due to a high ΔV requirement for their long duration. In addition, for missions without time constraints, electric propulsion can be used to perform station-keeping for remote sensing or telecommunication satellites, slow orbital maneuvering, plane changing, and orbit raising [3].

1.1 Hall-effect Thrusters

Hall-effect thrusters, which were first developed in the Soviet Union in the early 1960's, consist of a cathode-anode pairing where electrons traveling from the externally mounted cathode to the high potential anode are impeded by a radial magnetic field. The magnetic field, applied with electromagnetic coils, is strong enough (O[100 Gauss]) to trap the electrons within their gyroradii. Electrons also experience an $E \times B$ drift, which creates a Hall current:

$$\vec{j}_{Hall} = en_e \frac{\vec{E} \times \vec{B}}{B^2} \tag{1.2}$$

These electrons drift azimuthally and, through collisions with injected neutral propellant, create ions, which are electrostatically accelerated out of the chamber and neutralized by other electrons emitted from the cathode. Though Hall thrusters are electrostatic accelerators, the reaction force felt by the structure is not electrostatic but magnetic, through the Hall current. A schematic of a Hall-effect thruster can be seen in Figure 1-1.

The ions are electrostatically accelerated to an exit velocity,

$$v_i = \sqrt{\frac{2e\phi}{m_i}} \tag{1.3}$$

where ϕ is the potential at the location of ionization. This is the cause of the

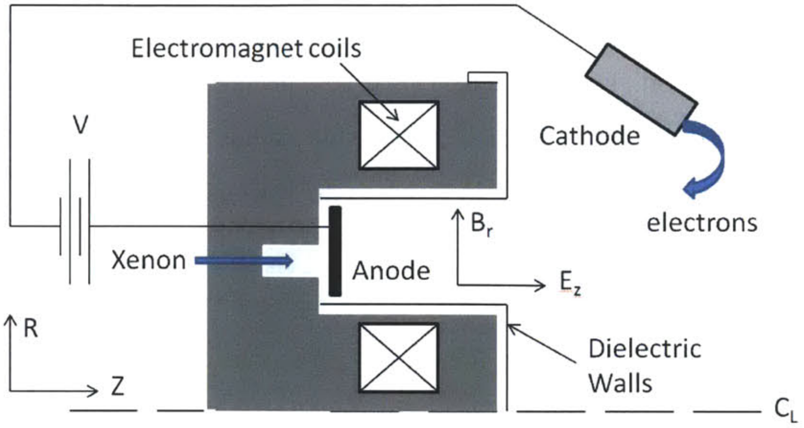

Figure 1-1: Hall-effect Thruster Schematic.

higher thrust density Hall thrusters have compared to ion engines, as Hall thrusters are not space-charge limited given the quasineutrality of the plasma in the discharge region. As a result of their higher thrust density and the high reliability (100% success rate in over 200 missions in orbit), Hall thrusters are now increasingly studied and adapted by industry for in-space propulsion. The emphasis of the current research has been devoted toward improving thruster efficiency and extending the lifetime of the devices. Toward those ends, improvements and modifications to low power Hall thruster designs in recent years have included incorporation of high power permanent magnets and adaptation of cusped magnetic topology. The adaptation of these techniques at the Massachusetts Institute of Technology has led to the development of the Diverging Cusped-Field Thruster [1] and, with continuing refinement, the Cylindrical Cusped-Field Thruster. The effects of these modifications and their incorporation into the Cylindrical Cusped-Field Thruster design will be discussed in detail in the following chapter.

1.2 Plasma-Surface Interactions and Thruster Longevity

Unfortunately, in addition to propellant capacity, the longevity of any mission using electric propulsion is also limited to the lifetime of these devices. In particular, plasma sputtering of the dielectric chamber walls of the discharge region of plasma thrusters is a primary life-limiting mechanism for long term satellite station-keeping and long-range space exploration. For Hall-effect thrusters in particular, failure can be defined as soft failure, which is when the dielectric insulator has been eroded to the magnetic circuit and would eventually lead to damage to the electromagnetic coils and thus results in thruster inoperation.

Table 1.1 [7] shows that soft failure severely limits thruster applicability for long missions, rather than the predicted lifetime. In order to address this issue, the primary source of erosion which causes the soft failure, particle sputtering from the plasma, must be investigated.

Table 1.1: Lifetimes of Commercial Hall-effect Thrusters

Thruster Designation	**Anode Power [W]**	**Anode Efficiency**	**Soft-Failure Time [h]**	**Predicted Lifetime [h]**
SPT-50	320	47 %	>2,500	-
KM-45	310	40-50%	3,500-4,000	-
KM-32	200	30-40%	2,000-3,000	3,000
BHT-200	200	43.5%	1,287-1,519	>1,700
HT-100	175	25%	300	1,500
SPT-30	150	26%	600	-
SPT-20M	<100	<38%	594-910	4,000

In particular, the sputtering of boron nitride (BN) is an especially critical topic due to its widespread use as as insulator wall material in Stationary Plasma Thruster (SPT) type Hall thrusters. Furthermore, deposition of the sputtered BN can contaminate spacecraft surfaces (e.g. solar panels or thermal control surfaces), which makes it a priority to better understand its erosion mechanisms. For plasma thrusters in general, wall degradation tends to be concentrated heavily in certain areas. For Hall thrusters, sputtering-induced erosion concentrates at the exit channel lips, because that is the area where the majority of ionization occurs.

However, while there have been resources spent towards finding the sputtering yield and other material characteristics of boron nitride due to its heritage, there has not been efforts toward developing general material diagnostic tools for studying, on a

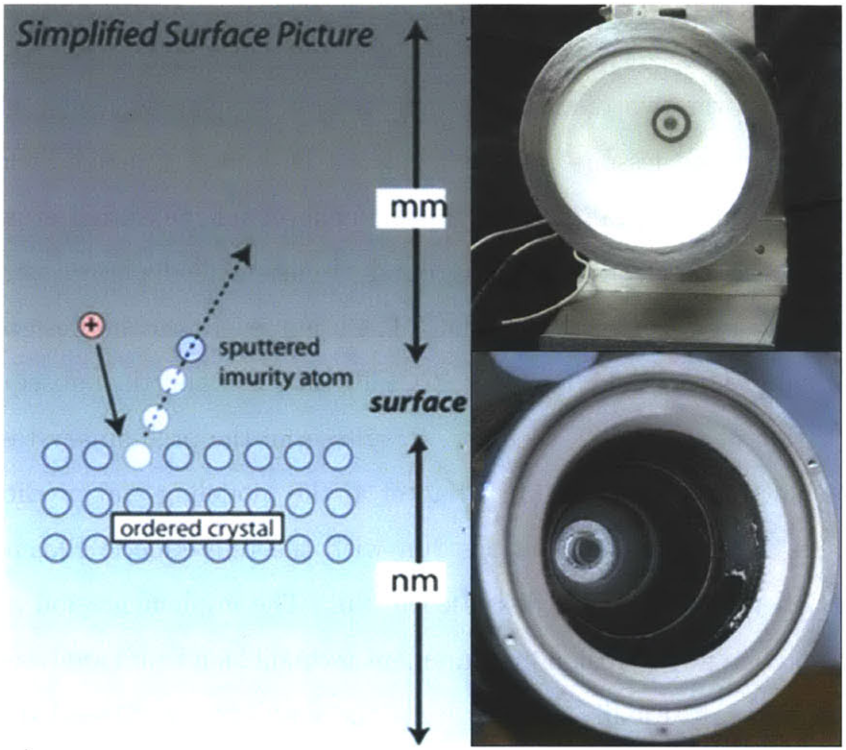

Figure 1-2: Sputtering Schematic (left) [8], Visual Display of Insulator Cone of the Diverging Cusped-Field Thruster, before and after erosion (right) [7]

fundamental level, the interactions between materials and plasmas. The current tools used in the electric propulsion community for investigating erosion are problematic in that they usually neccesitate the dismantling of the propulsion device, are extremely time consuming, and are limited for in-situ measurements. With the increasing sophistication of materials science and the subsequent advent of many new materials which could outperform boron nitride, there is a need for an expedient means of determining the adaptability of said materials to thruster use. To fulfill this need, ion beam analysis, an analytical technique commonly used in materials science but hitherto less commonly used in the propulsion community, has been employed and its applicability is further explored in this thesis.

1.3 Research Overview

This thesis will cover two discrete research topics: developing a new electrostatic thruster based on the lessons learned from the Diverging Cusped Field Thruster (DCFT), and testing and validating a novel technique for measuring erosion. Chapter 2 of this thesis describes the background of cusped field plasma thrusters, the development and performance of the DCFT, its influences on the design criteria of the Cylindrical Cusped-Field Thruster (CCFT) thruster, and the subsequent design and construction of the CCFT thruster. Results from the preliminary testing of the CCFT are shown in Chapter 3. In Chapter 4, the modeling and predicted performance of the CCFT from simulations run with the fully-kinetic Plasma Thruster Particle-in-Cell (PTpic) code is discussed in full. The implementation and preliminary validation of a novel erosion measurement technqie, ion beam analysis, is covered in depth in Chapter 5. Finally, a summary of the work and recommended future work is provided in Chapter 6.

Chapter 2

The MIT Cylindrical Cusped-Field Thruster Overview

2.1 Background: Cusped-Field Thrusters

In Chapter 1, the basic principles of Hall-effect thrusters were discussed. While Hall thrusters have certain advantages over other plasma thrusters, such as thrust density compared to ion engines, there are a few limitations. Due to electron confinement within radial magnetic fields which intercept thruster inner walls, there is a resulting flux of electrons to the dielectric insulators and a subsequent formation of a sheath. This sheath induces an ion flux, which could lead to ion recombination at the wall, radial ion acceleration within the discharge, and sputtering of the inner dielectric surfaces. These effects negatively impact the performance and, in the case of sputtering, severely limit the longevity of Hall thrusters. In fact, it is the erosion of the inner dielectric walls of the Hall thrusters which leads to exposure and subsequent damange to the magnetic circuit, which will be termed soft failure.

To address this problem, efforts have been devoted toward redesigning the magnetic configuration of the Hall thrusters for alternate means of electron confinement. As a result, the Cusped-Field thruster class was developed as a concept that has similarities to the general family of Hall devices but is clearly distinguished by the use of magnetic cusps for electron confinement. In these cusps, electrons are magnetically mirrored and, as such, are limited in their flux to the wall. While the magnetic field near the cusps is radial and contributes to the eponymous azimuthal Hall currents, the electrons are repelled from the cusps due to the high gradient of the magnetic field at their location. To illustrate this magnetic mirroring effect, the contributing repulsive force is shown in Equation 2.1:

$$F_{||} = -\frac{m_e v_\perp^2}{2B} \nabla_{||} B \tag{2.1}$$

where B is the magnetic field strength, $v_\perp$ is the perpendicular velocity to the wall, $\nabla_{||}$ is the gradient of the magnetic field parallel to the wall, and m_e is the mass of the electron. From conservation of the magnetic moment and total electron energy, the electrons entering an area of high magnetic gradient (e.g. the cusps) must increase their perpendicular energy whilst diminishing their parallel energy, thus reflecting the electrons away, as shown in Figure 2-1. If the electrons have sufficient parallel energy, they can overcome the magnetic bottling and collide with the surface. However, the resulting electron flux is significantly lower than the flux found in a standard radial magnetic field.

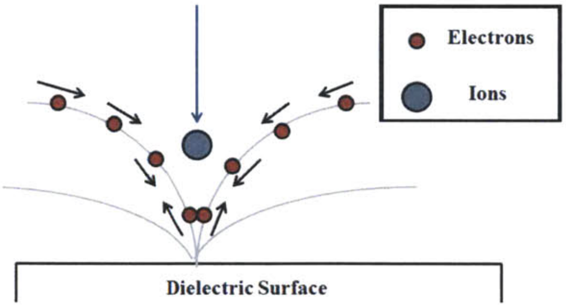

Figure 2-1: Magnetic mirroring of electrons in a cusped-magnetic field. Note the incident ion attracted to the cusp, where there is a sheath from the electron flux on the wall.

Away from the cusps, the magnetic field is mainly parallel to the surface and electron mobility across field lines is facilitated by collisions in the radial direction and anomalous diffusion, but it remains very small. As such, the overall electron flux away from the cusps is negligible and the resulting sheath potential will not be strong enough to attract the detrimental ion flux to the wall.

Among the designs that employ the cusped-field magnetic design, the Princeton Cylindrical Hall Thruster (CHT) [24] and the Thales High Efficiency Multistage Plasma Thruster (HEMPT) [4] have served as a motivation for initial designs of the Diverging Cusped-Field Thruster (schematics shown in Figures 2-2 and 2-3). A detailed comparison between the DCFT design, and the CHT and HEMPT has been documented by Courtney [1].

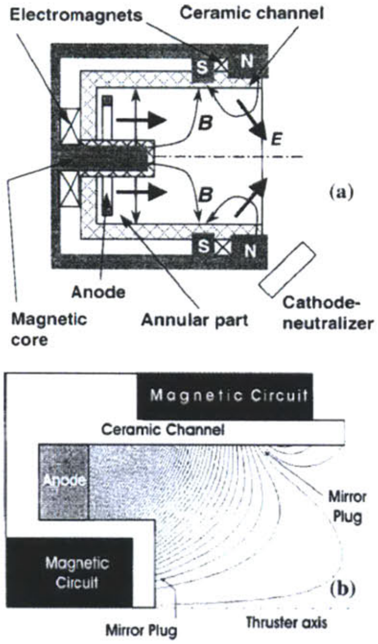

Figure 2-2: Schematic of the Princeton Cylindrical Hall Thruster (top), CHT magnetic circuit and field lines (bottom). [24]

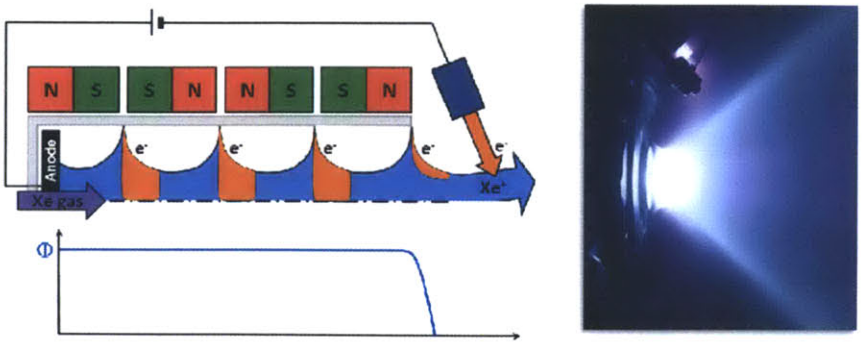

Figure 2-3: Schematic of the Thales HEMPT and potential plot (left), HEMPT plasma plume (right). [4]

2.2 The Diverging Cusped-Field Thruster

The DCFT, developed by Daniel Courtney in 2006, incorporates a cusped-field magnetic topology, as described above, to extend the thruster's longevity. One key difference between the DCFT and the traditional Hall-effect thruster is the use of Samarium Cobalt 3212 permanent magnets for the magnetic circuit. These magnets, which are arranged in an alternating polarity configuration shown in Figure 2-4, have stronger magnetic field strength (0.5 T) compared to traditional electromagnets (0.01 T) while using far less volume and with no need for additional power.

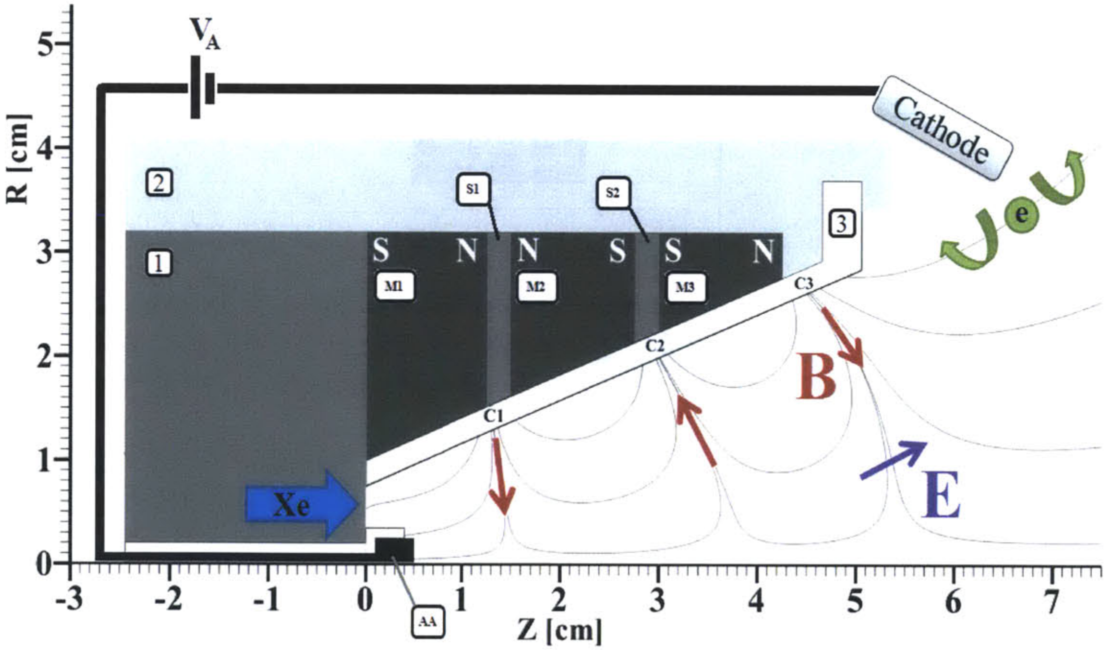

Figure 2-4: Cross-sectional schematic of the diverging cusped-field thruster, with overlayed magnetic field lines. [7]

As explained in the prior section, the alternating-polarity configuration creates cusps between each layer of magnets, which are the locations of localized electron flux. As such, these are also the primary locations of erosion for the DCFT. An erosion measurement study [7], was performed for the DCFT at the Air Force Research Laboratory. In the study, the DCFT fired continuously for 204 hours in high current mode (which will be discussed in the following subsection) and the boron nitride insulator cone's profile was taken before and after operation via a mechanical profilometer. The results, in Figure 2-5, reveal the main locations of erosion were at the three cusps, with minor erosion along the exit surface. It is also interesting to note that the location where maximum erosion took place is at the second cusp, where the electron flux to the wall is at its zenith and where it is believed that maximum ionization occurs.

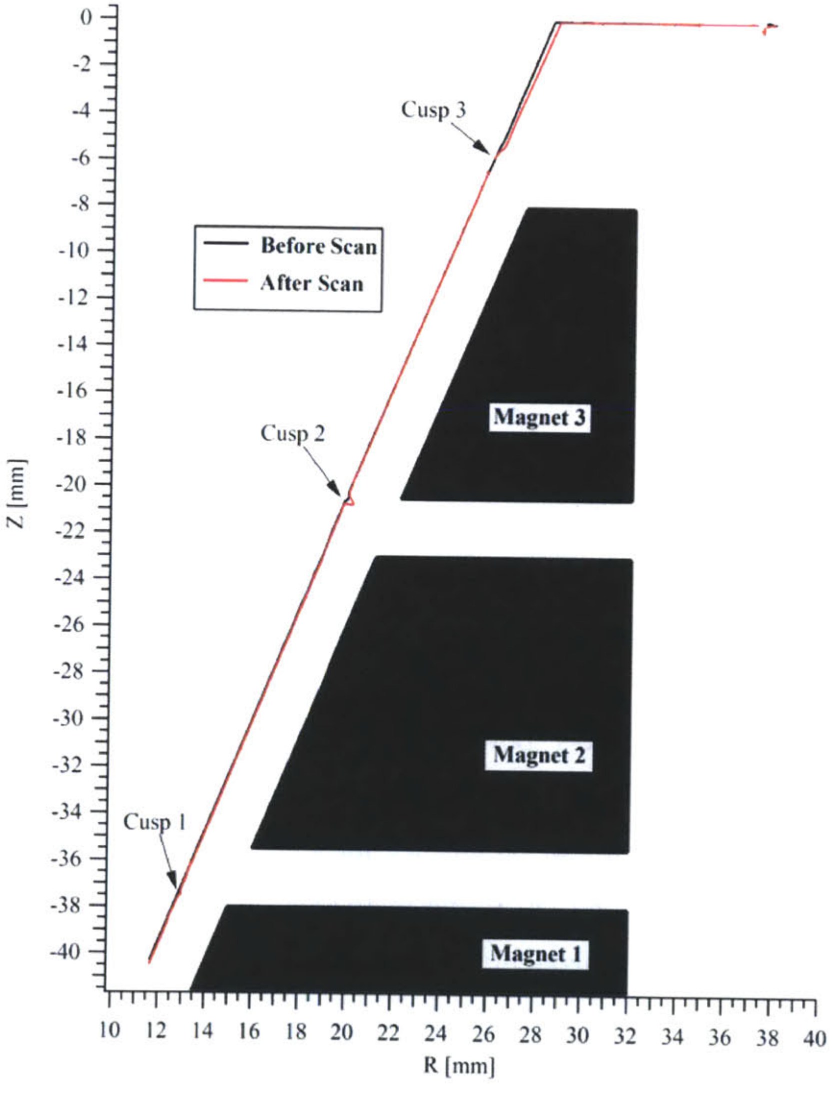

Figure 2-5: Erosion profile of DCFT Insulator Cone after 204 hr longevity experiment performed at the AFRL. [7]

Other key features of the DCFT include the removal of the central pole piece usually found in Hall thrusters and the incorporation of a divergent channel. In comparison to the annular discharge region of a traditional Hall thruster, the DCFT has a conically-hollow discharge region with a cylindrical anode at the upstream of the base. This design was made to eliminate any erosion which would have taken place in the annular center of the thruster, with the addiitonal reasoning that a diverging channel would also limit erosion on its walls near the exit. An additional benefit of the central pole piece modification includes the facilitatiion of miniaturization of the DCFT, as per the Princeton CHT.

With a peak anode thruster efficiency of 44%, thrust of 13.4 mN, and specific impulse of 1641 s while operating at an anode potential of 550 V and a flow rate of 8.5 sccm of Xenon [1], the performance of the DCFT is favorable when compared to commercial Hall thrusters operating at similar power and flow rate.

2.2.1 DCFT Drawbacks

However, there are a number of drawbacks with the DCFT. The foremost weakness of the DCFT is its divergent plume (shown in Figure 2-6), which has reduced thrust and efficiency when compared to a more collimated beam. The expanded plume may also cause damage, through sputtering and deposition, to other satellite components.

Also shown in Figure 2-6 are the bimodal operating modes of the DCFT: high-anode-current mode and low-anode-current mode. The two modes can be visually distinguished by the plume features. Both modes feature a divergence plume (at 37.5^{o}) and a hollow conical plume. The high-current mode is not desired as the increase in anode current is paired with lowered effiency for a given flow rate. Furthermore, it is hypothesized that the DCFT operating at the low-current mode experiences less erosion than operation in the high-current mode. Unfortunately, operating conditions for mode transition are occasionally difficult to predict and a "mixed" operating mode is often used, where characteristics of both modes are observed.

Last, the divergent channel of the DCFT causes decreased neutral density as propellant travels downstream. This negative gradient of neutral density will lower utilization efficiency if ionization occurs far downstream in the channel.

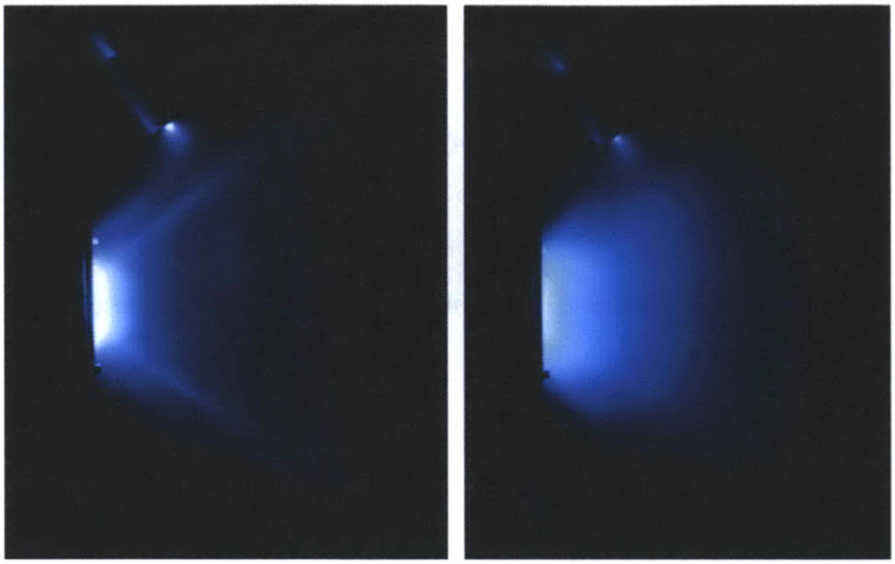

Figure 2-6: Hollow conical plume of the DCFT operating in high current mode (left), Plume of the DCFT operating in low current mode (right).

2.3 Cylindrical Cusped-Field Thruster Basic Design and Approach

To address the limitations of the DCFT, a new cusped-field thruster was designed. The criteria for the design are as follows:

- Magnetic field lines that begin out of the plume and end at the downstream cusps
- High field strength (>0.5 T) at the cusps
- Low field strength (<0.1 T) outside the mouth of the thruster
- Cylindrical discharge channel
- Flat downstream separatrix, to be discussed in Section 2.3.1
- Comparable discharge region size and number of cusps to the DCFT

These requirements not only fulfill various positive features of the DCFT but may also improve the performance. The first criterion was also used in the DCFT magnetic topology and facilitates electron travel from a cathode positioned well outside of the plume. The high field strength at the cusps is necessary for the magnetic mirroring of the electrons while the low field strength outside the mouth of the thruster would allow electrons to flow more readily into the channel. The change from a divergent discharge region to a cylindrical region would address the aforementioned issue of decreased neutral density. Last, by maintaining a similar discharge region volume and number of cusps as the DCFT, the effects of the other design changes can be more readily made visible.

2.3.1 Flat Exit Separatrix and Beam Divergence

The last design criterion was imposed to address the wide divergence of the DCFTs discharge plume. From previous studies of the divergence [Matlock, 2011], it was found that the ions were electrostatically accelerated out of the thruster perpendicular to the exit separatrix, which is the surface separating $\vec{B}$ lines that go to two different magnetic cusps. The various separatrices of the DCFT are highlighted in Figure 2-7.

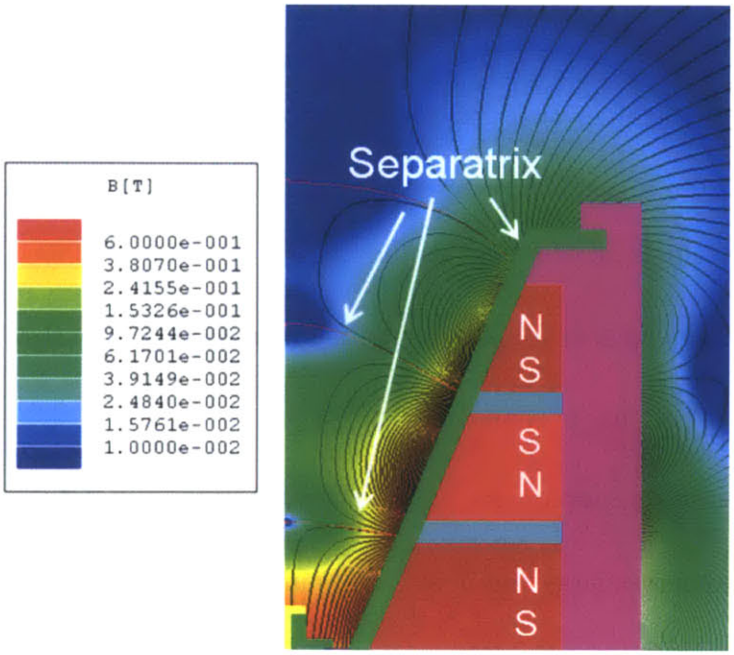

Figure 2-7: Magnetic topology, field lines and field strength of the DCFT, with the concave sepatrices noted.

Given the convexity of the DCFTs exit separatrix, the plume exiting the thruster would naturally be highly divergent. In an attempt to collimate the beam, Matlock et al experimented with the placement of a focusing electromagnet (operating at 20 A) at the exit of the thruster, as shown in Figure 2-8. In Figure 2-9, the use of the focusing electromagnet resulted in the thruster plume's divergence visibly decreasing from 37.5^o to 21.5^o.

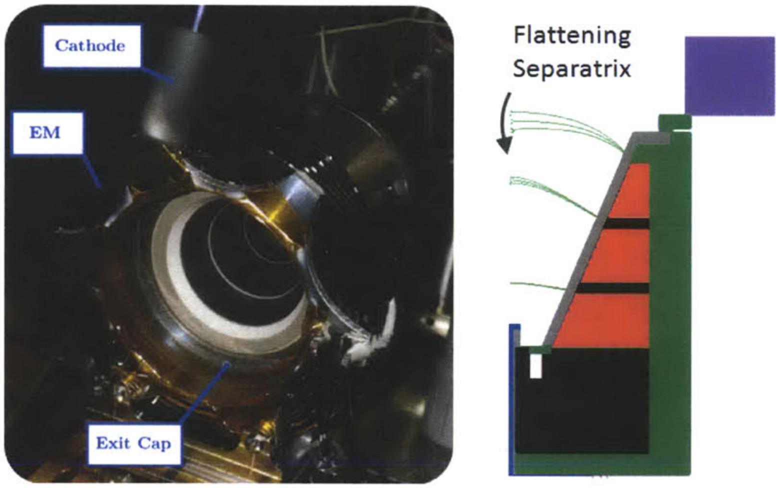

Figure 2-8: External electromagnet placed at end of DCFT (left), Simulated effect on separatrix from increased magnet current (right). [13]

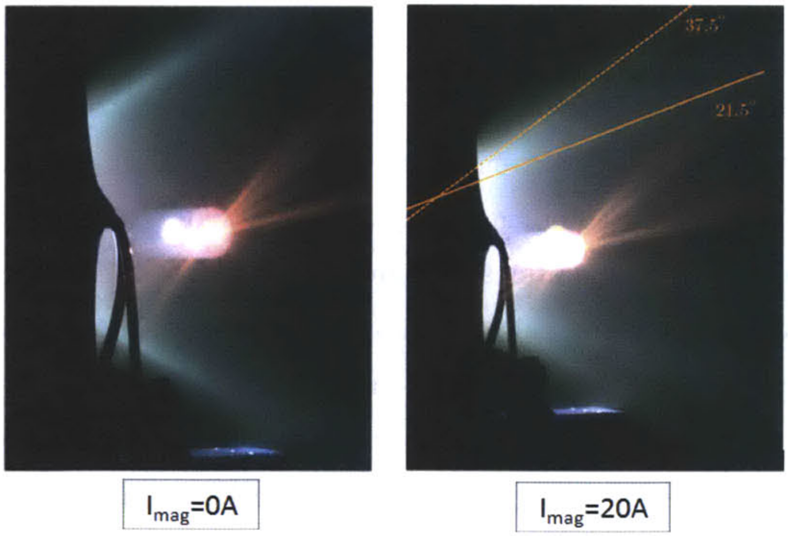

I_{mag}=0A

I_{mag}=20A

Figure 2-9: Plasma plume profile without applied electromagnet (left), Plasma plume profile with electromagnet (right). [20]

Thus, in order to collimate the beam, the planned design requires a powerful end focusing magnet to produce a flat exit separatrix plane. By placing a permannent magnet, which has higher field strength than the electromagnet, at the end of the magnetic circuit, the new thruster should produce a solid plume, akin to that of a Hall-effect thruster.

2.3.2 Magnetic Source Selection

Following the tradition of the diverging cusped-field thruster, Island Ceramic Grinding Magnetics Samarium-Cobalt 3212 rare-earth permanent magnets were selected for the design's magnetic source. While SmCo-3212 magnets do not possess fields as strong as neodymium magnets, they are used in cusped-field thruster designs because of their thermal properties. Given the relatively high temperatures (200^o C) typically encountered in the DCFT and other plasma thrusters, neodymium magnets would demagnetize after a period of thruster operation. In contrast, with SmCo-3212's maximum operating temperature of 300^o C, the CCFT can continuously fire without concerns about damage to the magnetic circuit.

2.3.3 Simulated CCFT Magnetic Field

With these requirements for the new design and chosen magnetic source, magnetic circuits for various cylindrical models were simulated. The simulation package used, Ansoft Maxwell SV, is an electromagnetic field finite element simulation software which was employed in the original design of the DCFT. The simulation employs an axisymmetric, 2D computational domain where geometric shapes are drawn and designated as magnetic material (samarium cobalt magnets, 1018 grade steel), dielectrics (boron nitride, alumina) or non-magnetic (aluminum, graphite). After imposing Dirichlet null boundary conditions at the boundaries, the magnetostatic solver will determine the resulting magnetic fields from the arrangement of these shapes in the magnetic circuit.

After an iterative process of designing and redesigning various magnetic circuits in order to produce a magnetic topology which would fulfill all of the design criteria, the Cylindrical Cusped-Field Thruster was developed.

As shown in the axisymmetric magnetic field plot in Figure 2-10, the magnetic topology of the CCFT features magnetic field lines which extend far outside of the exit, a cylindrical discharge channel with the same axial length and averaged radius of the DCFT, and, most importantly, a flat downstream separatrix. As with the Matlock studies, the flat separatrix was created through the placement of a permanent magnetic with alternate polarity at the end of the magnetic circuit.

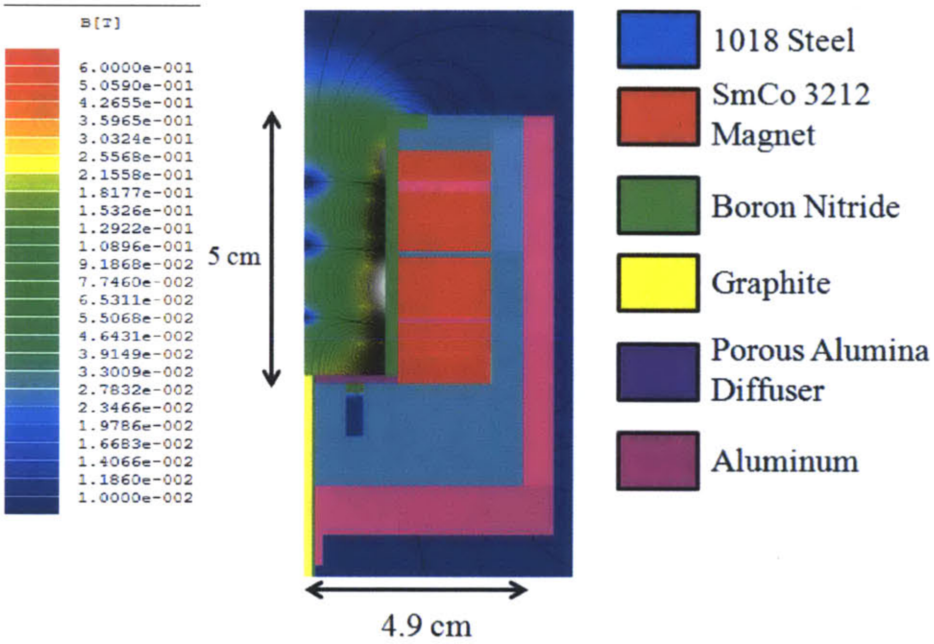

Figure 2-10: Magnetic field topology represented by magnetic flux lines within the cylindrical cusped-field thruster, in vacuum.

In addition, the high magnetic field strength at the cusps and relatively low field strength at the exit was also achieved, as displayed in Figure 2-11.

2.4 CCFT Thruster Design

Details of the MIT CCFT prototype are presented in this section, with machine drawings in Appendix A. Figure 2-12 displays the various components featured in the

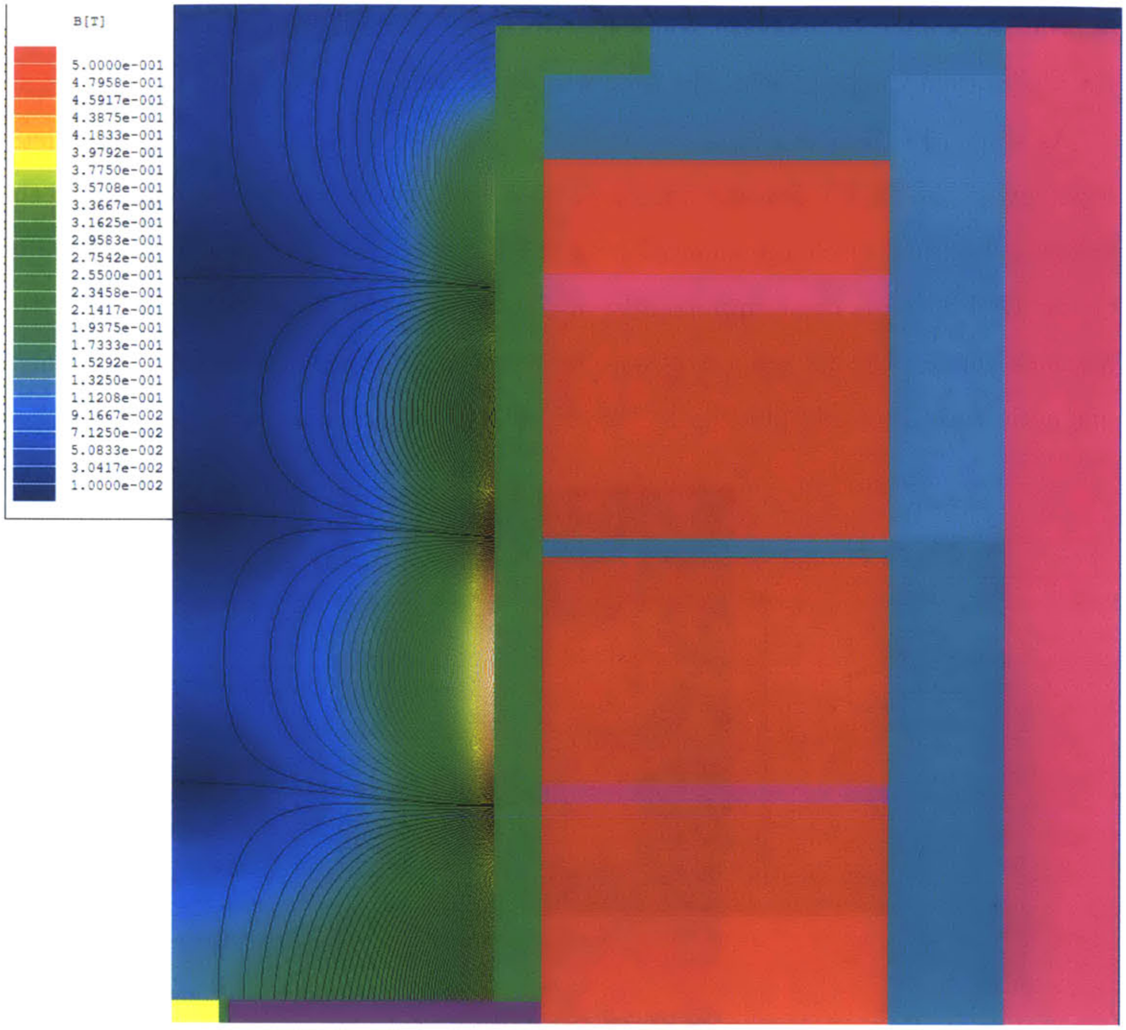

Figure 2-11: Simulated magnetic field strength within the CCFT, in vacuum.

finalized machine drawings of the CCFT in CAD form, with a corresponding bill of materials.

The following subsections will diskuss key design decisions for critical components of the CCFT not strictly affiliated with the magnetic design.

2.4.1 Dielectric Insulator Channel

The material used for the dielectric wall of the CCFT diskharge channel was High Purity (HP) grade boron nitride, purchased from Saint-Gobain Ceramics. The wall thickness of the cylindrical insert was 2.5 mm throughout the length of the thruster.

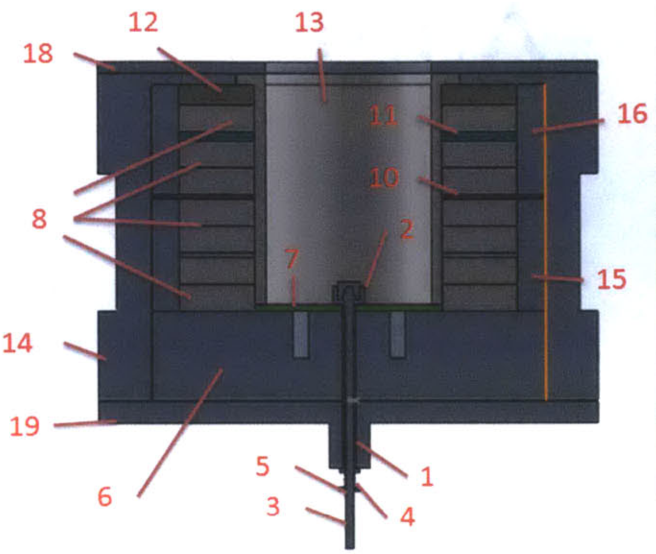

ITEM NO.	PART NUMBER	QTY.
1	Stem Sheath	1
2	Anode Insulator	1
3	Anode	1
4	Spring	1
5	Anode Hex Nut	1
6	Steel Base	1
7	Diffuser	1
8	SmCo3212 Magnet_new	7
9	Aluminum Spacer_new	1
10	Steel Ring_new	1
11	Aluminum Top_new	1
12	Steeltop_new	1
13	BN_new	1
14	Almn Shell	1
15	Steel Spacer_bottom	1
16	Steel Spacer_top	1
17	Anode Stem	1
18	Aluminum Cover Top	1
19	Aluminum Cover Bottom	1
20	Anode Washer	1

Figure 2-12: CAD cross section and bill of materials for the CCFT.

As with the DCFT, boron nitride was selected due to its ability to sustain high temperatures without becoming conductive and thermal conductivity to avoid thermal stress. As noted, it is also a heritage material frequently used in SPT-type Hall thrusters. The existing heritage with SPTs and the DCFT allows for direct comparisons between the erosion characteristics of the CCFT, of the DCFT, and traditional Hall thrusters. As with the DCFT, the dielectric insert was held loosely in place with an aluminum cap at the exit plane of the thruster, allowing for some axial expansion from possible thermal expansion during operation.

One key difference incorporated in the design of the CCFT insulator is segmentation of the boron nitride. By dividing up the boron nitride tube into smaller sections, the resulting shorter insulators now have an angle of attack for erosion measurements via ion beam analysis.

2.4.2 Anode Design and Propellant Inlet

For expediency and applicability to the design, surplus DCFT anode stock was used for the CCFT. The anode, composed of graphite due to its high electrical conductivity and excellent sputtering properties, is sheathed in boron nitride to prevent grounding

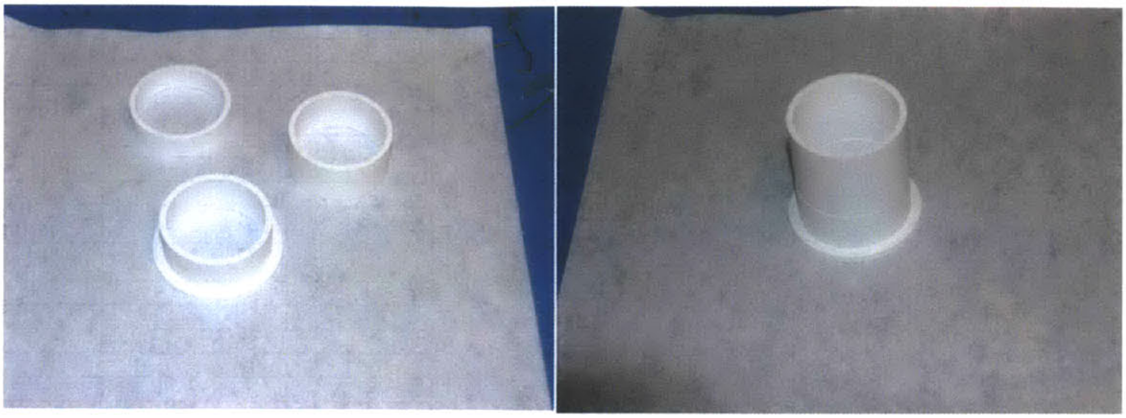

Figure 2-13: Boron nitride insulator components (left), Boron nitride insulator, in thruster configuration (right).

with the thruster body and inserted into the central cavity of the steel base at the furthest upstream section of the diskharge channel. At this point, the anode also helps secure the porous alumina diffuser disk. Additional details for the DCFT anode design can be found in diskussions about the original DCFT design.

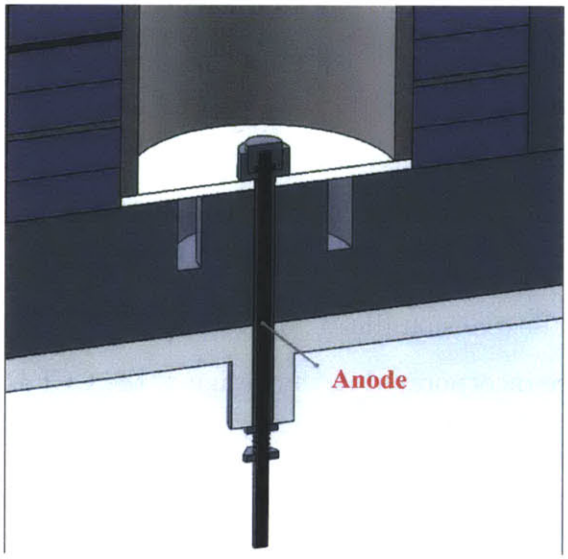

Figure 2-14: Cross section of the anode, with insulating sheath in the steel base.

The steel base, as shown in Figure 2-14, is also where propellant is fed into the thruster. The flow enters from an angled 316 stainless steel tube, welded at the rear of the thruster, into an annular region in the steel base, where it is stagnated by a porous alumina diffuser that distributes it diffused uniformly throughout the disk and, eventually, into the diskharge channel. Since flexibility was desirable in the installation of the diffuser disk and anode, there is a lack of a perfect seal in the feed system. The diffuser ring was simply set into an inscribed indentation in the steel base and held in place by oversized ceramic washers below the anode, as can be seen in Figure 2-14. As used in the DCFT, this arrangement facilitates changes and modifications to the diffuser without major disassembly of the thruster.

One major difference in the propellant inlet design transitioning from the DCFT to the CCFT is the use of porous alumina, rather than porous type 316 stainless steel for the diffuser disk. This decision was made due to observations of iron deposition on the DCFT insulator cone after hours of operation (as shown in Figure 2-15) is due to sputtering and subsequent redeposition of stainless steel from the diffuser disk.

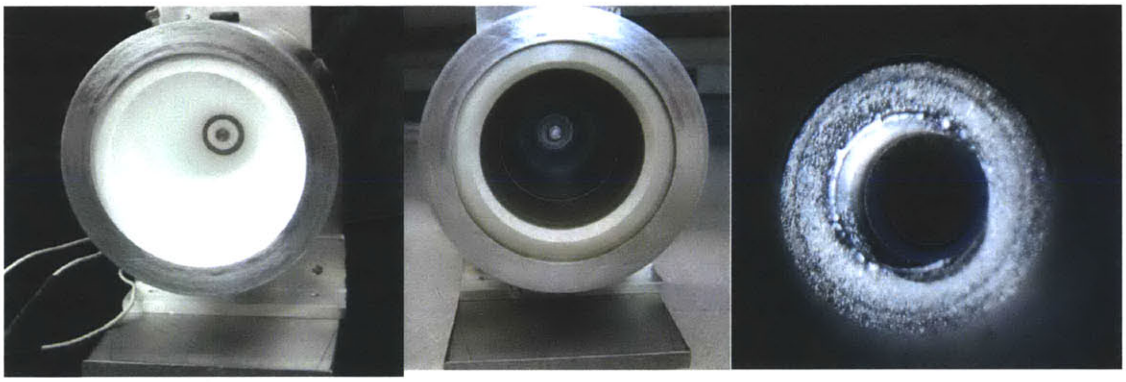

Figure 2-15: DCFT insulator prior to firing (left), DCFT insulator after firing (center), Eroded diffuser disk (right). [7]

2.5 Assembly

Due to the relatively high strength of the SmCo-3212 magnets used in the magnetic circuit, there are significant forces between the magnets, which renders assembly a difficult task. In the final arrangement, the repulsive force between the two largest magnets is estimated to be approximately 400N (determined using the Maxwell SV Field Calculator). A system for aligning and safely compressing the magnetic circuit is required for assembly of the thruster.

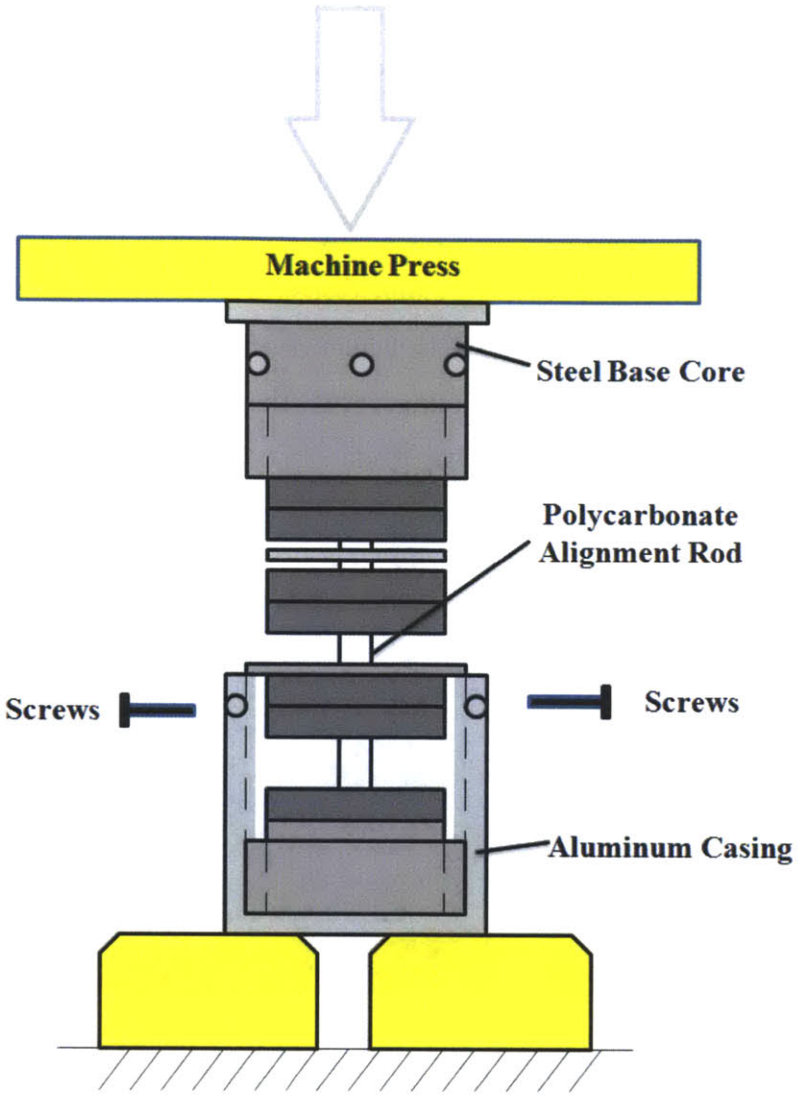

Figure 2-16: Schematics of assembly system for the CCFT.

The final design incorporates a polycarbonate rod which is used to align the various magnets and spacers, spaced apart due to the repulsive magnetic forces, collinearly with the aluminum casing. The casing is forced down with a machine press into contact with the steel base, with the magnetic circuit compressed into final thruster configuration. Once the thruster is in place and the press fixed in its location, the aluminum casing is screwed into the steel base core piece, which was modified to accommodate several large bolts, as well as the aluminum cover. With this arrangement the magnets and spacers are locked in place using bolts through the steel casing and into the base core. Once screwed in, the rod is removed from the magnets and, in its place, the porous alumina, ceramic tube insulator and anode are installed. Finally, the aluminum endcap piece is screwed in to secure the boron nitride insulator.

The completed thruster with hollow cathode neutralizer, ceramic wall insulation and test stand is shown in Figure 2-17.

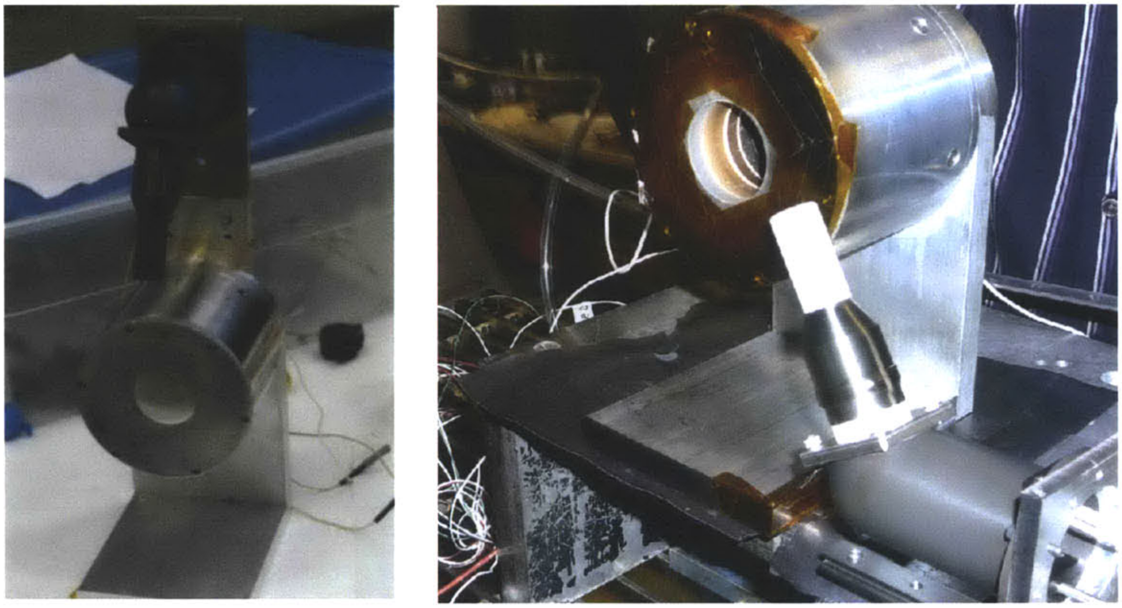

Figure 2-17: CCFT fully assembled, with Busek hollow cathode (left), CCFT in Astrovac with cathode on stage system (right).

2.6 Magnetic Field Measurements

Following the completed assembly of the thruster, an Alphalab DC magnetometer and Hall sensor were used to measure the radial magnetic field strength in the diskharge region of the thruster. These measurements were taken at the cusps and between the cusps along the diskharge wall. The results are shown in Table 2.1.

The results qualitatively and quantitatively match up closely with the Maxwell simulated radial magnetic field strengths, as shown in Figure 2-18. As such, it has been validated that the thruster has been built to design configuration and ready for preliminary testing.

Table 2.1: Measured Radial Magnetic Field Strength

Distance [cm]	Magnetic Field Strength [Gauss]
1.0	600
1.8	2870
2.5	800
3.0	3300
3.5	450
4.0	2800
4.5	800
5.15	300

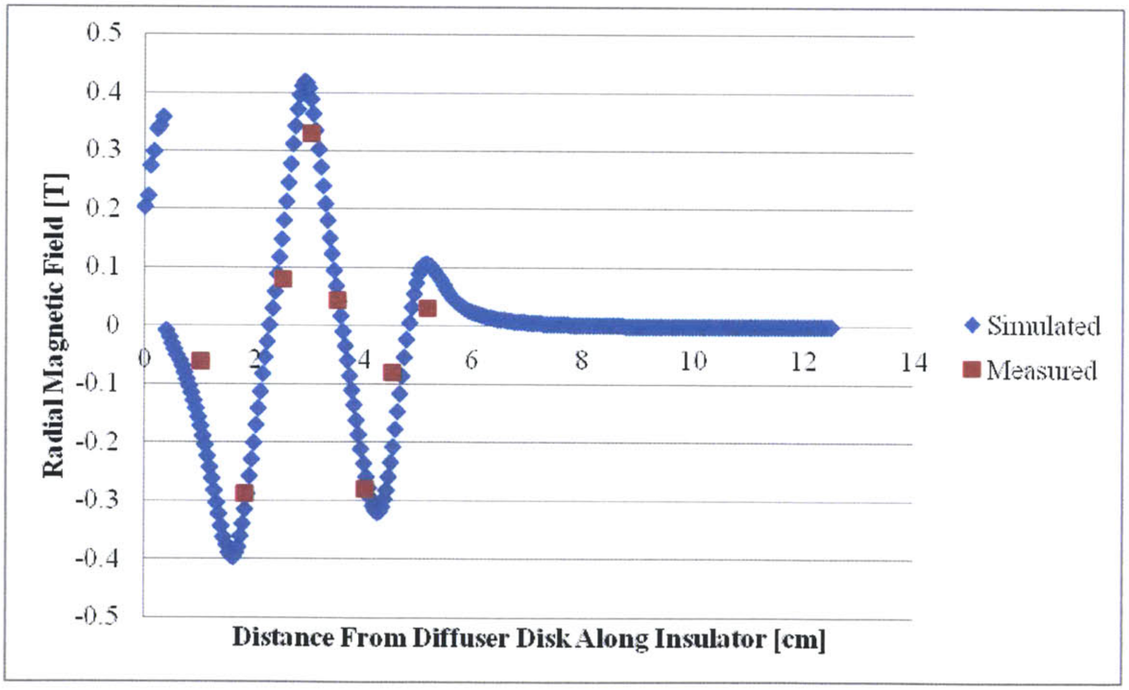

Figure 2-18: Simulated and measured radial magnetic field along boron nitride insulator.

Chapter 3

CCFT Preliminary Results and Performance

Following assembly, preliminary testing of the CCFT has been performed in the MIT Space Propulsion Laboratory. During the first discharge, voltage and current measurements and visual observations of the CCFT plasma plume were made. In this Chapter, the experimental setup and experimental facilities used for the first trials and results will be discussed in detail.

3.1 Experimental Setup

Figure 2-18 shows the setup was used in the CCFT experiments. As per most thruster performance tests, the thruster body was set at floating potential through the use of an insulator layer, which separated the thruster stand from the chamber, and flexible plastic tubing in the anode propellant line. Due to a lack of knowledge for the optimal cathode position, a cathode stage system was used. The cathode was placed on a 1-axis stage system, which fixed the cathode at an axial distance from the discharge region but allowed for radial traversing. During the first trials, the cathode was continuously repositioned and the resulting changes in the plume were recorded.

For the purposes of the simulation (discussed in Chapter 4), the floating body potential was also measured with a Fluke multimeter.

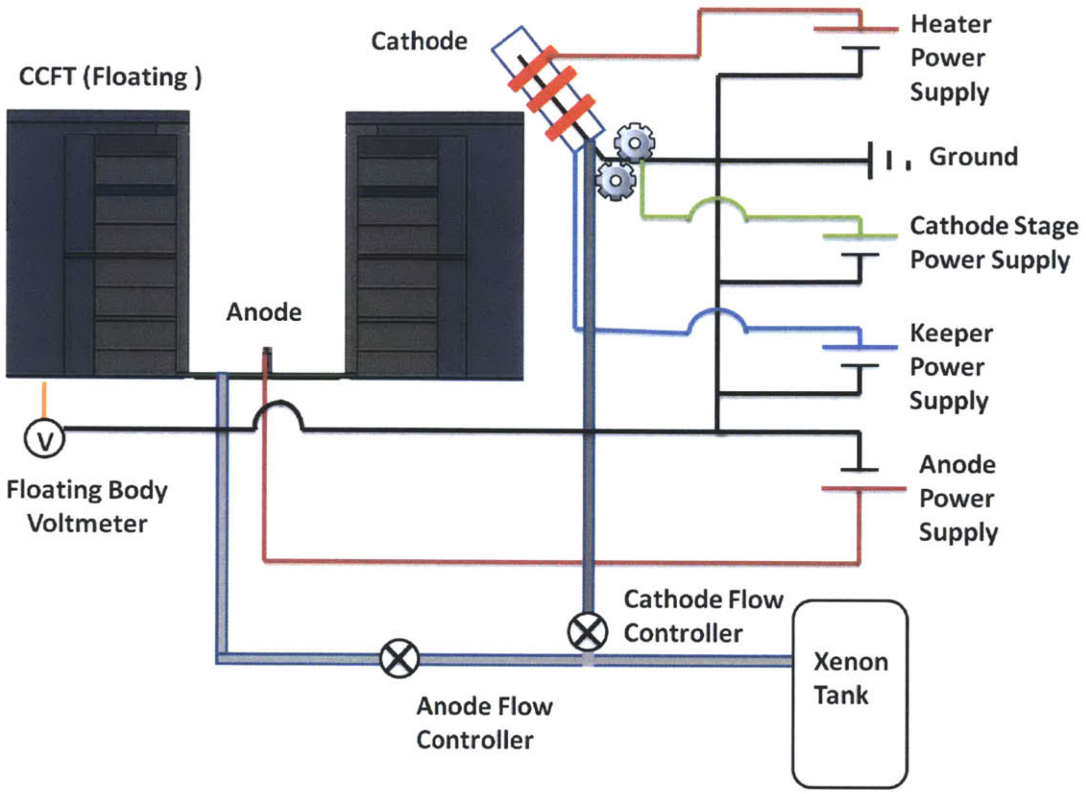

Figure 3-1: Sketch of the schematic of the experimental setup for the CCFT used at SPL.

3.2 Experimental Facility and Equipment

3.2.1 Astrovac

The MIT SPL vacuum facility (ASTROVAC) consists of a 1.5 m × 1.6 m cylindrical chamber equipped with a mechanical roughing pump and two cryopumps (CTI-Cryogenics CT10 and CTI-OB400 cryopumps), shown in Figure 2-19. The cryopumps used in tandem are capable of pumping out roughly 7500L/s of Xenon used. The pressure was monitored with a hot cathode gauge, which measured pressures maximized at 8.2×10^{-5} Torr while operating at a maximum flow rate of 7.5 sccm.

3.2.2 Cathode

The cathode used for the experiments is the Busek BHC-1500 hollow cathode, which is commonly used with the BHT-200 low-power Hall thruster and was used extensively

Figure 3-2: The Space Propulsion Laboratory Astrovac vacuum chamber. The chamber, used for the CCFT testing, is pumped by two cryopumps and one mechanical roughing pump.

for the DCFT. The cathode, which has a porous tungsten hollow insert impregnated with a low work function emitter comprised of a barium-calcium-aluminate mixture [14], ignites after using a co-axial tantalum swaged heater wire is heat the emitter to ignition temperature of approximately 1000 − 1200° C. The ignition is caused by a keeper, which is used to start the cathode and sustain an internal discharge before establishing thruster operation [14].

Figure 3-3: Busek BHC-1500 hollow cathode.

The aforementioned cathode conditioning process involves setting a flow of 2 sccm of Xenon through the cathode and initially setting the heater current at 2 A. After one half-hour, the heater current is increased to 4 A and, another half-hour after that, to 6 A. Five minutes after the heater current is set at 6 A, the cathode is ready to be fired. During normal operating conditions, the cathode operates with 1 sccm of Xe flow and 0.5A through roughly 20V to the keeper, with the heater circuit off.

3.2.3 Power Supplies

Two 1.5k W Agilent N5722A DC power supplies were to supply power to the anode and keeper and operate at a maximum voltage of 600 V and current of 2.6 A, which are more than enough for the required tests. To ignite the cathode and perform conditioning after exposing the cathoding to possible impurities, a HPJA1460PS DC power supply was used to heat the cathode.

3.2.4 Flow Controllers

The cathode and anode flows were regulated using two Omega FMA-A2400 flow controllers, which have been calibrated for Xenon flow and limited to a maximum flow of 10 sccm of Xenon. For all experiments, 99.999% high-purity Xenon gas was used for the anode and the cathode.

3.3 Preliminary Results from First Discharge and Stable Operation

3.3.1 Visual Observations of the Plume

The first discharge of the CCFT occurred with low power (100 V on the anode) and a low flow rate (4 sccm). With an increase in anode voltage, the plume became brighter, with a pronounced solidity along the centerline of the discharge. In both cases, the plume was widely divergent at approximately 45^o, as seen in Figure 3-4.

Figure 3-4: The CCFT firing with 4 sccm Xe flow and 100 V at the anode (left), CCFT firing with 4 sccm Xe flow and 200 V at the anode (right).

While the operations are stable within these operating conditions, an increase of anode voltage to above 350 V led to significant arcing between the thruster endcap and the cathode. To mitigate this arcing, the surface of the CCFT endcap was covered in Kapton insulating tape, as seen in Figure 3-5.

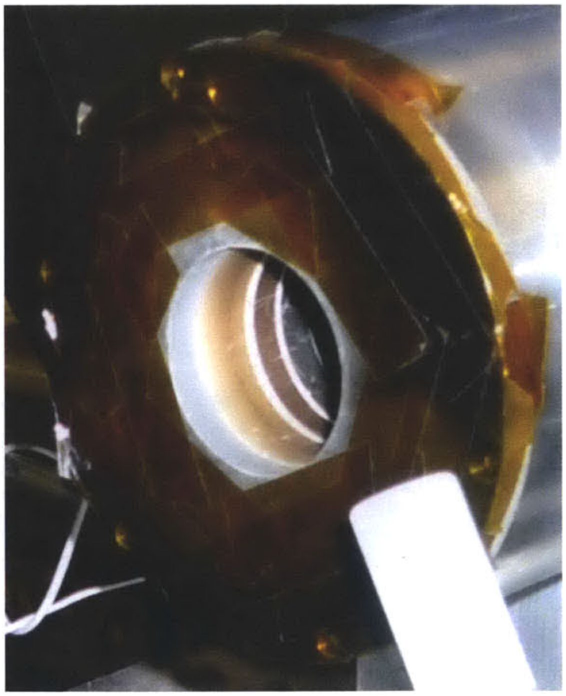

Figure 3-5: Endcap of the CCFT coated with Kapton tape.

With the new thruster configuration, the CCFT was again operated at the same conditions. As a result of the new insulation, the amount of arcing decreased drastically and the plume shape itself has changed. At the same flow rate and potential of 4 sccm Xe and 200 V, the new plume, shown in Figure 3-6, is now far more collimated, with a minor divergence of 15^o, in comparison to the 45^o beam seen in Figure 3-5.

Figure 3-6: The CCFT firing with 4 sccm Xe flow and 200 V at the anode.

Increasing the anode potential even further, there appears to be further changes to the plume. In Figure 3-7, there seems to be two plumes emitted from the CCFT: a solid, Hall thruster type beam, with a lower density, divergent (15^o) plume around it.

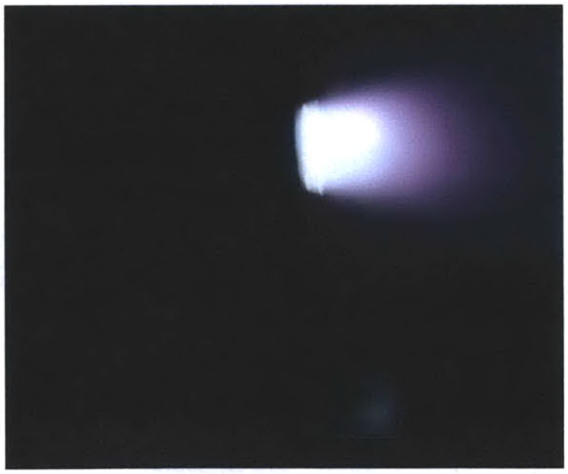

Figure 3-7: The CCFT firing with 4 sccm Xe flow and 300 V at the anode.

3.3.2 Anode Voltage and Flow Scans

With stable operations, the effects of flow rate and anode voltage were explored with flow and voltage scans. The results of these scans can be found in Figure 3-8, Figure 3-9, and Figure 3-10.

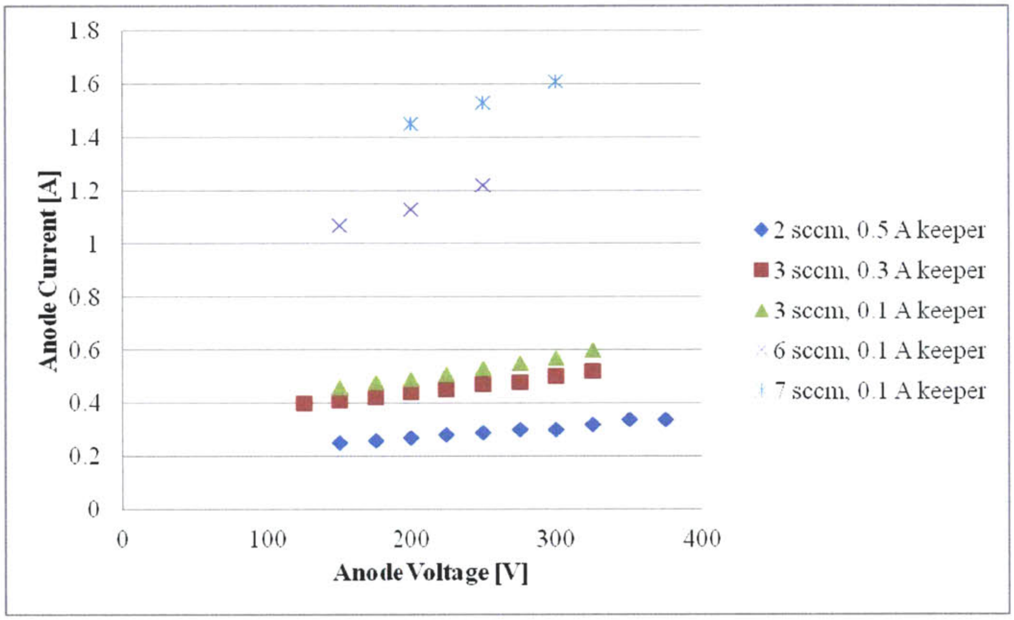

Figure 3-8: Anode voltage scan, with different keeper conditions. For reference, the complete ionization of 1 sccm Xe is equivalent to 0.0718 A of current, assuming single ionization. With double ionization, the current would be 0.144 A.

For the voltage scans, the range of voltages were from 100-375 V, with fixed flow rates at 2 sccm, 3 sccm, 6 sccm, and 7 sccm. During the voltage scan, the keeper current was diminshed to presumably decrease the current experienced at the anode. For the flow scan, the anode voltage was fixed and 150 V and 200 V, with flow ranging from 2-7 sccm Xe. The voltage did not exceed 375 V because of possible overheating of the anode, and the flow rate was limited due to caution about overly high operating pressures in the chamber.

3.3.3 Anode Current

The critical issue to note is the anode currents, which are higher than the currents found with the DCFT with the same operating conditions, as shown in Figure 3-11

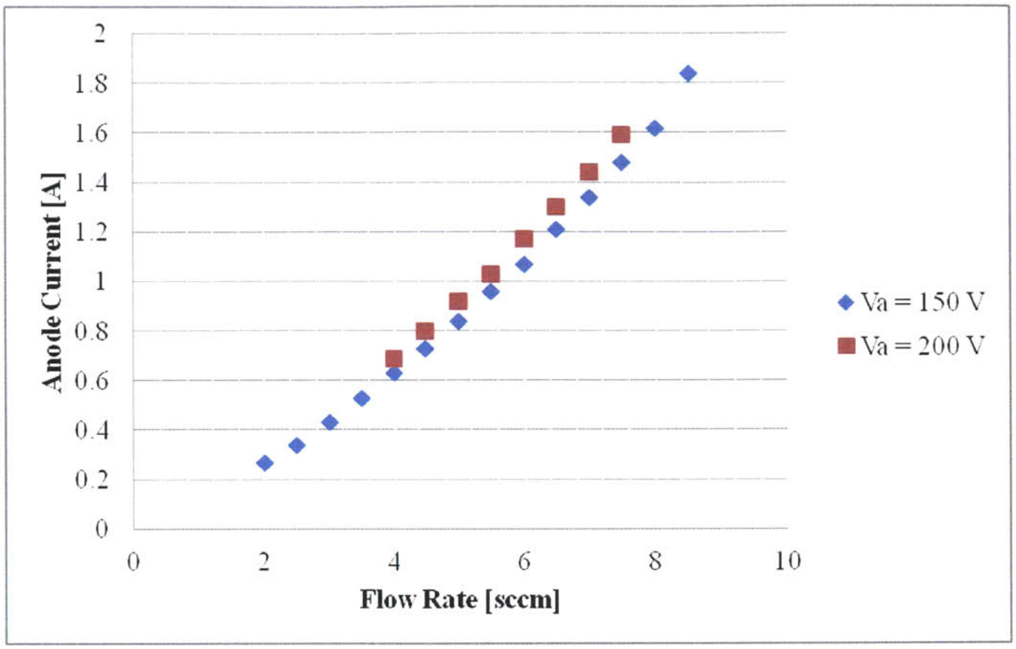

Figure 3-9: Anode flow scan.

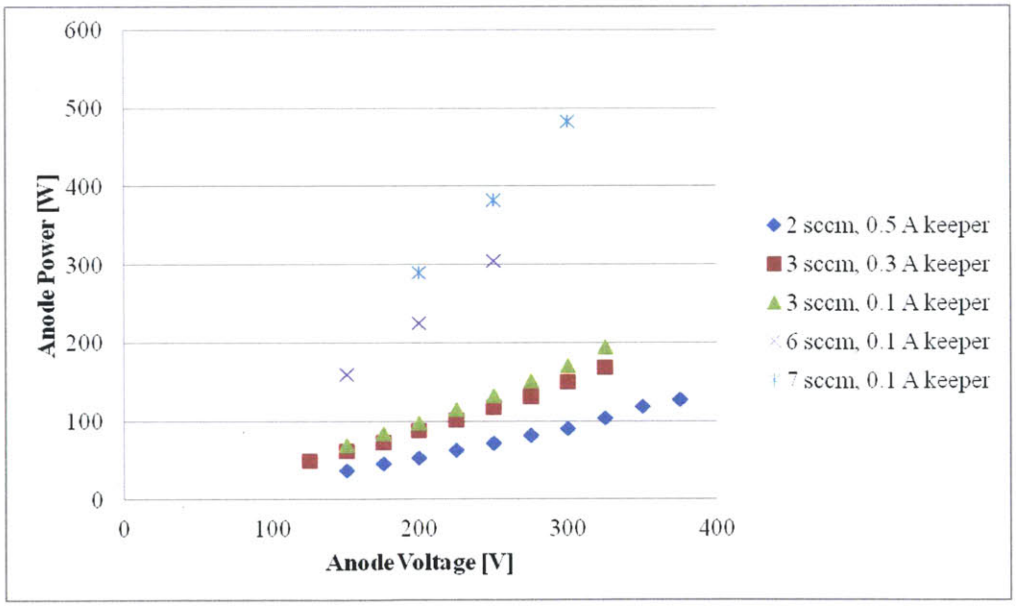

Figure 3-10: Anode power levels from the voltage scan.

as a reference. They are also higher than expected from full ion conversion of the anode flow, even full double ion conversion.

It can be observed that the anode becomes visibly hot (red-orange color, around 800^o C) when operating at high power, or when a quick transition in anode current

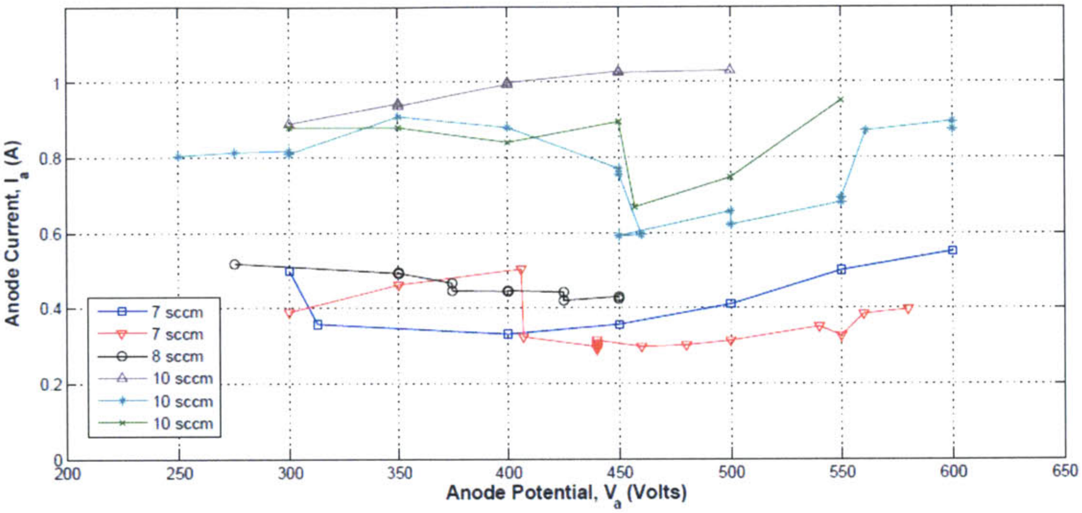

Figure 3-11: Voltage and flow scan for the DCFT [1].

is experienced. If the thruster is not shut off immediately, the excessive heat in the thruster may damage the anode itself as well as the ceramic diffuser through uneven thermal expansion. Figure 3-12 shows the extent of damage to the anode and the diffuser disk from overheating the thruster.

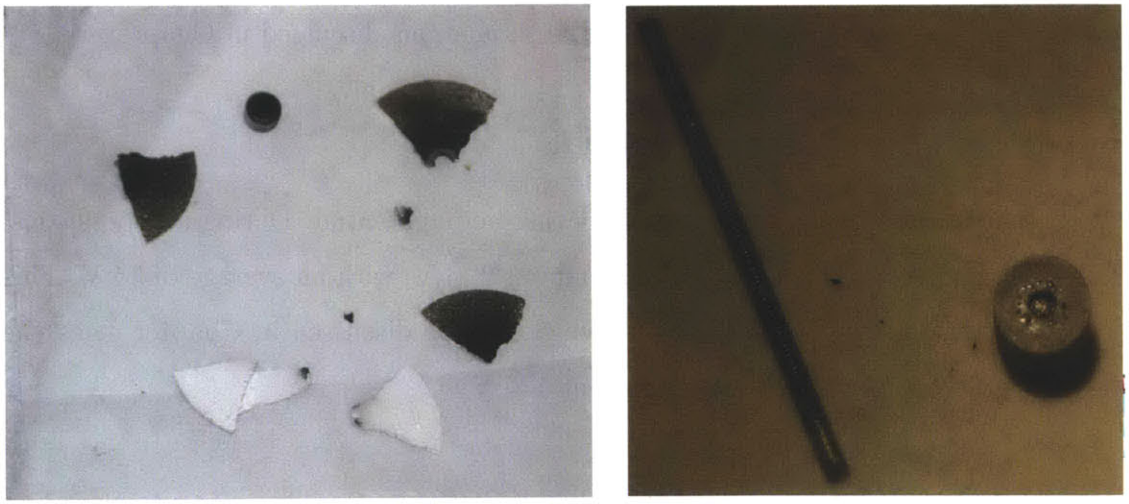

Figure 3-12: Shattered remains of the diffuser disk from thermal expansion (left), Sheared off graphite tip from anode stem (right).

The high temperatures experienced by the anode were not predicted for the CCFT, as the relatively high anode current was also unprecedented. Given the abnormally high pressure in the chamber, the original hypothesis for explaining the phenomena was a possible miscalibration of the flow regulators, which would result in a higher flowrate than recorded and, thus, higher anode current. However, subsequent to the CCFT trials, another Hall-effect thruster (Busek BHT-200) was tested in Astrovac with the same experimental setup, running at 8.5 sccm Xe. The measured values for the anode currents from this test, shown in Table, were not significantly higher than previously recorded results (Azziz, 2003) [27].

Table 3.1: BHT-200 Anode Current Measurements

Anode Voltage [V]	**Anode Current, Azziz** [A]	**Anode Current, Trial** [A]
225	0.888	0.900
250	0.878	0.892

As a result, flow regulator miscalibration may be minimal and the higher chamber pressure may be attributed to outgassing from instrumentation in Astrovac. The current conjecture on the causes of the high anode current in the CCFT is the possibility that a majority of the ionization occurs at the first cusp and with a large double or even triple ion fraction (as predicted in the simulations discussed in Chapter 4).

3.3.4 Floating Body Potential

Another issue to note is the measured floating body potential. During all operations, the Fluke multimeter measured a maximum of 20.4 V, with an average of 15 V. This is critical to note for the simulations, which will be discussed in Chapter 4, as the floating body for the thruster was fixed at 100 V.

Chapter 4

CCFT Numerical Simulations, Preliminary Results and Performance Characterization

4.1 Background: Fully Kinetic Modeling and Plasma Thruster Particle-in-Cell (PTpic)

4.1.1 Particle-in-Cell Modeling of Plasmas

In the field of plasma simulations, there are two main types of models: magnetohydrodynamic fluid models and particle-in-cell (PIC) kinetic models. While the fluid representation of plasmas is computationally expedient, the prerequisite base assumption of a Maxwellian electron energy distribution is incorrect and, as a result, is unable to model sheaths. In contrast, PIC codes, while computationally expensive, can model in kinetic detail the sheaths, which are critical elements in understanding wall effects (i.e. sputtering, secondary electrons, etc.) in plasma thruster discharge chambers. In addition, PIC also allows the electron and ion distribution functions to be computed.

With this method, individual particles in a Lagrangian frame are tracked in continuous phase space, whereas moments of the distribution such as densities and currents are computed simultaneously on Eulerian (stationary) mesh points. In plasma physics applications, the method amounts to following the trajectories of charged particles in self-consistent electromagnetic (or electrostatic) fields computed on a fixed mesh.

The method can be described by the following procedure, shown in Figure 4-1:

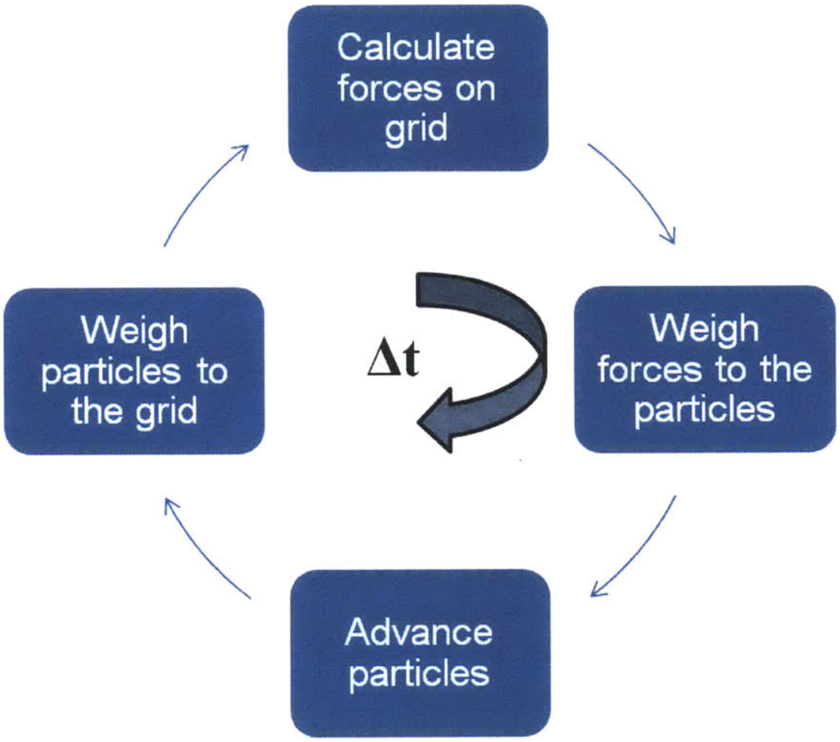

Figure 4-1: Particle-in-cell flow chart.

The process is conceptually simple: at the beginning of each cycle, the parameters and variables for the plasma and boundary conditions are initialized. Following the initialization, the particles are weighted to the nodes in the mesh. At this step, the individual properties of the particles (i.e. including their charge and mass) are spread out over several neighboring nodes. With this accomplished, the full set of Maxwell's equations is used to calculate electric potential and electric field. Given that we assume that the induced magnetic fields from associated currents in the thruster are negligible, we maintain the magnetic field as static, reduce Maxwell's equations and use Poisson's Equation to calculate the potential and the electric field in the domain:

$$\nabla^2\phi = -\frac{\rho(x)}{\epsilon_0} \tag{4.1}$$

where ϕ is the potential, $\rho(x)$ is the variable charge density over a spatial domain, and ϵ_0 is the free space permittivity. Once we discretize Poisson's equation, we would solve it with a partial differential equation solver. Once we solve for the electric field from the potential, we interpolate $\vec{E}$ at each particle location. The equations of motion for a charged particle which account for the influence of the electric and magnetic fields (as well as $E \times B$ drift, cyclotronic motion, and Hall currents) are the Lorentz force and kinematic equations:

$$m\frac{d\vec{v}}{dt} = q(\vec{E} + \vec{v} \times \vec{B}) \tag{4.2}$$

$$m\frac{d\vec{x}}{dt} = \vec{v} \tag{4.3}$$

where m, $\vec{v}$, q are the mass, velocity, and charge of the particle respectively, and $\vec{E}$ and $\vec{B}$ are the electric and magnetic fields. Note that, for PTpic, due to computational complexities, we model the velocity in three-dimensions (R, Z, and Θ) and positions in two (R,Z) in a polar coordinate scheme. Since Hall thrusters are nominally axisymmetric, axisymmetric simulation was assumed. While the particles are tracked in all three directions in velocities, only the meridional projection of each 3D position is tracked, along with all three components of velocity. Hence, they are moved in three dimensions at each time-step, but their final positions are always projected back into the R-Z plane. This is why PTpic is known as a fully-kinetic model with a "2D3V" configuration.

The Boris leapfrog algorithm, as described in detail by Birdsall [30], numerically integrate these equations to find the velocity at the next half-timestep and then, accordingly, move the particle forward at each timestep. With the trajectories of the particles calculated, their positions are then updated. With that accomplished, the code restarts the cycle at the initialization step and continues doing more iterations until the specified iteration number is reached.

Another interesting aspect to PIC is the use of superparticles. Given that the real systems studied are often extremely large in terms of the number of particles they contain, in order to make simulations efficient or at all possible, so-called superparticles are used. A super-particle is a computational unit that represents many real particles. It is allowed to rescale the number of particles, because the Lorentz force depends only on the charge to mass ratio, so a super-particle will follow the same trajectory as a real particle would. The number of real particles corresponding to a super-particle must be chosen such that sufficient statistics can be collected on the particle motion. In the following simulations, typical size is around 10^8 particles per superparticle.

While there are a few methods for solving Maxwell's equations, the method employed in this thesis is the Finite difference method (FDM). With FDM, the continuous domain is replaced with a discrete grid of points, on which the electric is calculated. Derivatives are then approximated with differences between neighboring grid-point values and thus the partial differential equations are turned into algebraic equations. As the field solver is required to be free of self-forces, inside a cell the field generated by a particle must decrease with decreasing distance from the particle.

4.1.2 Plasma Thruster Particle-in-Cell (PTpic)

The Massachusetts Institute of Technology Space Propulsion Laboratory (SPL) has been developing a 2D3V fully-kinetic model of the plasma in the discharge region of thrusters. The heritage of this code, Plasma Thruster Particle-in-Cell (PTpic), can be traced back to the PIC-Montel Carlo Collision (PIC-MCC) model developed by James Szabo. While it has been further developed by V. Blateau and J. Fox, major revisions were made to the code by Stephen Gildea which, amongst many other improvements, redesigned the potential solver and increased capabilities for adapting alternate plasma thruster designs.

In the version of the fully-kinetic code used in this thesis, the discrete particles of plasma (electrons, ions, and neutrals) are defined in continuum space for both position and velocity. These particles are then imported into a pre-made computational mesh, in which they are allowed to move under the effects of the electric and magnetic fields and undergo collisions and boundary interactions. For Hall thrusters and other Hall-type thrusters (which have been the focus of SPL's fully-kinetic models), the grid incorporates a static magnetic field and the electric field is iteratively calculated at the nodes.

PTpic employs the same methodology for plasma modeling as noted in the previous section, with a few key differences and details. For collisions, the Monte Carlo Collision (MCC) method has been employed in the PIC code. There are a number of particle interactions in the model for the ions, electrons and neutrals in the plasma. MCC was used to model three types of electron-neutral interactions: elastic scattering, ionization, and excitation. In addition, two types of ion interactions were included: ion-neutral scattering and ion-neutral charge-exchange. Coulomb electron-electron collisions were also included in the serial version of the code and were represented using two different approaches: MCC and a Langevin model based on the Fokker-Planck equation. There are a number of collisions which were neglected in the PIC code; collisions amongst ions, neutral-neutral collisions and recombination interactions were all omitted. In addition, the code employs a direct solver which employs repeated use of LU factorization to compute the potential and has replaced an iterative successive over-relaxation (SOR) solver.

However, even with the particle-in-cell method, the length and mass scales inherent in the simulation are cause for computational difficulties. Since the characteristic dimensions of most plasma thrusters are in the millimeter or centimeter range and the characteristic length of the mesh is smaller than the Debye length (Order: 10μm), this leads to an incredibly fine grid. In addition, the presence of various particles with widely disparate masses leads to large discrepancies between particle motions and thus the convergence of the PIC code is dependent on the flight time of the larger, slower particles (ions and neutrals). The low velocity of the ions and neutrals increases the number of iterations 40 times larger than what is reasonable on a local cluster, with respect to computational run-time.

In order to run a simulation with reasonable run-times on the lab group cluster, two acceleration techniques were introduced into the code: an artificial permittivity of free space and an artificial mass factor. Since the permittivity of free space is a key component of the Debye length, a larger permittivity constant would output a larger Debye length and, hence, a coarser mesh. Similarly, by artificially decreasing the mass of the slow particles (a technique used in PIC codes since the 1960's), their velocities would increase and allow for quicker convergence. To compensate for these alterations, scaling in the code was performed to increase the ionization rate. With these two tricks, the fully-kinetic code has been employed successfully for modeling various types of plasma thrusters, including Stationary Plasma Thruster (SPT)-type Hall thrusters, Thruster-with-Anode-Layer (TAL) Hall thrusters, near-vacuum Hall thrusters, and diverging cusped-field thrusters.

To perform these simulations, the parallelized version of the code is sent to the SPL Linux cluster, which consists of 144 dual-processor nodes.

4.2 Boundary Conditions, Grid Generation, and Simulation Inputs

In order to simulate any plasma thruster with PTpic, a number of input files and boundary conditions are required to represent the physical geometry and component composition, magnetic topology, and operating conditions of the thruster. Given the newly developed plug-and-play capabilities of PTpic (detailed description provided by Gildea), the inputs could be generated by commercial software and entered as fungible components into the program.

4.2.1 Magnetic Field and Grid Generation

The magnetic field of the cylindrical cusped-field thruster, developed with the Ansoft Maxwell suite, was discretized and then subsequently interpolated onto the grid as a separate input file. In direct comparison, the field strength and field lines of the PTpic interpolated input file are identical to the one generated by Maxwell SV.

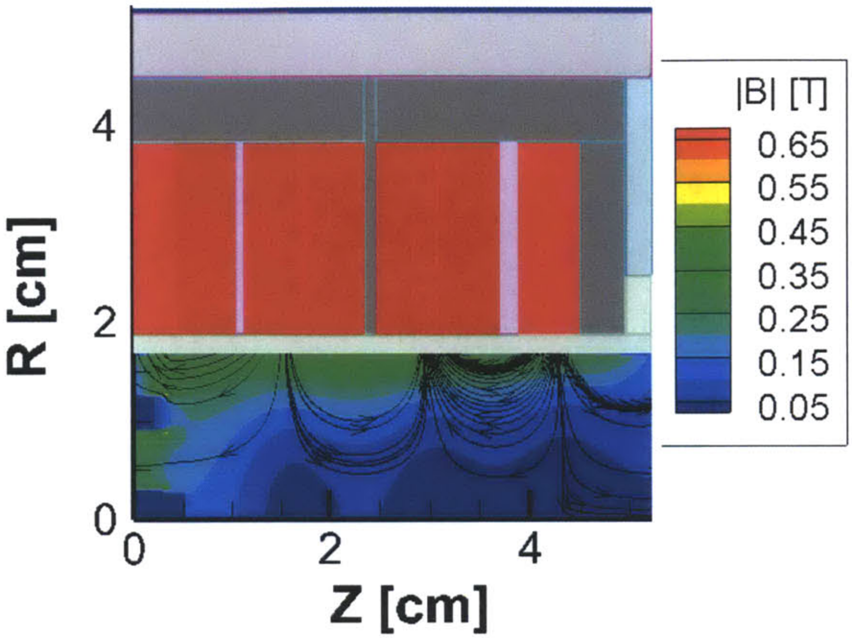

Figure 4-2: Interpolated Magnetic Field Lines and Strength Inputs for the CCFT simulation.

For the grid, Tecplot 360 was employed to create the mesh for the cylindrical cusped-field thruster. Figure 4-3 shows the computational domain overlayed with the physical dimensions of the thruster. The size of the simulated domain includes a large farfield in order to account for the plasma plume. Given that the CCFT had not been fired at the time of the modeling, assumptions about the prospective plasma's density and temperature were made based on the characteristics of the diverging cusped-field thruster. With these assumed values, the Debye length was calculated and used to determine the coarseness of the mesh. Thus, the overall size of the CCFT's computational domain (12.5 cm axial and 7.6 cm radial) and mesh coarseness are the same as the DCFT's.

4.2.2 Boundary Conditions

Figure 4-3 illustrates the different boundary conditions used in the PTpic model. The area not covered by the thruster floating body, anode and boron nitride insulator is the simulation region, the allowed locations of all particles in the simulation. The nodes at the anode position are assigned the applied positive potential, the nodes

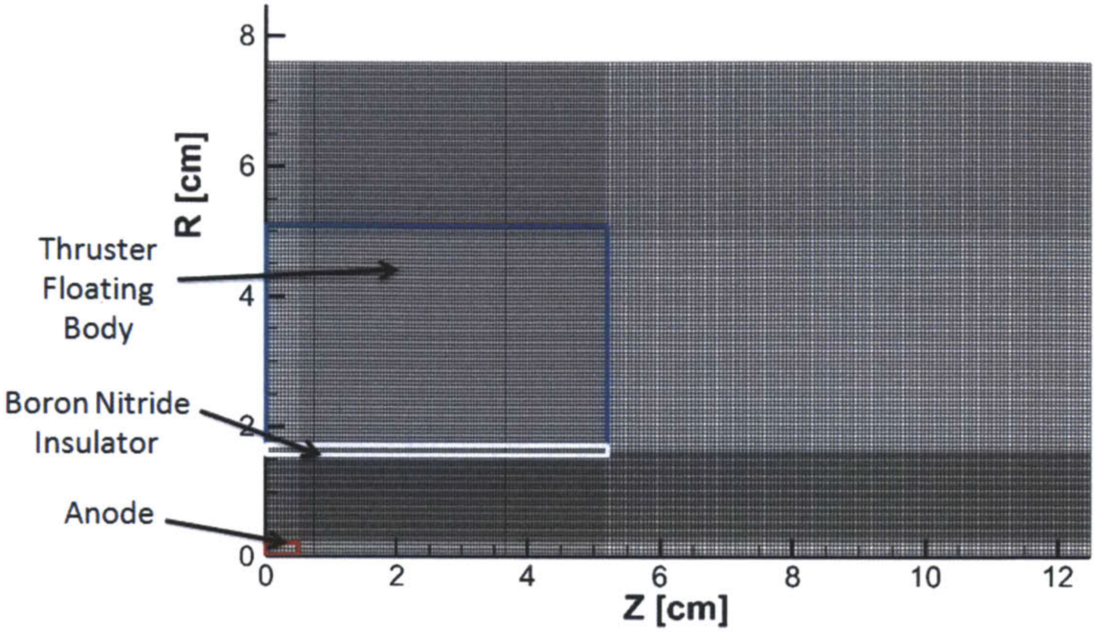

Figure 4-3: Cylindrical Cusped-Field Thruster mesh with thruster components identified.

lined along the boron nitride edge are assigned as "dielectric", and the farfield on the rightmost, topmost, and left boundary above the thruster floating body are assigned the free space boundary. At the free space boundary, the incident particles which hit the boundary are deleted. Last, the electrons are injected along the righthand farfield, with the upper-rightmost node of the simulation region specified to be at the cathode potential.

Another key boundary condition to note is the use of a fixed free body potential for the thruster body. While PTpic is equipped to solve for a variable free body potential, its employment for the cylindrical cusped-field thruster has produced anomalous potentials well exceeding -5000 V, as seen in Figure 4-4. Not only does this adversely affect the trajectories of the ions and electrons and is not an accurate physical representation of thruster potential during operations, the potential fails to resolve quickly enough and causes the code to crash.

As a result, a fixed potential of 100V is imposed on the floating body. The value for this potential has been extrapolated from the the thruster potential in converged DCFT simulations. In future simulations, this potential will be adjusted

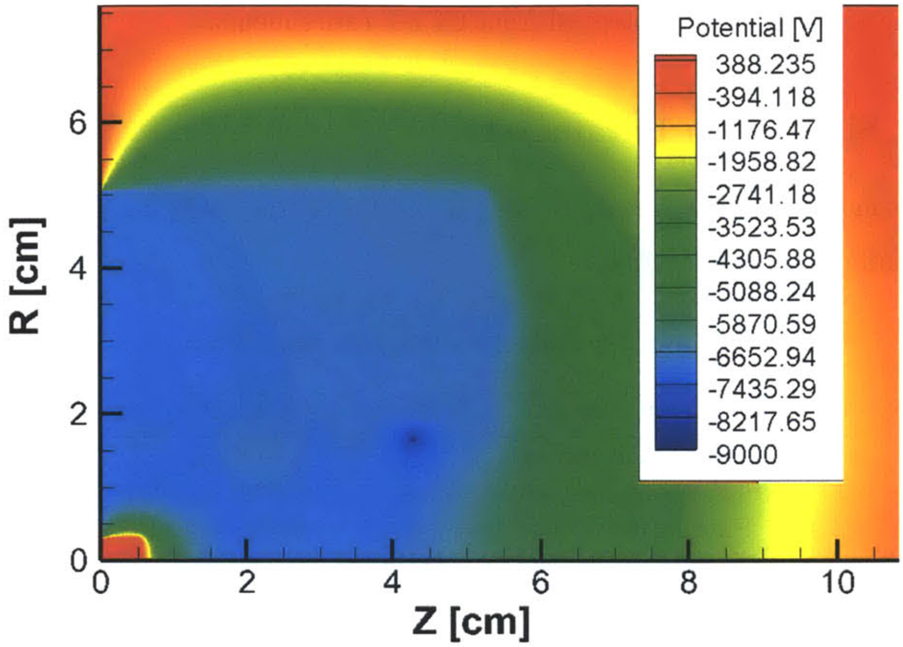

(a) PTpic simulation with calculated floating body potential, after 1 μs.

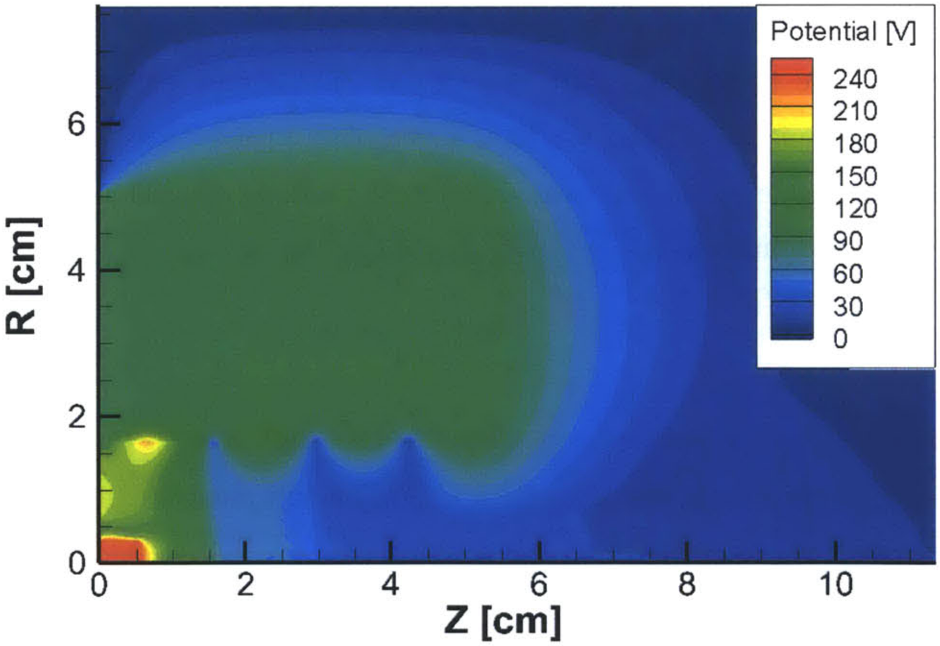

(b) PTpic simulation with fixed floating body potential, after 1 μs.

Figure 4-4: Note the high negative floating body potential in (a), which does not get resolved, completely alters the trajectories of the charged superparticles, and eventually leads to the code to crash.

to the measured thruster potential from CCFT experiments.

4.2.3 Simulation Parameters

For the simulations and to account for the mesh size, the following parameters were used for all of the simulations:

Table 4.1: Variables Used for Simulation

Variable	Symbol	Quantity
Number of Iterations	-	10 million
Number of Processors	-	24 (out of 144)
Simulation Time	dt	1.0-2.0e-12 s
Super-particle size	SPS	1.0e8
Mass factor	f	1000
Artificial Permittivity	γ	50

Based on the specifications listed above, the length of simulated time for each of these runs would be approximately 10 to 20 μs. The size of the time step, which was originally 1 picosecond and was later increased to 2 picoseconds, is based on the electron gyro-frequency, ω_c, a typical requirement for PIC codes [30]. The ratio used to determine the timestep is:

$$\omega_c dt < 0.2 \tag{4.4}$$

and given that the maximum magnetic field strength used in the CCFT is 0.6 T, the gyrofrequency is approximately 10 teraradians per second. Thus, our original timestep size was conservative and was doubled.

4.3 Preliminary Simulation Results

With the proper inputs and boundary conditions, the simulations were run over a variety of operating conditions. The simulation procedure is as follows: the code first seeds the computational domain with neutral superparticles for a period in order to provide a background for which plasma can form. After this "neutrals only" run is performed, electrons are then seeded at the farfield and the anode potential is assigned at the anode nodes. From this point onwards, the particle-in-cell algorithm determines the trajectories of the electrons and the ions generated from the collisions. The now three species of particles evolve in time for a preset number of iterations, with the "convergence" of several simulated variables as stopping criteria. When these variables, such as superparticle populations and anode current, reach steady state values, the results can then be analyzed. For the majority of the simulations, this was met within 20 μs of simulation time, as shown in Figures 3-5, 3-6, and 3-7.

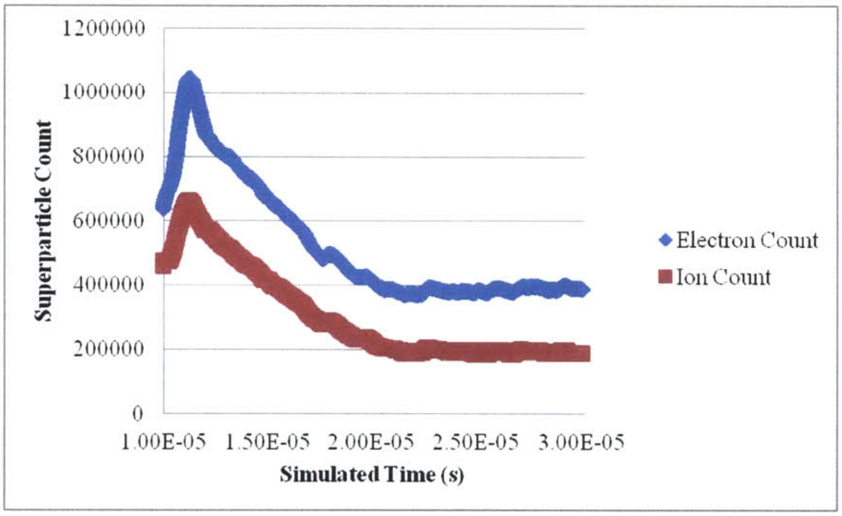

Figure 4-5: Ion and electron population, over 20 μs, operating at 4 sccm Xe and 600V. Note that the difference between electron and ion count is accounted by the presence of double ions.

To gauge the performance of the CCFT under various operating conditions, voltage scan simulations were performed. The flow rates for the following simulations were limited to 4 standard cubic centimeter per minute (sccm) of Xenon gas and resulted in an average computation time of 0.15 seconds per iteration. Given that increased flow rate results in more superparticles, there is a corresponding increase in computational time for each timestep. In addition, with sufficiently high flow rate, the increased density could lead to mesh cells becoming significantly larger than the Debye length. In that case, either the mesh must be further refined or the artificial permittivity needs to be increased, which are both undesirable situations due to

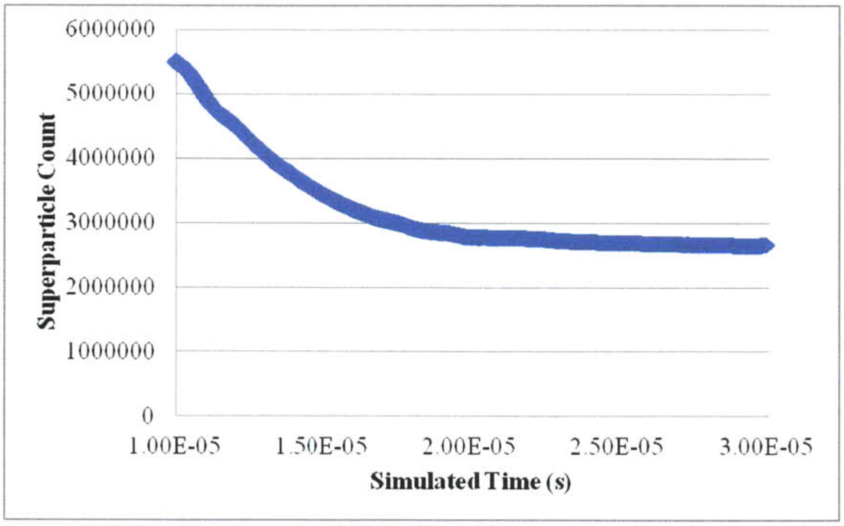

Figure 4-6: Neutral population, over 20 μs, operating at 4 sccm Xe and 600V.

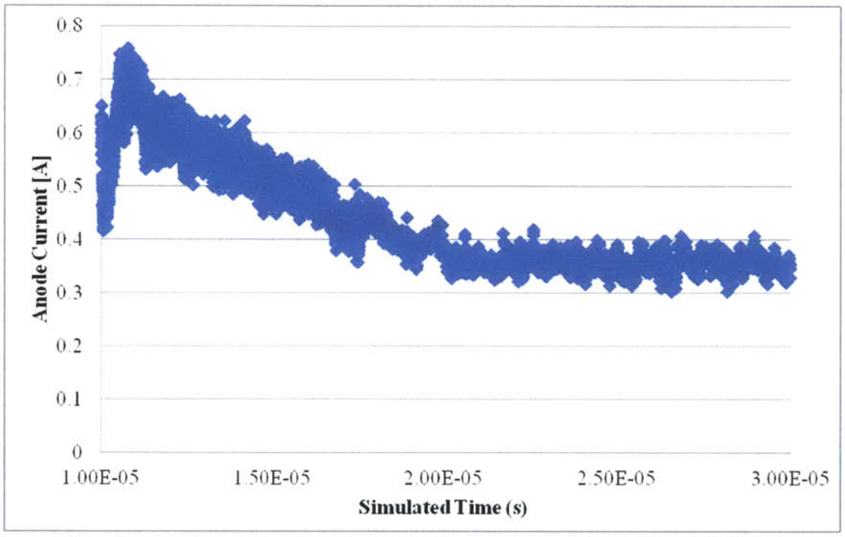

Figure 4-7: Anode current, over 20 μs, operating at 4 sccm Xe and 600V.

increased computational time and possible unphysical effects, respectively.

Instead, in the scope of this thesis, a fixed flow rate and a series of simulations scanning over a wide range of potentials was used, to some effect, to explore the performance of the CCFT. At the "low" flow rate, a trio of simulations with fixed anode potentials (250V, 425V, and 600V) were applied. For time expediency, the low voltage simulation was performed first and, through saved "restart" files, subsequent runs with altered anode potential were continued from the converged simulations, rather than restarting from the seeding stage.

4.3.1 Plasma Structure

For all cases, the qualitative nature of the discharged plume provides insight on the success of the cylindrical cusped-field design. Compared to the diverging cusped-field thruster, which features a hollow conical plume in simulations and experiments, the cylindrical cusped-field thruster has a collimated, solid plume similar to a Hall-effect thruster plume, as shown in Figure 4-8.

The stratification of the CCFT plume in Figure 4-8(b) can be further shown by quantifying the density at a distance 5 and 7 centimeters from the exit of the thruster. As shown in Figure 4-9, the density drops exponentially radially away from the centerline.

For further details on the structure of the CCFT discharge, the ion and electron densities and temperatures of the CCFT simulations operating at 4 sccm Xe and 600V are shown in Figures 4-10 to 4-13. Figure 4-10 displays a snapshot of the CCFT ion density which reveals a collimated plume with a sharp density gradient from a maximum of 1x10^{19} ions / m^3 along the centerline and tapering off at the edge with 1x10^{17} ions / m^3. Figure 4-11 shows that the electrons follow the magnetic field lines from outside of the exit and are confined in the cusps.

The potentials for the CCFT are also shown in the Figure 4-14. Given that ionization occurs heavily upstream in the first cusp and the sharp gradient in potential also occurs in the vicinity of the first cusp, the electric field experienced at this location causes the coupled ion acceleration. In addition, this would also imply that erosion would be highest at the first cusp; the validity of this hypothesis will be determined in the subsequent subsection.

The plasma structure of the CCFT matches preliminary visual experimental results as seen in Section 3.3.1, as the plume is shown to be highly collimated.

4.3.2 Performance Characterization

The key measures of performance for electric propulsion devices include but are not limited to: thrust, specific impulse, and efficiency. For Hall-effect thrusters, efficiency

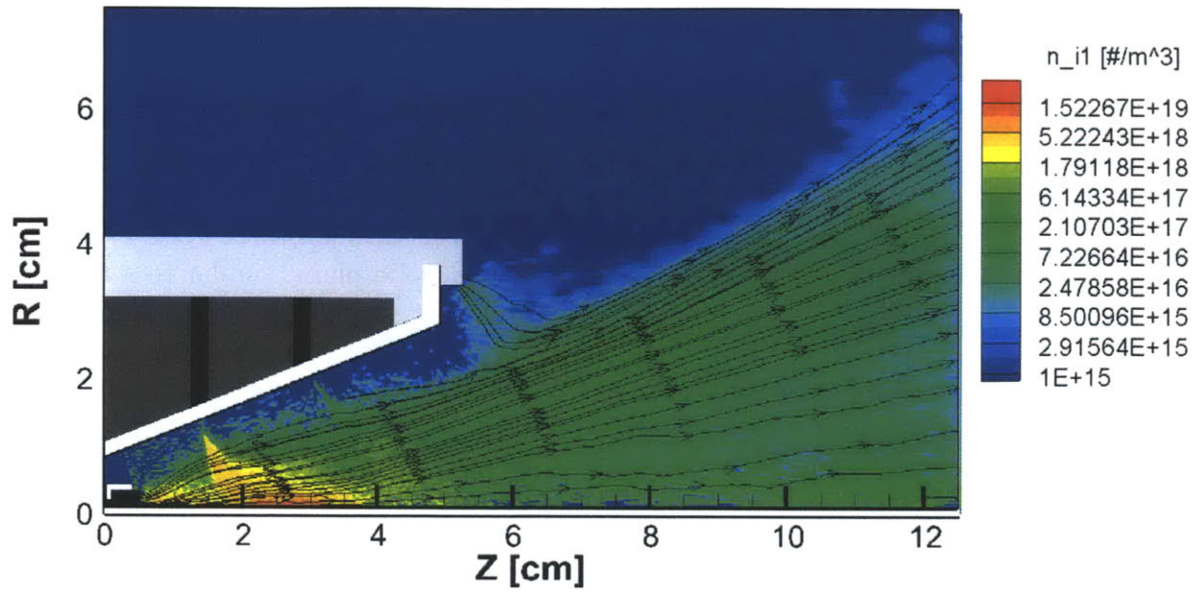

(a) Streamlines of the DCFT and ion superparticle density, snapshot moment at 20 μs.

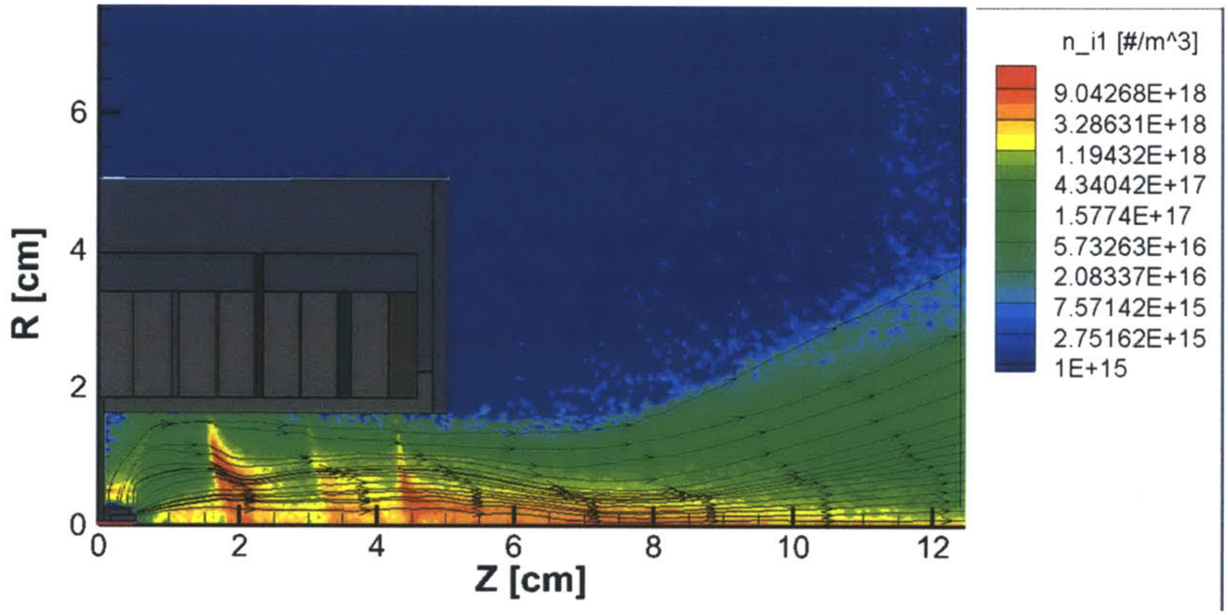

(b) Streamlines of the CCFT and ion superparticle density, snapshot moment at 20 μs.

Figure 4-8: Streamlines and ion densities for the DCFT and CCFT. Note how the streamlines follow a hollow conical plume of the DCFT whereas the CCFT has a solid plume shape.

can be further categorized as anode thrust efficiency η_t, beam efficiency η_b, and utilization efficiency η_u. These efficiencies are defined as:

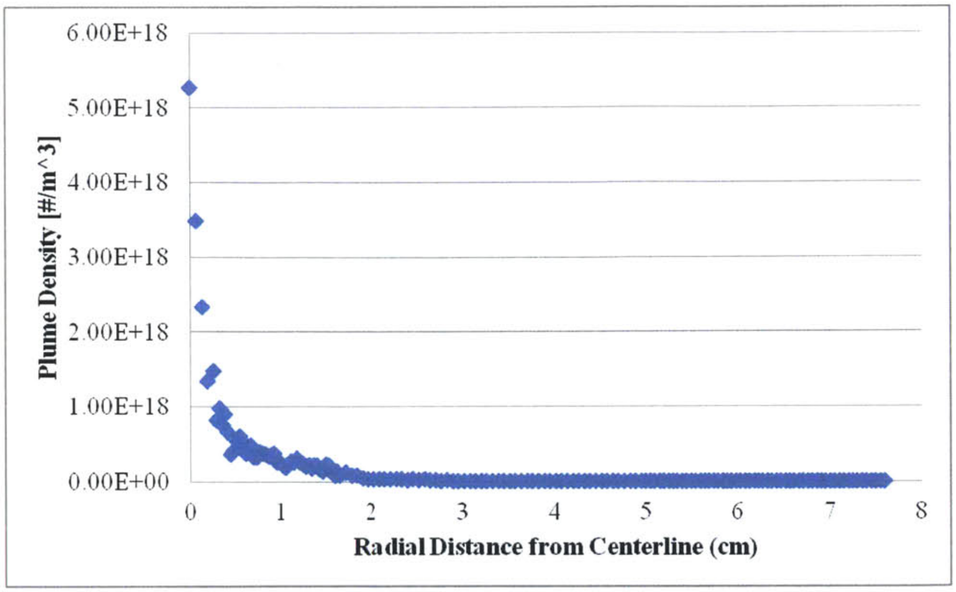

(a) Radial density of the CCFT Plume, 5 centimeters away from the thruster exit.

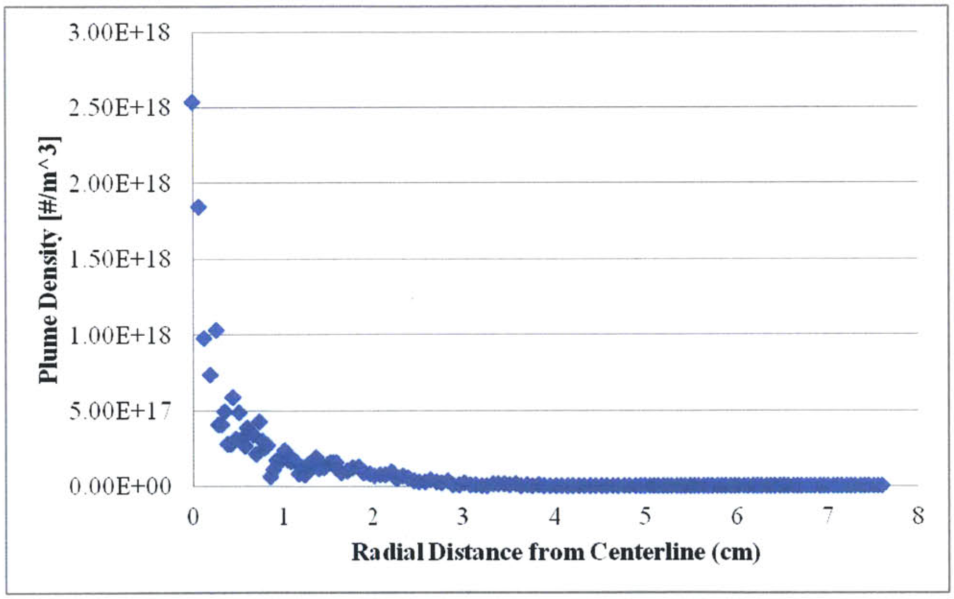

(b) Radial density of the CCFT Plume, 7 centimeters away from the thruster exit.

Figure 4-9: Radial density of the CCFT Plume, 5 centimeters and 7 centimeters from the thruster exit. Note that the density drops drastically 1 centimer away from the centerline.

$$\eta_t = \frac{T^2}{2m_a P_a} \tag{4.5}$$

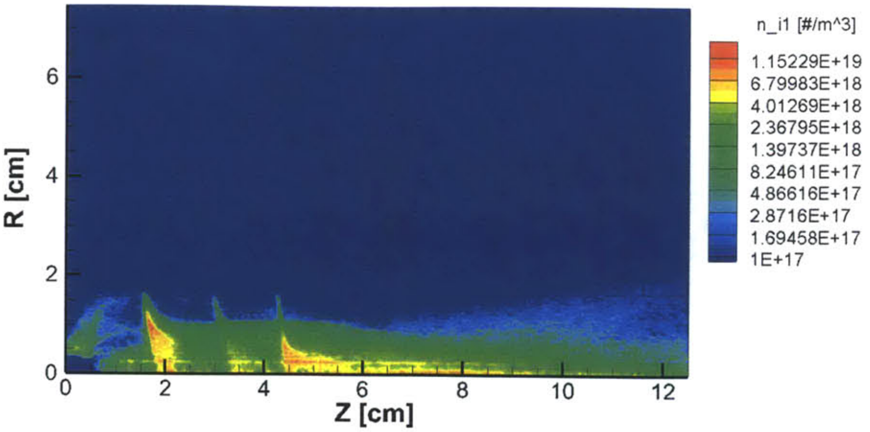

Figure 4-10: Single ion superparticle density snapshot moment at 20 μs.

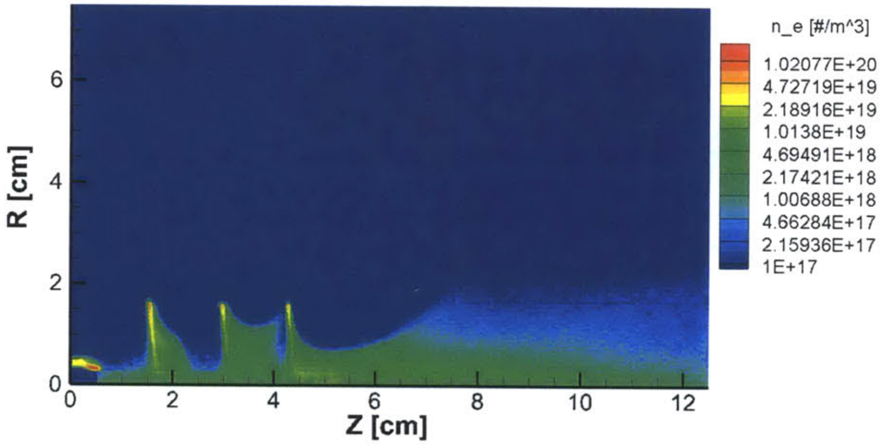

Figure 4-11: Electron superparticle density snapshot moment at 20 μs.

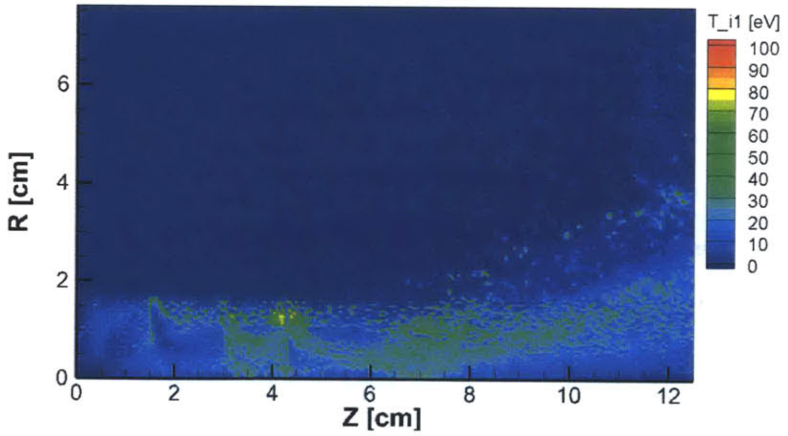

Figure 4-12: Single ion temperature snapshot moment at 20 μs.

$$\eta_b = \frac{I_b}{I_a} \tag{4.6}$$

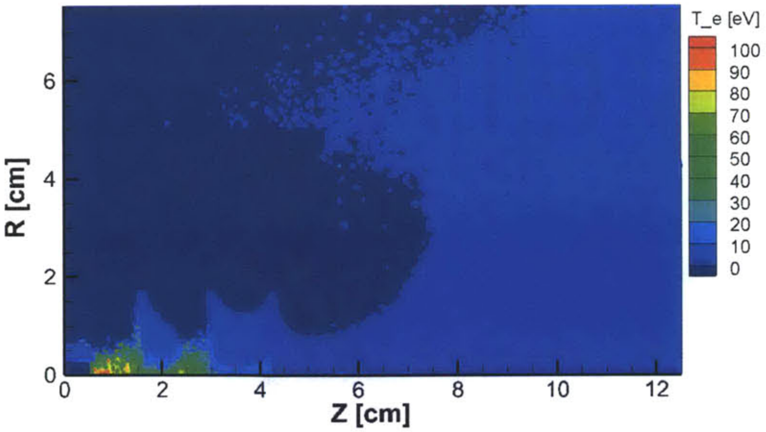

Figure 4-13: Electron temperature snapshot moment at 20 μs.

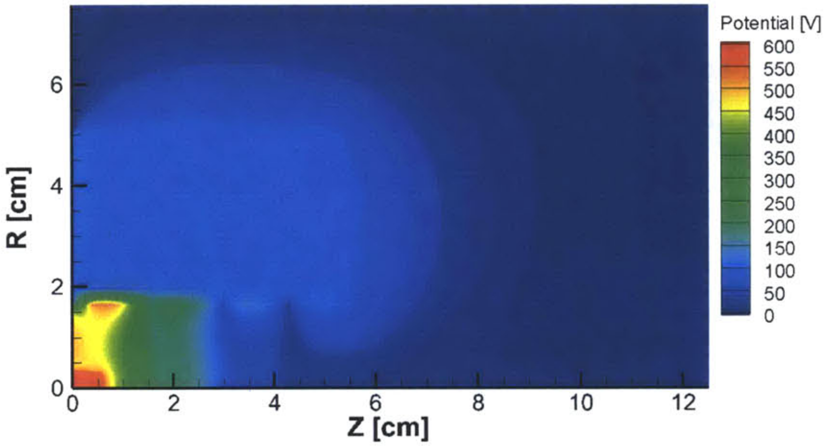

Figure 4-14: Potential snapshot moment at 20 μs.

$$\eta_u = \frac{I_b}{I_n} \tag{4.7}$$

where T is thrust [N], m_a is the mass flow rate [kg/s], P_a is the anode power [W], I_b is the beam current, I_a is the anode current, and I_n is the neutral current or the current from totally single-ionizing all incoming propellant.

With these measures, we first perform efficiency calculations for the low flow (4 sccm Xe) and low power (250V) operating condition. With the steady state values of thrust of 3.5 mN (shown in Figure 4-15(a)), anode current of 0.3 A, and beam current of 0.25 A (shown in Figure 4-15(b)) as well as a neutral current of 0.289 A for 4 sccm flow, we find that the "low-power" (75 W) CCFT has a 21% anode thrust efficiency, 85% beam efficiency, 86.5% utilization efficiency, and specific impulse of 900 seconds.

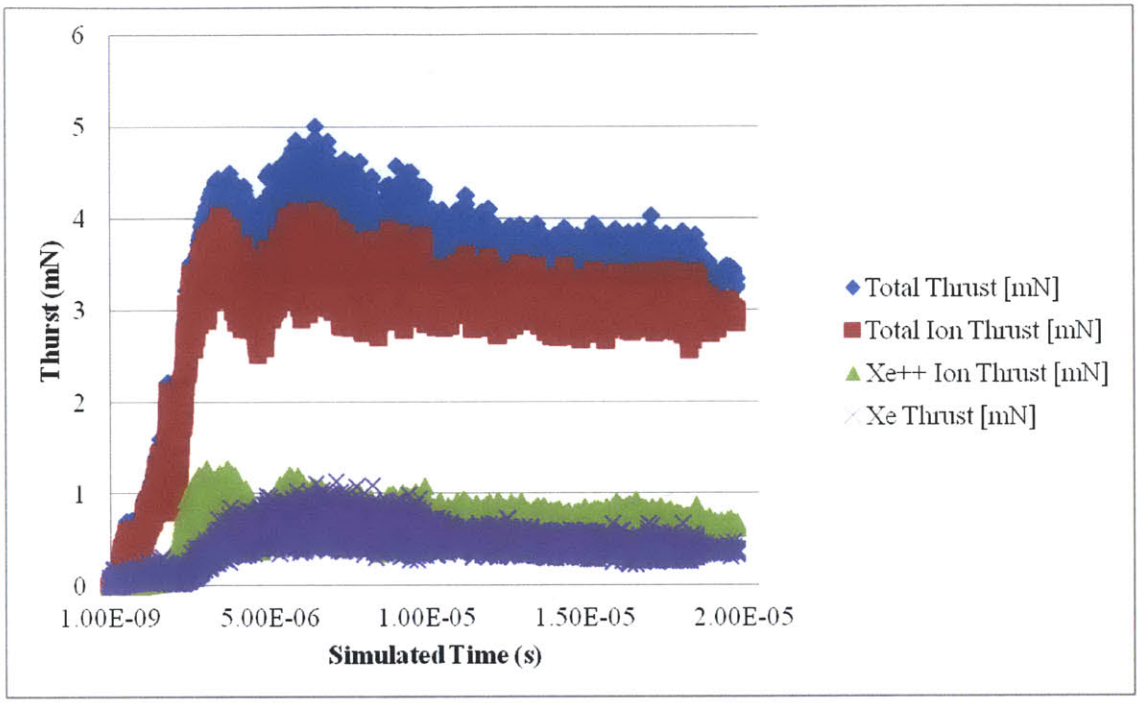

(a) Thrust estimates of the CCFT, at 250 V and 4 sccm Xenon flow, for over 20 μs.

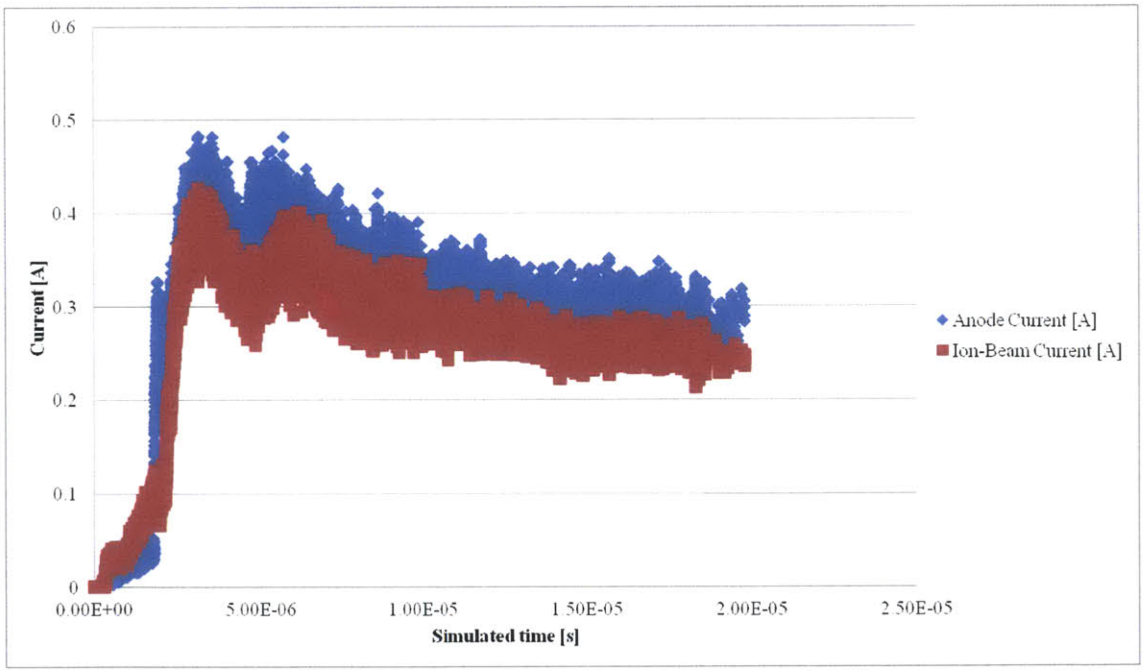

(b) Anode and beam currents, at 250 V and 4 sccm Xenon flow, for over 20 μs.

Figure 4-15: Thrust, anode current, and beam current for the CCFT operating at 250 V anode potential and injection of 4 sccm Xe

In comparison, at the same low flow rate and high power (600 V) operating condition, we have a thrust of 7 mN, anode current of 0.33 A, and beam current of 0.28 A. For the "high-power" case (210 W), the anode thrust efficiency is 30%, the beam efficiency is 85%, the utilization efficiency is 97%, and the specific impulse is 1800 seconds. For low flow rates in the cylindrical cusped-field thruster, it appears that the ionization is drastically improved with higher anode potential.

The results for all of the simulations are shown in Table 4.2.

Table 4.2: Performance Characteristics for Various Operating Conditions of the CCFT

	Thrust [mN]	**Isp** [s]	I_a [A]	I_b [A]	η_t [%]	η_u [%]	η_b [%]
4 sccm, 250 V	3.5	900	0.3	0.25	21	85	86.5
4 sccm, 425 V	5	1296	0.32	0.275	25	95	86
4 sccm, 600 V	7	1800	0.33	0.28	30	97	85

4.3.3 Erosion Estimates

A dielectric erosion module has been recently adapted into PTpic (Gildea, 2012) [10] and was used for preliminary lifetime measurements of the CCFT under two operating conditions. The module, which was based on the erosion models developed by S. Cheng [19] and J. Yim [18], calculates the sputtering from singly charged ions, doubly charged ions, and charge-exchange neutral particles. From impacts from these incident particles, a volume V is eroded from the surface (designated as Boron Nitride Insulator in Figure 4-3), which is calculated in the following equation [10]:

$$V = W \cdot e \cdot S_{\xi}(E, \Theta) = \delta A \tag{4.8}$$

where W is the superparticle weight, e is the elementary charge, and S_{ξ} is the sputter yield, which is a function of Θ (the incidence ange of the particle) and E (the incident particle energy). From Equation (4.8), the eroded depth, δ, can also be calculated for a designated unit area A. The erosion rates are calculated via averaging

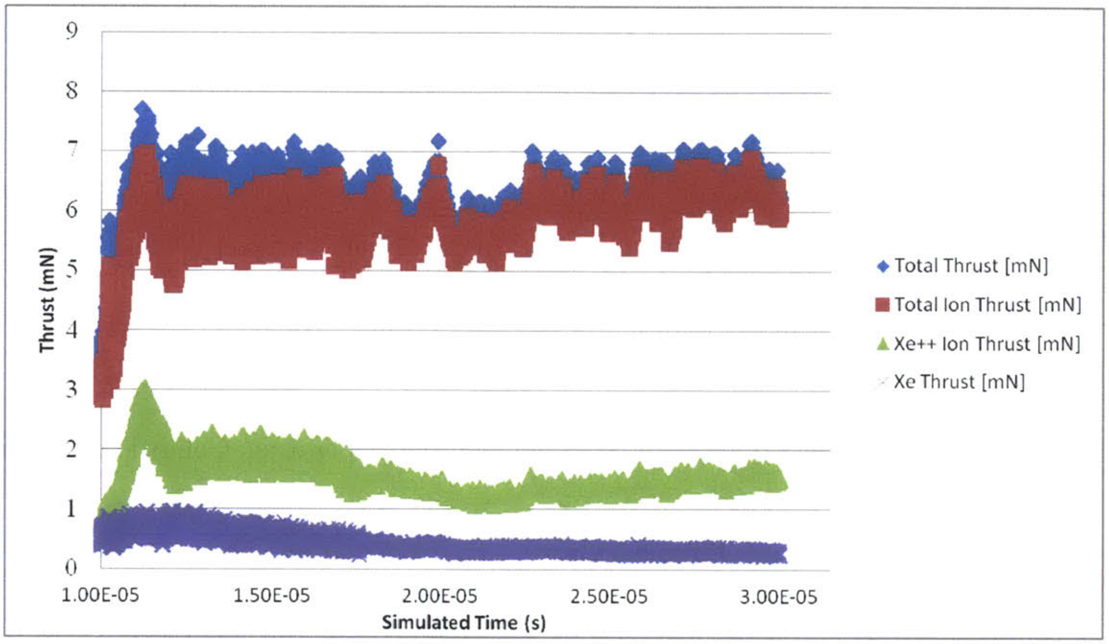

(a) Thrust estimates of the CCFT, at 600 V and 4 sccm Xenon flow, for over 20 μs.

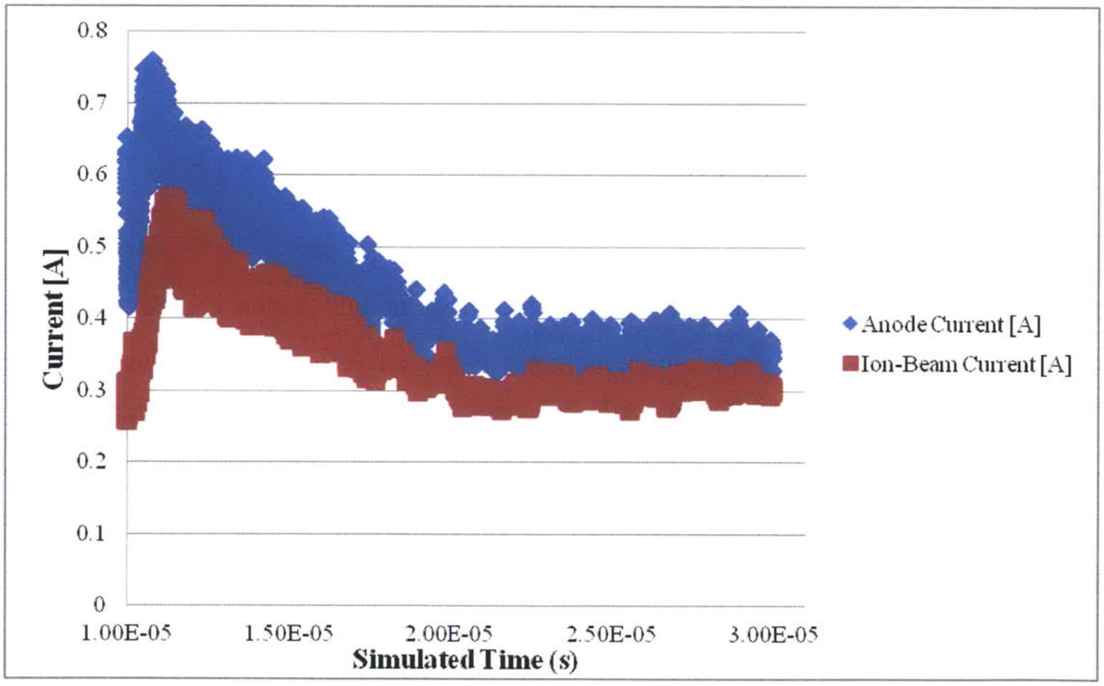

(b) Anode and beam currents, at 600 V and 4 sccm Xenon flow, for over 20 μs.

Figure 4-16: Thrust, anode current, and beam current for the CCFT operating at 600 V anode potential and injection of 4 sccm Xe the eroded depths over a simulated period of time. For additional details on the implementation of the erosion model, refer to S. Gildea's thesis [10].

The two simulatiions which employed the erosion module were the low flow, high power (4 sccm Xe, 600 V anode potential) and high flow, high power (8 sccm Xe, 600 V anode potential) cases. While the erosion rates were taken at regular intervals (every 100,000 iterations of simulation time) and the rates are unsteady during the startup transients, the erosion rates are steady when the simulations have "converged". The erosion rates at convergence [20 μs simulated time] for the two simulations are presented in Figures 3-17 and 3-18:

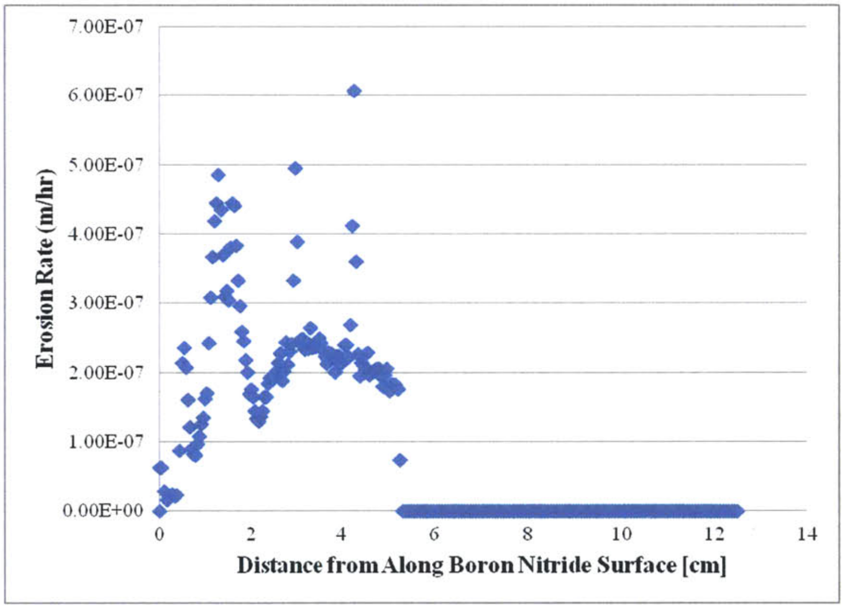

Figure 4-17: Erosion rate of the CCFT, operating at 250 V and 4 sccm Xe.

With the maximum erosion rate of 0.6 $\mu m/hr$ for the low voltage case and 0.95 $\mu m/hr$ for the high voltage case, this leads to a lifetime of 4166 hours hours and 2631 hours, respectively, with the 2.5 millimeter-thick boron nitride walls. For both simulations, the local of maxima for erosion are mainly at the three cusps, as was the case for the DCFT. However, there are marked differences between the simulated erosion in the CCFT and DCFT. In contrast to the maximum erosion at Cusp 2 for the DCFT, the location of maximum erosion for the "low-power" CCFT is is at cusp 3, and cusp 1 for the "high-power" case. These locations are presumed to be where

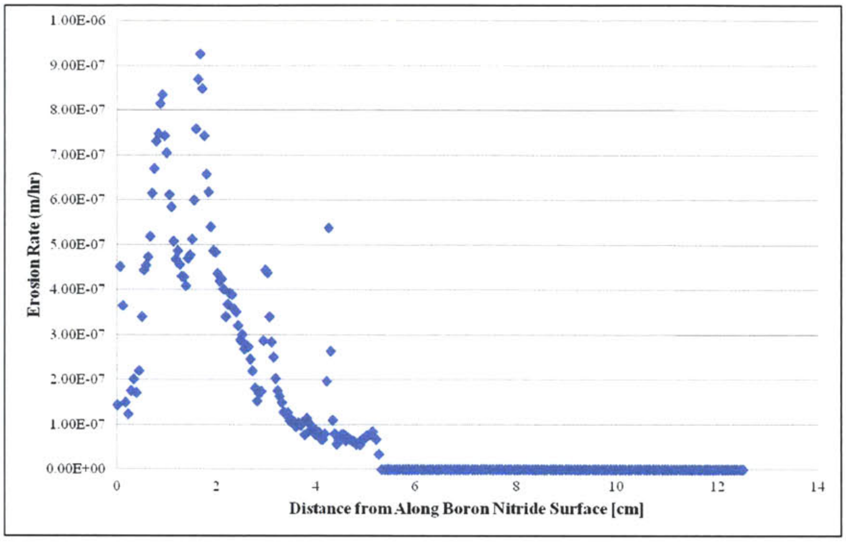

Figure 4-18: Erosion rate of the CCFT, operating at 600 V and 4 sccm Xe.

the most ionization occurs.

It is also critical to note that while the DCFT has nearly constant erosion rates between cusps [23], the CCFT exhibits linear erosion between cusps at similar power levels. In addition, a second peak of erosion appears before the first cusp in the "high-power" case. This peak may be related to the relatively lower magnetic field strength at this region, which would allow for a greater electron flux and, subsequently, increased ion sputtering. Since the CCFT has more utilization efficiency at higher power, the expansion of this pre-cusp peak becomes more apparent with increased anode potential.

4.4 Simulations and Preliminary Experimental Observations

Comparison between simulation and experimental results of the CCFT operating at various operating conditions is currently ongoing. However, initial observations show qualitative similarities between the simulations and experiments. As seen in Figure 4-19, the plume shape for both the PTpic simulation and actual CCFT operation is remarkably similar for the same operating condition (4 sccm Xe and 250 V anode potential). In both simulations and observations, there is an initial necking down of the plume, followed by radial expansion further downstream.

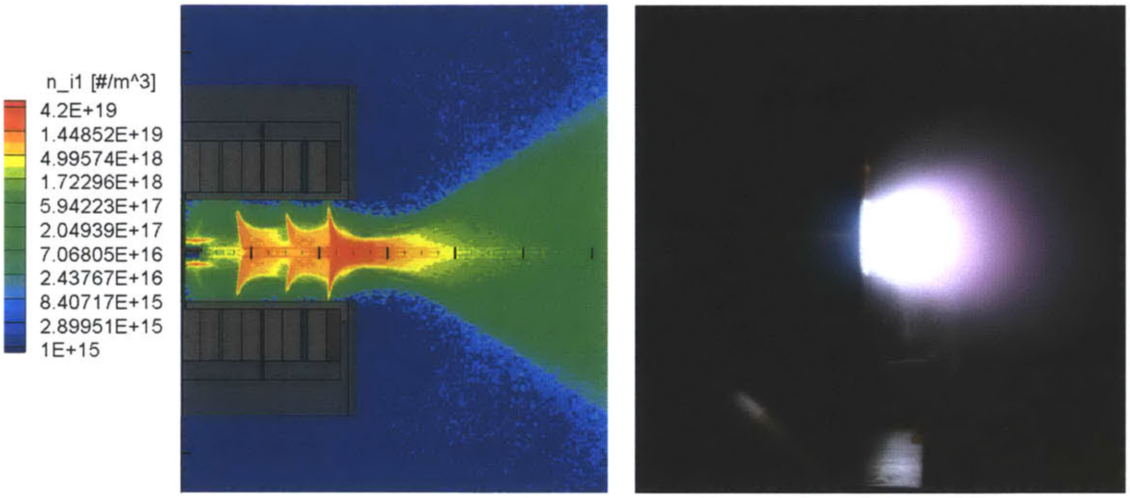

Figure 4-19: Simulation of CCFT, operating at 250 V at the anode and with 4 sccm Xe flow (left), CCFT operating at 250 V at the anode and with 4 sccm Xe flow (right).

Furthermore, the simulated predictions that sputtering would occur heavily at the cusps were validated by experimentation. Initial imaging of the CCFT boron nitride insert shows that the primary locations of erosion are indeed at the cusps, with re-deposition of sputtered graphite from the anode onto the walls as well as the porous alumina diffuser disk.

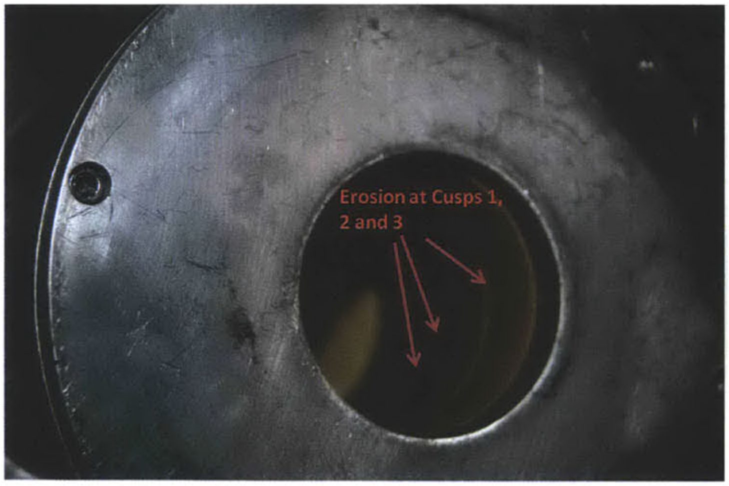

Figure 4-20: Angled image of boron nitride insert in the CCFT, with rings of erosion at the cusps and deposition in between.

However, one issue that has arisen from the experimental observations is the floating body potential. Although the simulations covered all have a floating body potential of 100 V, the measurements made from experimentation show that the floating potential ranges in the low 10's of volts, with maximum of 20 V, for the CCFT during operation. As a result, there may be minor discrepancies in the simulated results and subsequent simulations with the adjusted floating body potential should be performed.

With the CCFT, quantitative comparisons between simulation and experimentation will assist in the iterative process of validating PTpic and using PTpic in the design of other plasma thrusters.

Chapter 5

Ion Beam Diagnostics for Erosion Measurements

5.1 Background

Traditionally, the impact of surface effects such as sputtering and redeposition on plasma thruster longevity have been experimentally measured with the use of devices such as optical profilometers (Figure 5-1) or quartz crystal microbalances. Given that the measuring resolution of these devices are typically in the order of the 100 μm level, measurements must be made after long-duration operations. In the case of the DCFT, the erosion measurements took 204 hours of operation [23]. As a result, reliable erosion measurements via these instruments are often time-consuming and costly. Furthermore, the data obtained is limited to the fixed operating condition used during the long duration testing. In order to determine the effects of different operating conditions on erosion, the long duration test would need to be repeated for the new condition. Last, the thruster typically requires disassembly in order to retrieve the eroded dielectric insert, which compounds the inexpediency of the process.

Ion beam analysis (IBA) is an alternative diagnostic tool which could provide a more versatile approach to investigating surface effects. While novel to the space propulsion community, IBA is a non-destructive technique used by the thin film materials and the tokamak operator community for surface profiling. While ion beam

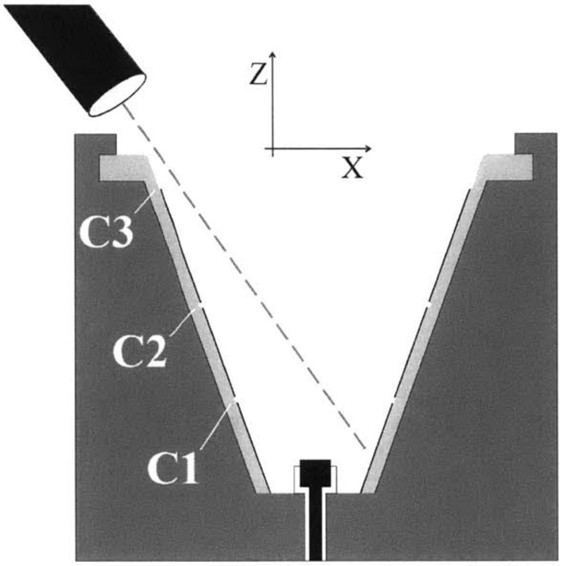

Figure 5-1: Schematics illustrating how profilometry measurements were performed for the 204 hr CCFT longevity test [7].

analysis is a family of different analytical techniques, every technique involves the use of focused, low current, high energy[MeV] ion beams to collide with target surfaces. Energy spectra of byproducts from the collisions (scattered ions, radiation, etc.) are measured by detectors and translated into the elemental depth profiles of the near-surface layer of targeted materials. For an in-depth introduction to ion beam analysis, refer to Tesmer, et al. Modern Ion Beam Materials Analysis [28].

There are multiple advantages of using ion beam analysis for erosion measurement. Given that IBA methods are highly sensitive and allow the detection of elements in the sub-monolayer range, the depth resolution is typically in the range of a few nanometers to a few tens of nanometers. As a result, changes in depth as low as tens of nanometers can be detected with an accuracy of within a few percent, which is well within the range of erosion depth of a plasma thruster operating for a few minutes. Furthermore, the applied beam size can be adjusted and the beam itself can be redirected during operation. While the technique measures the surface directly at select locations, it can be used to "map" out the entirety of a target's surface.

Another key advantage of IBA is the ability to perform in-situ erosion measurements during thruster operation and does not require disassembly of the device or designation of reference markers. Coupled with the fast measurement capabilities, IBA can be used to determine the erosion rate of different operating conditions in real time within minutes. Ion beam analysis can also determine surface composition in addition to surface profiles. With the Elastic Recoil Detection (ERD) technique, impurity concentration on the dielectric surface from sputtered particles can be qualified and quantified. Past studies have suggested that impurities such as trapped hydrogen can affect plasma behavior and overall Hall thruster operations.

Last, implementation of ion beam analysis is simple and the technique can be applied to a wide range of materials, including crystalline and amorphous targets. No special specimen preparation, such as polishing or chemical treatment, is required for surface composition measurements. For erosion measurements, there is an additional ion implantation process which must take place before analysis. While this implantation phase is relatively time consuming compared to the subsequent analysis, it takes a fraction of the time needed for profilometry measurements and only needs to be applied once.

While there are many methods which belong to the IBA analysis family, the two techniques used exclusively in this thesis are Rutherford Backscattering Spectrometry and Nuclear Reaction Analysis.

5.2 Rutherford Backscattering Spectrometry and Nuclear Reaction Analysis

With Rutherford Backscattering Spectrometry (RBS), the depth profile and atomic concentration of a target can be detected through the energy spectrum of backscattered ions. The process begins with a directed flux of high energy ions (protons or alpha particles) towards a target surface, usually composed of high atomic number ("high-Z") elements. As the incident ions collide with the surface, they will backscatter at a certain angle and lose energy. These ions are then collected by detectors and their energies are measured in a spectrum.

From a purely kinematic standpoint, the energy E_1 of the scattered light projectile from a collision with the more massive target is reduced from the initial energy E_0 [29]:

$$E_1 = k \cdot E_0 \tag{5.1}$$

where k is the kinematic factor:

$$k = \left(\frac{m_1 cos\theta_1 + \sqrt{m_2^2 - m_1^2 (sin\theta_1)^2}}{m_1 + m_2} \right)^2 \tag{5.2}$$

where m_1 is the mass of the incident particle, m_2 is the mass of the target nucleus, and θ_1 is the scattering angle of the projectile.

As with the original Geiger-Marsden experiment, the Rutherford backscattering of these ions is an elastic collision between a high kinetic-energy particle and a stationary particle located in the sample, where energy is conserved. However, there are cases where there are non-conservative collisions. In these circumstances, a collision between the ion beam and the surface can induce nuclear reactions at the surface, which can result in the production of high energy protons [p], gamma rays [γ], neutrons [n], and alphas [α]. In this case, Nuclear Reaction Analysis (NRA) is more useful for detecting these lighter, higher-energy radiation byproducts.

Figure 5-2 provides a concise description of the two types of ion beam analyses.

5.3 Simulation Software and Depth Markers

5.3.1 SIMNRA

One of the key software suites used in this thesis was SIMNRA. SIMNRA simulations can be used to predict spectra before experimentation and, through comparisons with experimental data, determine the surface composition [9]. In Figure 5-3, an energy spectra obtained from a SIMNRA simulation of a RBS scan of an aluminum sample displays an illustrative example of the outputs from ion beam analysis.

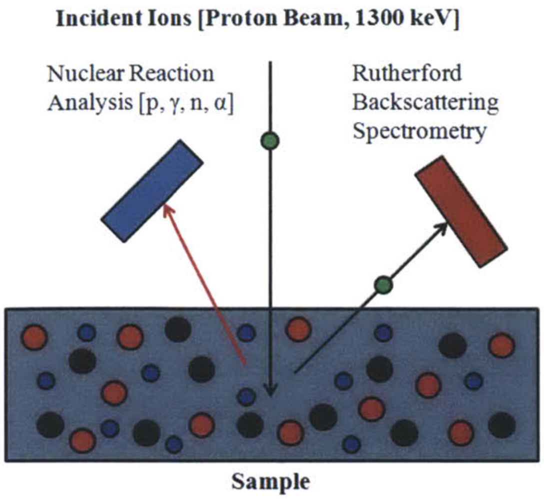

Figure 5-2: Schematic of Rutherford Backscattering Spectrometry and Nuclear Reaction Analysis.

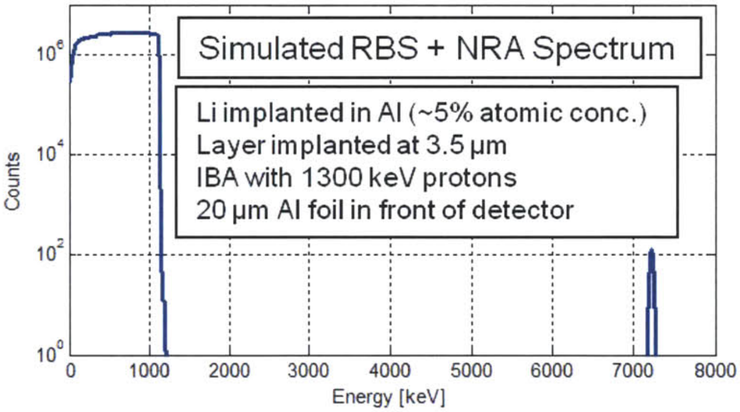

Figure 5-3: Simulated Rutherford Backscattering Spectroscopy and NRA spectra of a lithium implanted aluminum sample [8].

This simulated sample has an implanted lithium layer, 3.5 μm deep and at 5 % concentration, under the surface. Collisions between the 1300 keV protons which penetrate the surface and this "depth marker" lithium layer result in nuclear reactions. As a result, the structure of the distribution obtained from the simulation is bimodal: the first curve, on the left side of the spectrum, is the measurement of the backscattered protons with energy equal or less than the energy of the incident ions, and the second peak is the measurement of the nuclear reaction byproducts.

During actual experimentation, an optimal arrangement for the setup would be the use of dual detectors to separately measure the two curves. The RBS detector can measure both backscattered protons and α particles and can be used to determine if surface composition has changed. In contrast, the NRA detector has an aluminum foil covering its silicon layer, which prevents low-energy particles from reaching the detector. As such, it only detects the high energy peak [11].

5.3.2 Depth Markers

Depth markers can be used in conjunction with the ion beam analysis techniques to facilitate erosion and re-deposition studies. Depth markers have several characteristics useful for erosion measurements. Given that the depth markers are implanted with a pre-determined energy, their depths are known. In addition, the depth of the marker layer determines the energy of the particles that emerge after the nuclear reaction. In Figure 5-4, the simulated NRA spectra show three distinct peaks for three implanted layers of lithium.

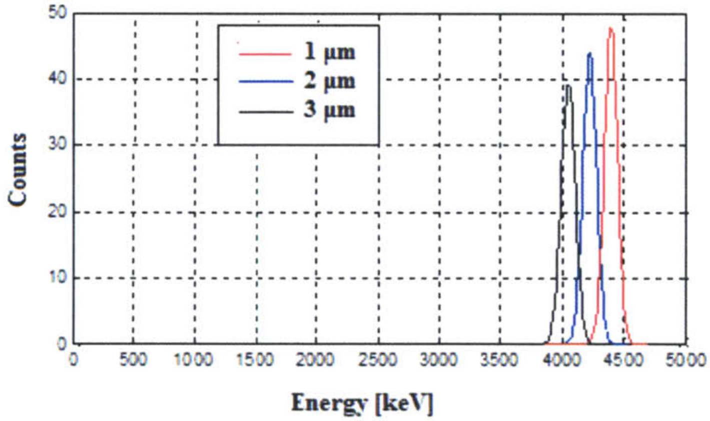

Figure 5-4: Spectra of implanted Li, at various depths.

As can be seen in the figure, the depth of the lithium layer is inversely proportional to the measured energy. Hence, when a target surface with an implanted marker layer is exposed to a plasma source and minor erosion removes some of the material on top of the marker layer, there will be a significant difference in the energies of the NRA spectra before and after exposure. This difference can and has been used as a means for calculating the depth of the erosion and is why ion beam analysis can be used for measuring erosion.

In all the IBA experiments discussed in this thesis, the depth marker material used was lithium. Lithium was chosen because of its low atomic number, Z, and its unique nuclear reaction with protons that produce alpha particles. With its low Z value, lithium causes negligible damage to the bulk material as it is implanted. The nuclear reaction lithium has with proton collisions produces alpha particles which are observed as a 17.35 MeV peak in the RBS spectrum. The high energy of the nuclear reaction creates significant separation between lithium peak and the structure representing the bulk material.

5.4 Research Overview

This thesis covers the preliminary validation of the use of ion beam analysis and the depth marker technique for erosion and re-deposition studies, with the intent of using IBA to perform erosion measurements on the DCFT and CCFT. Given that the locations of maximum erosion for both thrusters is at the cusps, depth markers would be implanted at these locations. Figure 5-5 shows the planned configuration for these future experiments:

Prior to these particular experiments, validation of this technique was performed. The validating experiments include small scale erosion studies with aluminum and boron nitride samples with implanted depth markers and compared to SRIM data and observation of the effects of heat on the RBS/NRA spectra for a few of these samples.

Effects of other aspects of thruster operation were taken into consideration. Given that plasma thrusters can heat up to a few hundred degrees Celsius during operation, tests were made to ensure that the heat would not cause deviations in the spectra. Vacuum heating was performed on aluminum coupons and RBS/NRA was performed before and after the heating. Comparisons of the two spectra will determine effects, if any, heating would have on the measurements.

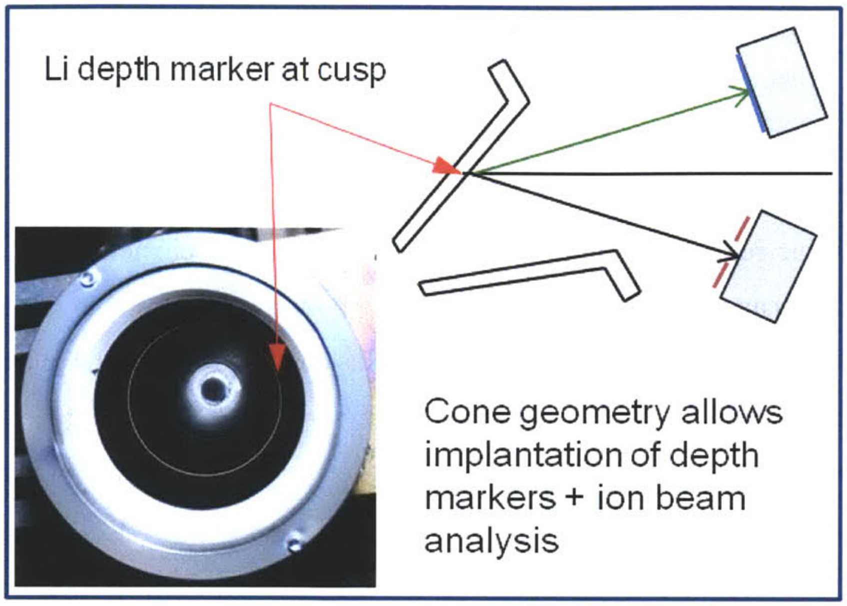

Figure 5-5: Setup for planned ion beam analysis erosion/redeposition experiments with the DCFT [11].

5.5 Validation Procedure

The basic procedure used for validating the depth marker/IBA technique is as follows and as illiustrated in Figure 5-6:

1. Implant marker ions at a given depth (depth depends on ion energy, species).
2. Perform RBS/NRA to create an initial depth profile of the surface.
3. Expose the material to a plasma environment (procedure covered in Section 5.6.2).
4. Perform RBS/NRA on eroded surface.

With SIMNRA, the differences in energy in the NRA spectra before and after exposure were used to compute the change in thickness of the material on top of the depth marker layer. However, the raw data from the NRA trace must be processed before the this calculation may be made.

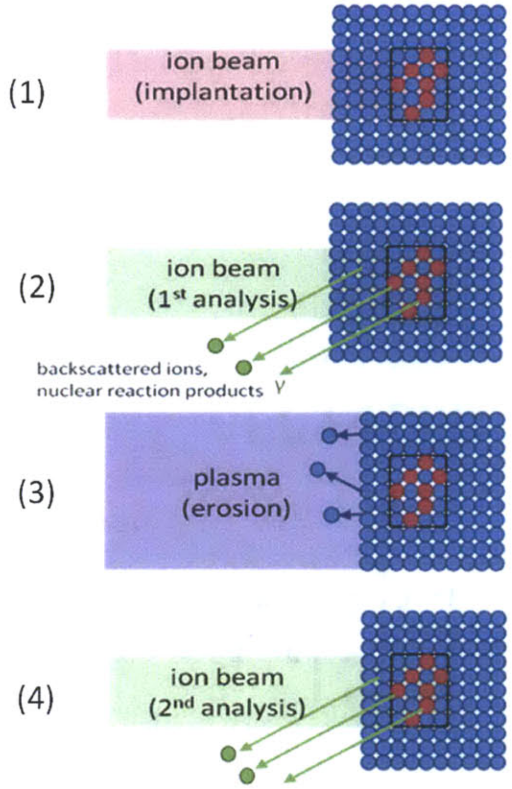

Figure 5-6: Procedure for ion beam analysis [11].

5.5.1 Calibration and Gaussian Fitting

The first step towards processing the NRA results is the fitting of a Gaussian distribution to the raw data, where the mean of the Gaussian curve is the center of the alpha peak:

$$f(x) = \frac{1}{\sigma\sqrt{2\pi}} exp(\frac{-(x-\mu)^2}{2\sigma^2}) \tag{5.3}$$

where the fitting parameters, μ and σ, represent the mean and variance of the curve, respectively. The spectra output is in the form of counts over an array of channels, which must be be converted into energy. The conversion from channels to energy is computed with Equation 5.4:

$$E = a(N_{ch})^2 + bN_{ch} + c \tag{5.4}$$

where, after comparison with spectra of a few calibration sources, the empirical coefficients are a = -2.4 × 10^{-3} keV/ch^2, b = 10.15 keV/ch and c = -132.5 keV. In each calibration process, the same RBS/NRA scans must be performed on at least one other control target in order to create a reference spectra for properly determining the energy calibration of the detector. In the case of these experiments, the control group includes a Polonium 210 check source (α energy of 5.304 MeV), and two aluminum targets with different depths of lithium layers (4.03 μm and 4.84 μm) which have not yet been eroded.

5.5.2 Validation with SRIM Estimates

Once processed and calibrated, the results are then compared to predicted depths of erosion, which were calculated with inputs from Stopping and Range of Ions in Matter (SRIM). Through quantum mechanically modeling collisions between incident ions and atoms within a target material, SRIM computes sputter yields for a material exposed to a plasma with known properties. The sputter yield data from SRIM for aluminum (the material which was used to validate the depth marker/IBA technique) with normal incident ions is shown in Table 5.1:

Table 5.1: SRIM Simulated Sputter Yield, Ar Plasma on Al

Bias Voltage [V]	**Ion Energy** [eV]	**Sputter Yield** [atoms/ion]
0	12	0.0
-25	37	0.0098
-50	62	0.045
-75	87	0.096
-100	112	0.13

With these sputter yields, the expected depth of erosion was calculated with Equation 5.1:

$$d = \int_{t_0}^{t_f} \frac{n_i v_i Y}{n_{Al}} dt \tag{5.5}$$

where Y is the sputter yield, t_0 and t_f are the initial and final times, n_{Al} is the atomic density of aluminum, n_i is the density of ions, and v_i is the ion velocity. The ion velocity is assumed to be the ion sound speed,

$$v_i = \sqrt{kT_e/m_i} \tag{5.6}$$

where k is the Boltzmann constant, T_e is the electron temperature of the plasma, and m_i is the ion mass. The plasma parameters were measured for the helicon plasma generator used to erode the sample while will be discussed in Section 5.6.2. The measured parameters are the ion density ($n_i = 9 \times 10^{16}$ m^{-3}), electron temperature ($T_e = 6$ eV), and plasma potential ($\phi_p = 12$ V).

With these parameters and SRIM-generated sputter yields, the expected erosion depths are shown for each of the experimental cases, which will be discussed in Section 5.6.2.

Table 5.2: Expected Erosion Depths

Case	**Depth of Erosion** [μm]
E_0	0.00
E_1	1.83
E_2	3.66

5.6 Experimental Facilities: Plasma Surface Interactions Surface Center

The studies investigated and detailed in this thesis were performed at the MIT Plasma Surface Interactions Science Center (PSISC). The PSISC features the Cambridge Laboratory for Accelerator Study of Surfaces (CLASS) 1.7 MV tandem Tandetron ion accelerator and the Dynamics of IONic Implantation and Sputtering on Surfaces (DIONISOS) helicon plasma generator. CLASS was used to generated high energy ions for both depth marker implantation and ion beam analysis, and DIONISOS was used to erode the samples.

5.6.1 Cambridge Laboratory for Accelerator Study of Surfaces (CLASS)

As shown in Figure 5.7, the CLASS accelerator consists of a negative ion source, a high-voltage acceleration section, and steering magnets capable of directing the beam down a number of different beamlines.

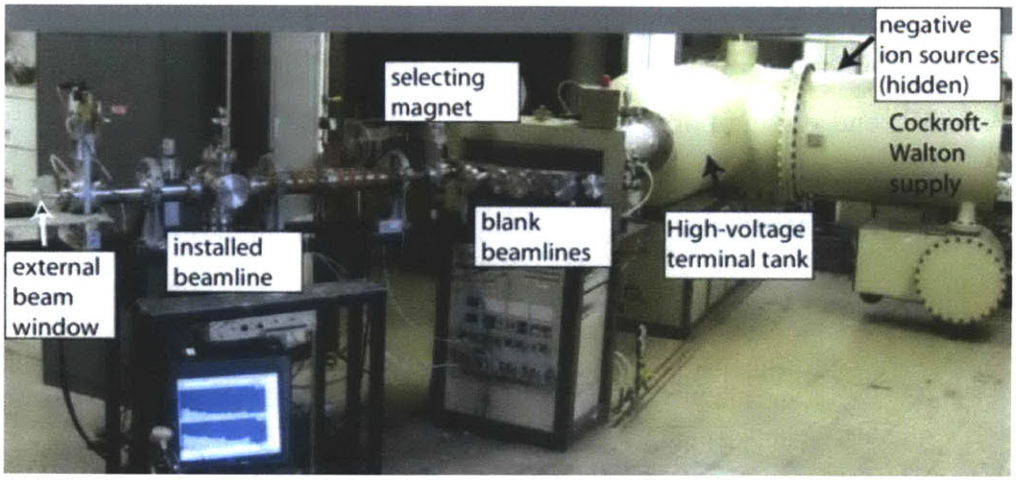

Figure 5-7: Cambridge Laboratory for Accelerator Study of Surfaces (CLASS) 1.7 MV tandem ion accelerator [8].

Cesium Ion Sputtering Source

Within the Tandetron ion accelerator is the cesium ion source, where negative ions are produced through a process involving sputtering and charge-exchange. These ions are produced from a cylindrical target containing the required species for experimentation. In the case of implantation and for generating protons for RBS/NRA, the ions were produced from a lithium cathode; in some cases, titanium hydride were used to generate protons for ion beam analysis. The cathode is biased to -3 kV and bombarded with evaporated Cesium from a heated chamber (T = 1500^o C), which sputter positive ions and neutral particles from the lithium target. The sputtered particles undergo one or more charge-exchange interactions with the Cs accumulated at the surface of the target to become negative ions. These negative ions are then extracted from the source by a -15kV potential. [16].

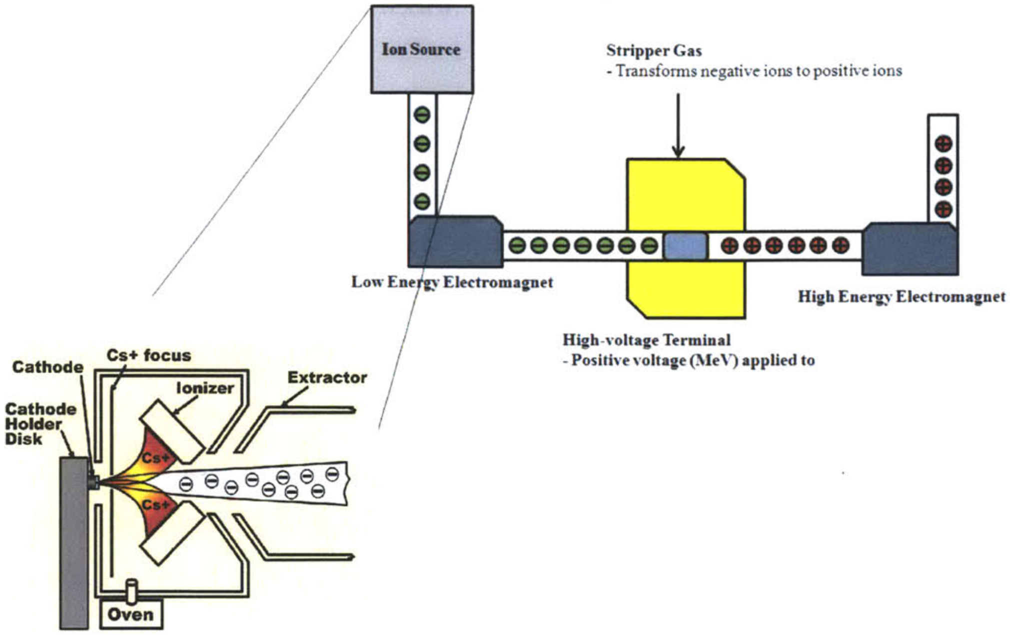

Figure 5-8: CLASS accelerator schematic, with highlights on cesium ion sputtering source. Image of cesium ion sputtering source courtesy of Pelletron.

Electrostatic Focusing of Ion Beam

Ions from the cesium source were electrostatically focused by an Einzel lens in order to prevent beam loss from divergence. A schematic of an Einzel lens is shown in Figure 5-9:

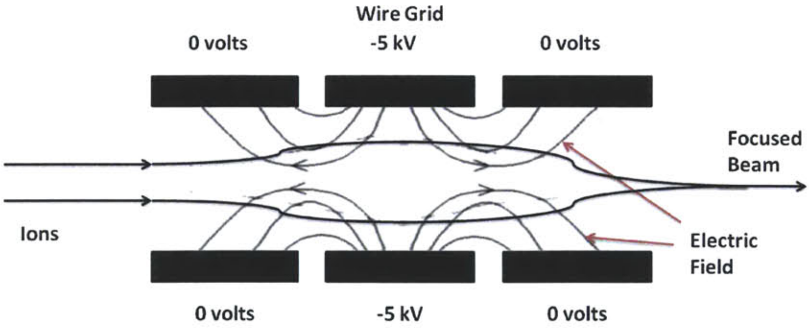

Figure 5-9: Diagram of the electrostatic Einzel lens, which focuses on negative ions from the cesium source.

To focus the ion beam, the Einzel lens creates an axisymmetric electric field between a wire grid at a high voltage (- 5kV) and two co-linear cylinders at ground potential. This design creates an electric field which causes no net acceleration and radially focuses the ions [16].

Ion Accelerator

The collimated ion beam goes through a low energy dipole electromagnet, in order to select ions with the mass and energy desired for the particular experiment. These ions are steered into the next chamber, where a high DC voltage accelerates them. This voltage is provided by an adjustable power supply which consists of a sulfur-hexafluoride (SF_6)-insulated Cockroft-Walton charging network and generates a stable, steady-state terminal voltage of up to 1.7 MV, which is connected directly to the acceleration sections [16]. The energy of the beam is chosen based on the depth of ion penetration desired.

In the next stage of the chamber, the accelerator ionizes the negative ions by having it pass through an electron stripping medium. The stripper medium, nitrogen gas, converts the negative ions accelerated in the first section into positive ions which are subsequently accelerated in the next section. The net effect of this is to double the acceleration potential of the power supply for singly charged ion species. A second acceleration section, over which the potential drops from the maximum positive potential to ground potential, further boosts the velocity of the ions [16].

The accelerated ion beam is then further focused using the high energy electromagnet. The high energy electromagnet selects the beam with the directed charge state and steers it down to the beam line used for ion beam analysis.

The result of this process is a monoenergetic, focused ion beam consisting of a single species. The diameter of the beam is on the order of a millimeter, and the beam current produced ranges from 1 to a few 1000's of μA.

The current used is relative to the application of the ion beam. For RBS/NRA, higher current results in more counts in the spectra sooner, which drastically reduces the amount of time needed to obtain the results (hours to minutes). However, in the case of depth marker implantation, high current could potentially damage the surface

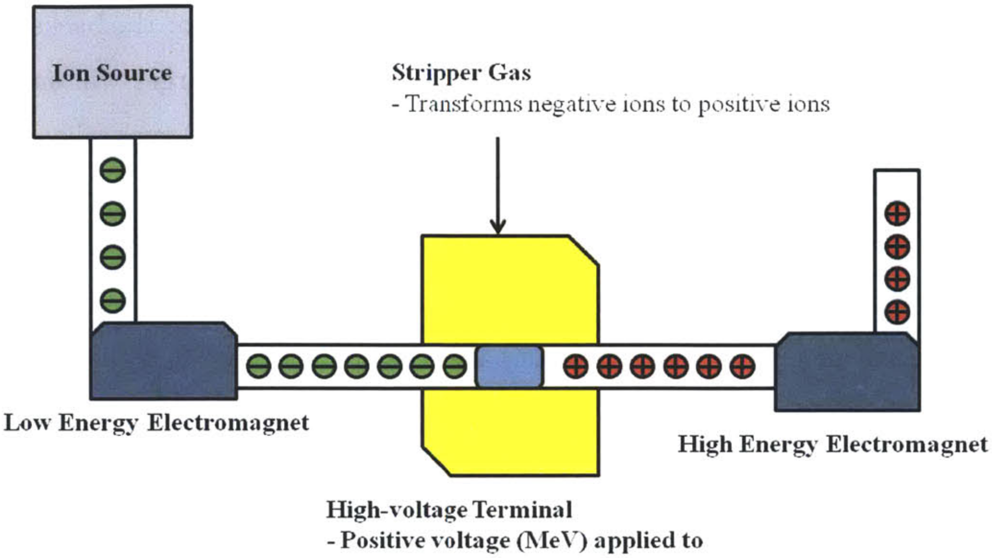

Figure 5-10: CLASS accelerator schematic.

of the target. Ideally, the current produced should be relatively low (100's of μA). The concentration and depth of the marker layer are determined by the amount of time spent implanting and the energy of the beam, respectively.

5.6.2 Setup of Diagnostics Equipment

In general, any RBS/NRA experiment requires the following three components:

- Ion source.
- Particle accelerator capable of accelerating ions from the source to high energies (1-3 MeV)
- Detectors for measuring the energies of the backscattered ions and, in the case of NRA, nuclear reaction byproducts.

In the PSISC, the first two components are represented by the CLASS accelerator, which has the cesium ion sputter source and the tandem accelerator. The detectors, which are placed in the beamline where the target material for RBS/NRA experiments is located, are silicon surface barrier detectors, which measure the backscattered energy and nuclear byproduct.

The silicon surface barrier detectors operate in the following fashion: the backscattered protons and byproducts from the proton collisions with the target will subsequently collide with the detector, which has a thin layer (100 nm) of P-type silicon on an N-type substrate, and lose energy due to inelastic scattering from the electrons. Some of these electrons gain enough energy to overcome the band gap between the semiconductor valence and conduction bands. As a result, each ion incident on the detector produces one or more electron-hole pairs, the number of which is dependent on the energy of the ion. These pairs are detected by applying a voltage across the detector and measuring the current, providing an effective measurement of the ion energy [10].

The placement of the two detectors, which are used for RBS and NRA independently, is shown in Figure 5.11.

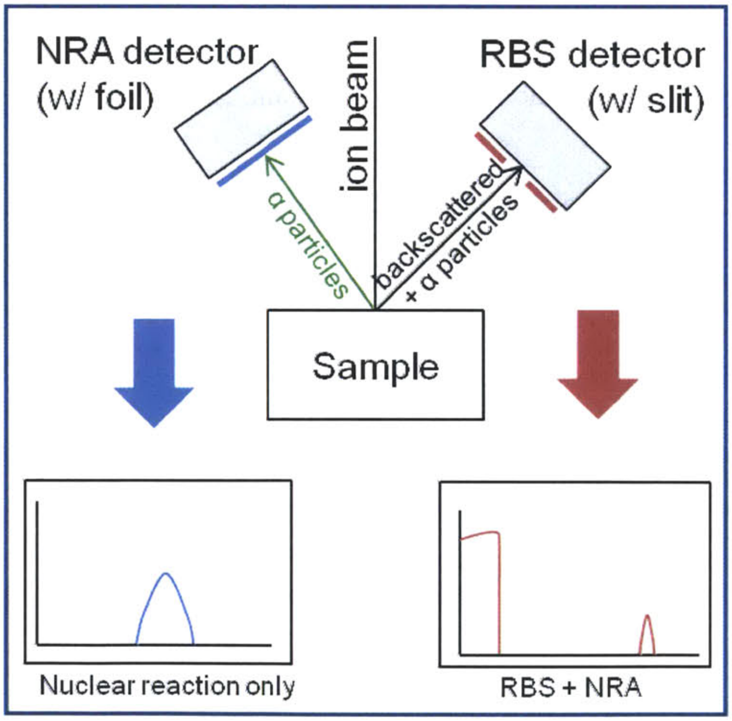

Figure 5-11: Setup configuration for NRA and RBS detectors and respective spectra [11].

As noted in Section 5.3.1, the RBS detector can measure both backscattered protons and α particles and can be used to determine if surface composition has changed. In contrast, the NRA detector has an aluminum foil covering the silicon layer, which prevents low-energy particles from reaching the detector.

5.6.3 Helicon Plasma Erosion

Once implantation and initial surface profiling is performed, DIONISOS is used to erode the target surface. DIONISOS features a helicon plasma source, with typical plasma parameters of $n_e = 10^{17}$ to 10^{18} m^{-3} and T_e = 1-10 eV with Argon gas.

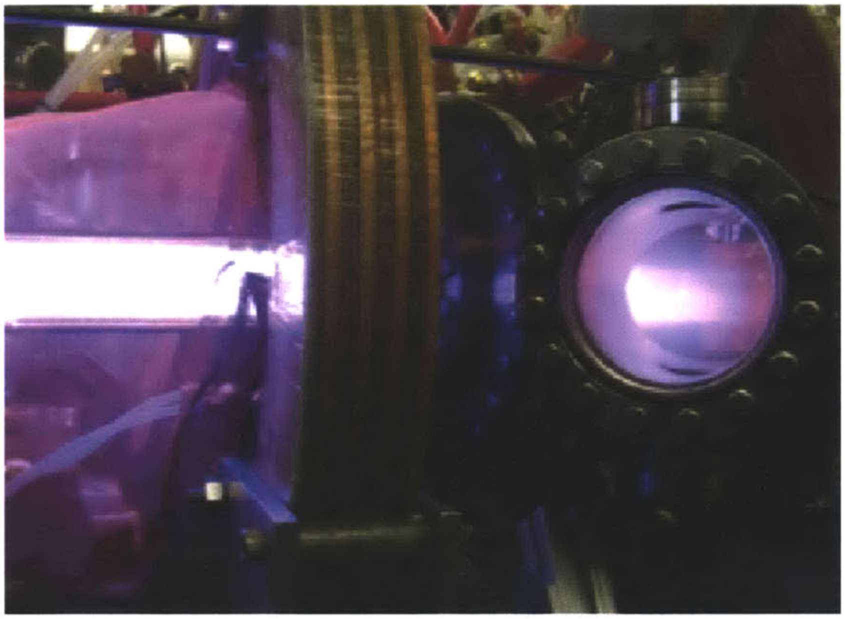

Figure 5-12: DIONISOS helicon-generated plasma eroding a sample.

As a helicon plasma source, DIONISOS generates plasma through helicon waves induced with radio frequency heating. The RF-generated plasma is then confined within strong electromagnets (0.1 T) and driven to a biased surface which, in most cases, is the target. The bias of the target determines the energy of the incident ions and is adjusted with regards to the target material, the plasma ion species, and the sputtering yield predicted by SRIM.

One supplemental use of DIONISOS is in-situ RBS/NRA measurements of a target exposed to a plasma. In-situ ion beam analysis is enabled by the extremely large difference in plasma and beam energies, the fact that plasma is transparent to ion beam and scattered particles, and the fact that IBA techniques are valid in the presence of a magnetic field [8]. As such, these measurements allow for real-time tracking of dynamic processes of near-surface, such as hydrogen impurity concentrations, surface erosion and re-deposition [11]. However, this option is not explored within this thesis.

Instead, DIONISOS was used extensively to erode coupons for the self-consistent validating studies. One such study involved three aluminum 6061 disk samples (3 cm diameter) which were implanted with lithium depth marker layers. These samples were serially placed inside of DIONISOS, where they were exposed to the helicon-generated plasma. For one sample, hereafter designated as UE_1, the target was not biased and, as such, encountered only ions at the plasma potential (12 V) and was exposed to plasma in DIONISOS for 30 minutes.

The other two samples, E_1 and E_2, were both biased and thus had sputtering from higher energy ions (112 eV, from a -100 V bias). For both cases, a specialized "startup" procedure was used to incrementally increase the bias in order to prevent arcing to the target holder. The startup procedure is as follows:

- 5 min. erosion with 0V bias
- 5 min. erosion with -25 V bias
- 5 min. erosion with -50 V bias
- 5 min. erosion with -75 V bias
- 5 min. erosion with -100 V bias

After the startup procedure, the erosion procedure begins to differ for E_1 and E_2. For E_1, the startup procedure is succeeded by a 30 minute exposure to the plasma with -100 V bias. E_2 underwent the same procedure as E_1 but also included a second iteration of the startup procedure and 30 minute plasma exposure. As a result, the additional procedure for E_2 would, in theory, double the eroded depth.

5.7 Preliminary Results Summary

For the three cases, the raw NRA spectra were compiled and their calibrated energy curves, as compared to the check sources, are shown in Figure 5-13. As expected, the samples exposed to plasma with a bias (E_1 and E_2) had a higher energy alpha peak than the sample without a potential, and the sample exposed longer (E_2) had the highest energy peak of all three spectra. This is because the more material is eroded, the less the initial α particle energy is attenuated. This is a qualitative validation of the depth marker/NRA technique.

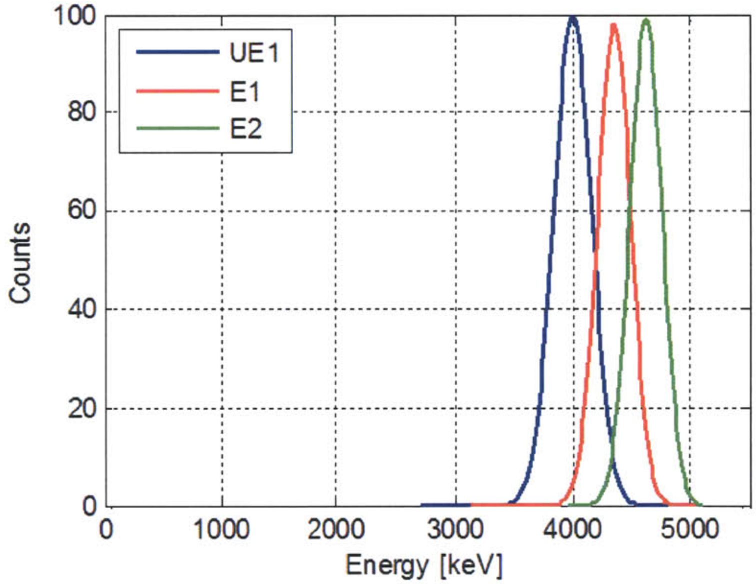

Figure 5-13: NRA trace of aluminum coupons UE1, E1, and E2.

5.7.1 Interpretation and Discussion of Results

With these energy spectra, SIMNRA was used to calculate the measured erosion. In each case, the simulated change in layer depth due to erosion, and the corresponding shift in energy of the alpha peak was matched to the calibrated experimental Gaussian curves. Table 5.3 displays the experimental results and the SRIM predicted results:

The relative errors for the E_1 and E_2 are 8.2 % and 4.6 %, respectively. This relative error, however, must take into account the uncertainty of the plasma mea-

Table 5.3: Energy Shift from Experiment and Erosion Determination

Case	**ΔE** [keV]	**Δd** [μm]	**SRIM Δd** [μm]
E_0	0	0	0
E_1	350	1.98	1.83
E_2	617	3.49	3.66

surements made for the SRIM predictions. The uncertainty of the Langmuir probe data are:

- $n_i = 9 \times 10^{16} \pm 1 \times 10^{16}$ m^{-3}
- $T_e = 6$ eV $\pm$ 1 eV
- $\phi_p = \pm$ 1 eV

When you account for the uncertainty in the SRIM sputtering calculations:

$$d_{sputtering} = \int_{t_0}^{t_f} \frac{n_i \sqrt{\frac{kT_e}{m_i}} Y}{n_{Al}} dt \tag{5.7}$$

$$U = \frac{\Delta d_{sputtering}}{d_{sputtering}} \tag{5.8}$$

where U is the uncertainty. We have a collective uncertainty of 1 ± 0.2 or 20 % uncertainty in the expected erosion based on SRIM data and Langmuir probe measurements. Furthermore, there is an additional uncertainty from the Gaussian fits, where Δ d/d is approxlimated by σ/μ. For E_1, which has a mean of 501.1 and variance of 18.2, and E_2, which has a mean of 536.1 and a variance of 18.1, the uncertainty for both cases is around 4 %. This sums up to a total of 24 % of uncertainty.

Given that the relative errors are well within the uncertainty, it can be concluded that the actual erosion rates measured by the depth marker/NRA technique match the expected erosion rates from the SRIM-based predictions. Thus, we have self-consistent validation of the technique.

To eliminate the uncertainty from the Gaussian fits in the future, the variance should be decreased. This can be accomplished by decreasing the spread of the alpha peak and/or increases the total number of counts measured by the detector (increasing proton flux to the target or allow the RBS/NRA process to take longer to collect more counts).

5.7.2 Effects of Heating

An ancillary experiment performed in preparation for the use of the depth marker/NRA technique for erosion studies with the DCFT was to investigate the effects of heating on the implanted samples. Given that normal thruster operations can heat DCFT to steady state temperatures of 200^o C or more, it is critical to see if the NRA peak would be affected. To determine the effects, an implanted aluminum sample was depth profiled, heated to 300^o C, and then profiled again. The two NRA traces can be seen in Figure 5-14:

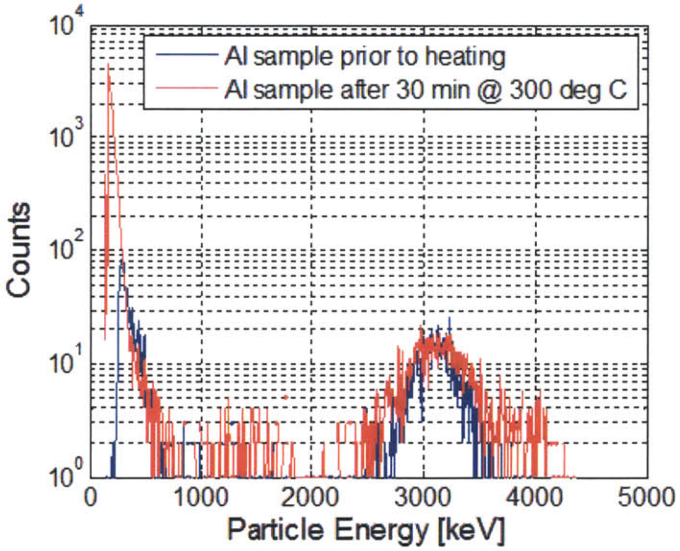

Figure 5-14: NRA trace of aluminum coupon before and after being heated to 300^o C for 30 minutes.

As observed in the spectra above, heating does have effects on the raw data in that it widens the peak. However, this widening does not adversely affect NRA, as the center of the peak itself is unchanged and the technique is still applicable.

As a result, it can be concluded that any heating from thruster operation would not adversely affect NRA measurements with the depth marker for relatively short thruster operation periods.

Chapter 6

Conclusions and Future Work

A prototype Cylindrical Cusped-Field Thruster has been developed and built based on some of the suggested improvements for the Diverging Cusped-Field Thruster. The CCFT, which features a cylindrical discharge chamber, has a magnetic topology aimed to create more collimated plasma plumes. Based on kinetic simulations performed with the Plasma Thruster particle-in-cell (PTpic) code, thruster performance, plume characteristics, thruster longevity, and erosion profiles has been predicted at low flow rates with varying anode power. With preliminary testing of the CCFT in the MIT Space Propulsion Laboratory, some qualitative results have validated some predictions of the plasma plume and erosion profile. However, comprehensive and quantitative testing of the thruster remains to be performed. In particular, the phenomena of high anode current must be further investigated and the hypothesis of high double ion fractions must also be tested with a time-of-flight experiment.

In addition, a new diagnostic tool, the depth marker/NRA techqnie, for plasma thruster erosion and re-deposition studies has been self-consistently validated. This technique has been tested on aluminum samples and its result will pave the way for continued testing and eventual application on the DCFT and the CCFT.

6.1 CCFT Thruster Recommended Studies

Performance characterization of the CCFT is to be performed, which includes energy and current measurements of the thruster with the use of instruments such as a Faraday probe and Retarding Potential Analyzer (RPA), similar to studies performed with the DCFT [5]. In addition, direct thrust measurements can be performed with the use of the Milli-Newton Thrust Stand (MiNTS), which was developed by R. Daspit [25]. Last, high frequency measurements of the anode current should be performed in order to see if the bi-modal nature of the DCFT is present in the CCFT.

Faraday Probe

Faraday probes measure ion current density by collecting ions incident on a charged plate from a thruster plume. A schematic overview of a typical Faraday probe is shown in Figure 6-1.

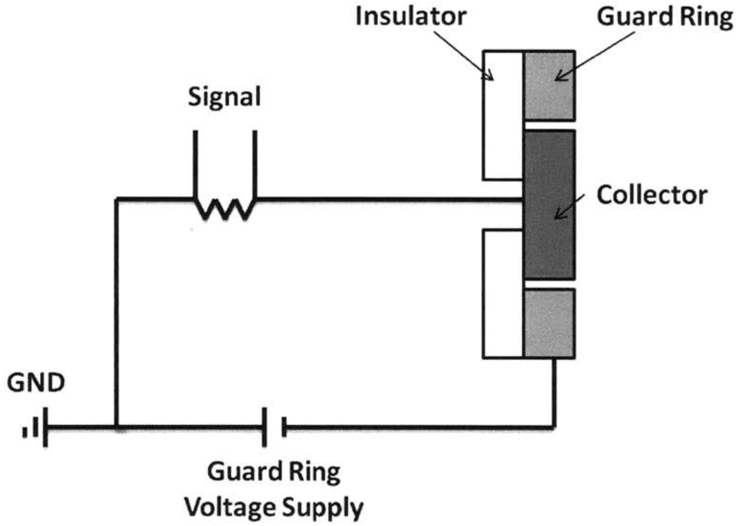

Figure 6-1: Basic schematic of the Faraday probe used in the experiments.

To repel incident electrons, a negative potential of 30V below the plasma floating potential is applied to the tungsten plate while the ions are collected in the collector plate. The cumulated ion current collected is assumed to be the beam current of the thruster. A guard ring is included around the collector plate to repel ions not collinear to the probe geometry and mitigate non planar electric fields that could form on the probe edges. The current density, at the location of the probe is approximately

$$j = I_p/A_p \tag{6.1}$$

where j is the current density, I_p is the collected current [A] and A_p is the probe collector area [m^2]. The probe used in this study is the same probe used in the initial performance testing of the DCFT [?] and has a collector diameter of 4.45mm, with a 6.35mm guard ring.

With the current density, the total beam current can be calculated by the following equation:

$$j = 2\pi R^2 \int_0^{\pi/2} j(\phi) sin(\phi) d\phi \tag{6.2}$$

where R is the fixed radial distance from the thruster exit plane and ϕ is the azimuthal angle.

Retarding Potential Analyzer (RPA)

A RPA, schematic shown in Figure 6-2, was designed to measure the distribution of ion energies at a fixed probe location. Unlike Faraday probes, RPAs collect ions above a threshold energy through the use of a positively biased retarding grid. In order to maintain only ion flux to the collector, another grid is placed before the ion retarding grid and negatively biased below the floating potential to repel electrons. Finally, a floating grid is placed in front of the electron repelling grid to reduce probe perturbations on the surrounding plasma.

The probe used in this thesis was on loan from the SPL ion Electrospray Propulsion System (iEPS) research group. Through varying the voltage of the retarding grid and measuring the resulting current on the collector plate, a current-voltage relationship can be derived. The derivative of this current-voltage curve is proportional to the ion energy distribution, as shown in Equation 6.3:

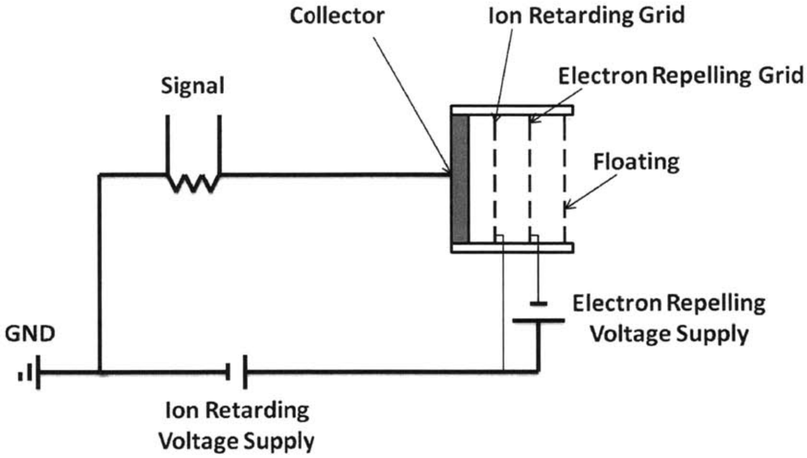

Figure 6-2: Basic schematic of the Retarding Potential Analyzer used in the experiments.

$$\frac{dI}{dV} = -qAn_i(\frac{2eV}{m_i})^{1/2}\frac{1}{V_a}f(\xi) \tag{6.3}$$

where q is the elementary charge (assuming singly-charged ions), A is the area of the collector plate, n_i is the ion density, ξ = V/V_a and $f(\xi)$ is the ion distribution function.

Milli-Newton Thrust Stand (MiNTS)

The MiNTS system is a torsional-style thrust stand design which can measure thrust in the range of 3-20 mN, with a resolution of ± 0.2 mN [25]. The system has been used for thrust measurements of the DCFT, as seen in Figure 6-3, and can be easily adapted for the CCFT.

Instrumentation Setup

The Faraday and RPA probes are to be installed 10 centimeters from the CCFT exit. Figure 6-4 shows the physical arrangement of the instrumentation setup with respect to the CCFT and the cathode stage.

The two probes are placed on a mechanized rotary arm system, which will position the two instruments in different positions of the plasma plume, and the CCFT will be

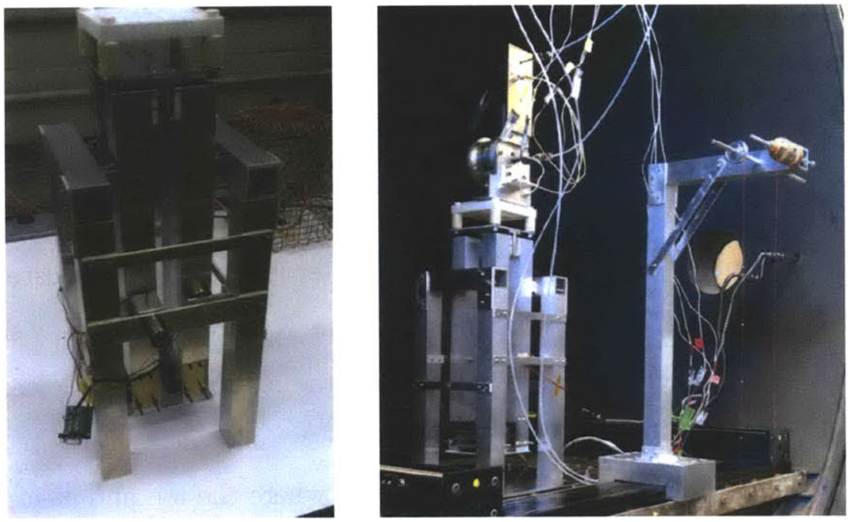

Figure 6-3: Milli-Newton Thrust Stand (left), Setup of DCFT/MiNTS and calibration equipment in Astrovac (right) [12].

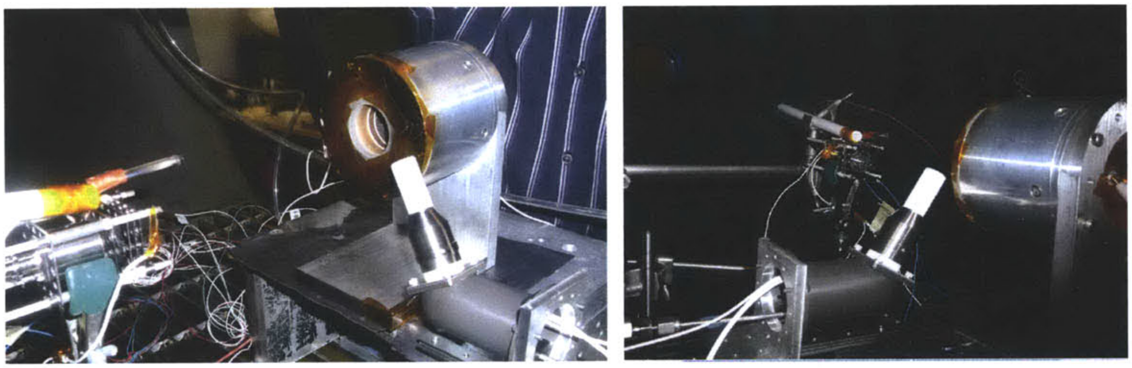

Figure 6-4: Front view of experimental setup (left), Back view of the experimental setup in Astrovac.

placed on the MiNTS to measure the thrust. To measure the high frequency anode current, a Tektronix P6016 current probe is attached on the anode power wiring and its output is read with an oscilloscope.

6.1.1 Continued Numerical Simulations

Extensive simulations have been performed for the CCFT over a range of anode power (75-300 W) for low anode flow (4 sccm Xe). However, as noted in section 4.4 of Chapter 4, the predicted floating body potential (100 V) used as a boundary condition for these simulations is not accurate, as the experimentally measured potential of the

CCFT ranged in the low 10's of volts. Additional simulations with the corrected boundary condition should be performed.

High Flow Simulations

As a guide to continued experimentation and better insight to the thruster behavior, high flow (6-8.5 sccm Xe) simulations should be run.To perform high flow simulations, the mesh must be further refined to account for the effects of higher plasma density and, a result, changed Debye lengths. This mesh refinement is to be performed primarily in the discharge region of the thruster, where the ion and electron density are predicted to be at their maximum.

The erosion predictions generated by the high flow simulations will be useful for comparing the CCFT's longevity to the DCFT's, as they are closer in metrics to the DCFT operating conditions (optimal conditions: 8.5 sccm Xe, 242 W anode power).

6.2 Ion Bean Diagnostics Recommended Studies

For the continued validation of the depth marker/NRA technique, a number of experiments should be performed. Given that boron nitride is the material most commonly used as a dielectric insulator for the DCFT, CCFT, and many commercial Hall-effect thruster, additional experiments with boron nitride coupons should be performed prior to employing the method with the DCFT. These experiments, which would include the heated measurement, would follow the same methodology explained in this thesis and previously employed with the aluminum samples.

6.2.1 External Validation Studies

Validation of the technique can be made through measuring the erosion with other instruments and methods. For the coupon validation, with the use of a high-sensitivity (± 0.1 μg), low mass balance, the mass difference of the coupon before and after erosion can be used to compute the eroded depth on the surface.

Another study which could measure the eroded depth of the material directly would be the use of high-resolution optical microscopy (± 0.1 μm) on the surface of the target before and after plasma exposure. However, the limitations of this technique would be the additional requirements of special surface treatment and material handling before the experiment is run. Without proper preparation of the coupons, regular surface imperfections may cause errors in measurements.

6.2.2 Validation with the DCFT

With basic validation performed, a high level validation of the depth marker/NRA technique would be to measure the erosion at the cusps for the DCFT, operating at the conditions used in the AFRL longevity tests. Favorable comparisons between these measurements and the existing erosion data from the DCFT would give strong evidence of the accuracy and validity of the use of ion beam analysis for erosion and re-deposition studies.

Bibliography

[1] Daniel G. Courtney. Development and Characterization of a Diverging Cusped Field Thruster and a Lanthanum Hexaboride Hollow Cathode. Master's thesis, MIT, Department of Aeronautics and Astronautics, 2008. 21, 27, 30, 51

[2] D. Courtney and M. Martinez-Sanchez. Diverging Cusped-Field Hall Thruster (DCHT). In *30th International Electric Propulsion Conference*, Florence, Italy, 17-20 Sept, 2007, IEPC-2007-39.

[3] P. Lozano and M. Martinez-Sanchez. Fundamentals and definitions. In *MIT 16.522 Space Propulsion: Lecture Notes*. 20

[4] G. Kornfeld, N. Koch, and H.-P. Harmann. Physics and Evolution of HEMP-Thrusters. In *30th International Electric Propulsion Conference*, Florence, Italy, 17-20 Sept, 2007, IEPC-2007-39. 27

[5] S. Gildea, M. Martinez-Sanchez, M. Nakles, and W. Hargus. Experimentally Characterizing the Plume of a Divergence Cusped-Field Thruster. In *31st International Electric Propulsion Conference*, University of Michigan, Ann Arbor, Michigan, USA, 20-24, 2009, IEPC-2009-259. 100

[6] D. Courtney, P. Lozano, and M. Martinez-Sanchez. Continued Investigation of Diverging Cusped Field Thruster. In *44th AIAA/ASME/SAE/ASEE Joint Propulsion Conference & Exhibit*, Hartford, CT, 21-23 July 2008, AIAA 2008-4631.

[7] S. Gildea, T. Matlock, M. Martinez-Sanchez, and W. Hargus. Erosion Measurements in a Diverging Cusped-Field Thruster. In *32nd International Electric Propulsion Conference*, Wiesbaden, Germany, 11-15 Sept, 2011, IEPC-2011-149. 22, 23, 28, 29, 39, 78

[8] R. Sullivan. Plasma-Surface Interactions in Thrusters and Tokamaks: An Opportunity for Collaboration Between the Fusion and Propulsion Communities. In *MIT PSFC Spring Seminar Series*, Cambridge, MA, 24 February, 2012. 23, 81, 88, 94

[9] M. Mayer. Rutherford Backscattering Spectrometry (RBS). In *Workshop on Nuclear Data for Science and Technology- Materials Analysis*, Trieste, Italy, 19-30 May, 2003. 80

[10] EAG: Evans Analytical Group Materials Characterization. Rutherford Backscattering Spectrometry: Spectroscopy. http://www.eaglabs.com/mc/rbs-spectroscopy.html, Accessed May 19, 2013. 92

[11] R. Sullivan. The Development of Novel Diagnostic Techniques for Plasma Surface Interaction Studies in Tokamaks and Thrusters. In *MIT Plasma Science and Fusion Center Rising Stars Symposium*, Cambridge, MA, 5 March, 2013. 82, 84, 85, 92, 94

[12] R. Daspit, P. Lozano, and M. Martinez-Sanchez. Characterization and Optimization of a Diverging Cusped Field Thruster wih a Calibrated Horizontal Accelerometer. In *47th AIAA/ASME/SAE/ASEE Joint Propulsion Conference & Exhibit*, San Diego, CA, USA, 31 July-3 August, 2011, AIAA 2011-6069. 103

[13] T. Matlock, S. Gildea, F. Hu, N. Becker, P. Lozano, and M. Martinez-Sanchez. Magnetic Field Effects on the Plume of a Diverging Cusped-Field Thruster. In *46th AIAA/ASME/SAE/ASEE Joint Propulsion Conference & Exhibit*, Nashville, TN, USA, 25-28 July, 2010, AIAA 2010-7104. 33

[14] Busek Co. Inc. Hollow Cathodes. http://www.busek.com/indexhtmfiles/70008509 revA.pdf, Accessed May 17, 2013. 45

[15] Taylor S. Matlock. An Exploration of Prominent Cusped-Field Thruster Phenomena: The Hollow Conical Plume and Anode Current Bifurcation. PhD dissertation, MIT, Department of Aeronautics and Astronautics, 2012.

[16] Harold S. Barnard External Proton Beam Analysis of Plasma Facing materials for Magnetic Confinement Fusion Applications. Master's Thesis, MIT, Department of Nuclear Science and Engineering, 2009. 89, 90

[17] Stephen R. Gildea. Development of the Plasma Thruster Particle-in-Cell Simulator to Complement Empirical Studies of a Low-Power Cusped-Field Thruster. PhD dissertation, MIT, Department of Aeronautics and Astronautics, 2012.

[18] John T. Yim. Computational Modeling of Hall Thruster Channel Wall Erosion. PhD dissertation, University of Michigan, Department of Aerospace Engineering, 2008. 71

[19] Shannon Y. Cheng Modeling of Hall Thruster Lifetime and Erosion Mechanisms. PhD dissertation, MIT, Department of Aeronautics and Astronautics, 2007. 71

[20] T. Matlock, F. Hu, and M. Martinez-Sanchez. Controlling Plume Divergence in a Cusped-Field Thruster. In *32nd International Electric Propulsion Conference*, Wiesbaden, Germany, 11-15 Sept, 2011, IEPC-2011-178. 33

[21] J. Szabo, M. Martinez-Sanchez, and O. Batishchev. Fully Kinetic Hall Thruster Modeling. *27th International Electric Propulsion Conference*, Pasadena, CA, 15-19 October, 2001, IEPC-01-341.

[22] Y. Garnier, J. Roussel, and J. Bernard. Low-energy Xenon sputtering of ceramics investigated for stationary plasma thrusters. *Journal of Vacuum Science and Technology*, A 17(60: 3246-3254, Nov. Dec. 1999.

[23] S. Gildea, T. Matlock, M. Martnez-Snchez, and W. Hargus, Jr. Erosion Measurements in a Low-Power Cusped-Field Plasma Thruster. *Journal of Propulsion and Power.*, doi: 10.2514/1.B34607, 2013. 74, 77

[24] A. Smyrnov, Y. Raitses, and N. Fisch. Experimental and theoretical studies of Cylindrical Hall Thrusters. *Physics of Plasmas*, V. 14, No. 057106, 2007. 27

[25] Ryan M. Daspit. Performance Characterization and Optimization of a Diverging Cusped Field Thruster with a Calibrated Counter-Weighted Millinewton Thruster Stand. Master's thesis, MIT, Department of Aeronautics and Astronautics, 2012. 100, 102

[26] Stephen R. Gildea. Fully Kinetic Modeling of a Divergent Cusped-Field Thruster. Master's thesis, MIT, Department of Aeronautics and Astronautics, 2009.

[27] Yassir Azziz. Instrument Development and Plasma Measurements on a 200-Watt Hall Thruster Plume. Master's thesis, MIT, Department of Aeronautics and Astronautics, 2003. 52

[28] J. Tesmer and M. Nastasi. *Handbook of Modern Ion Beam Materials Analysis.* Materials Research Society, 1995. 78

[29] K. Oura *Surface Science: An Introduction.* Advanced Texts in Physics, Springer, 2003. 80

[30] Charles Kennedy Birdsall and A. Bruce Langdon. *Plasma Physics Via Computer Simulation.* McGraw-Hill Book Company, New York, 1985. 55, 62

[31] W. Chu, J. Mayer, and M. Nicolet. *Backscattering Spectrometry.* Academic Press, 1978.

Appendix A

Cylindrical Cusped-Field Thruster SolidWorks Drawings

All units are in centimeters.

Side View

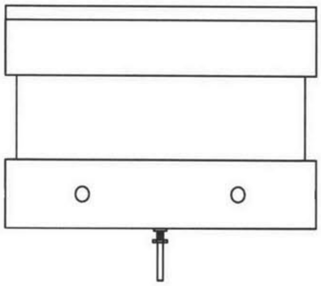

Top View

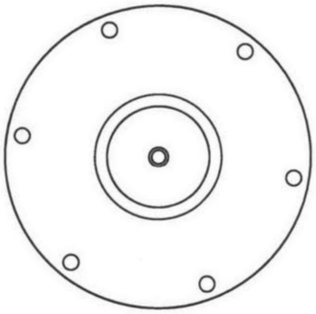

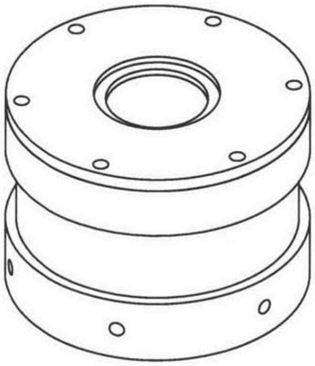

Bottom View

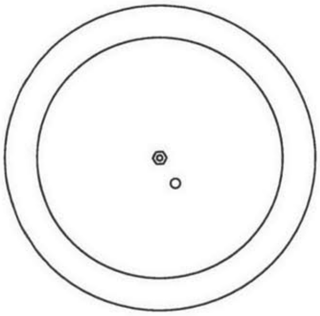

SolidWorks Student Edition.
For Academic Use Only.

TITLE:

Assembly

SIZE A
DWG. NO. Assembly1
REV
SCALE: 1:2
WEIGHT:
SHEET 1 OF 10

5 4 3 2 1

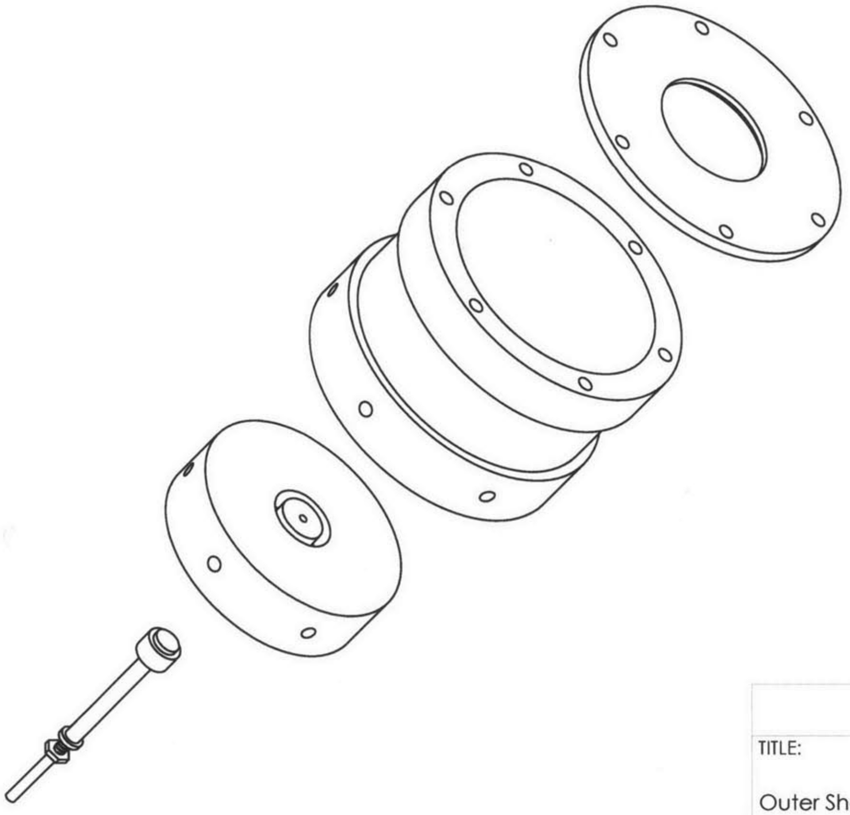

SolidWorks Student Edition.
For Academic Use Only.

TITLE: Outer Shell, Base, Anode Assembly		
SIZE A	DWG. NO. Assembly1	REV
SCALE: 1:2	WEIGHT:	SHEET 2 OF 10

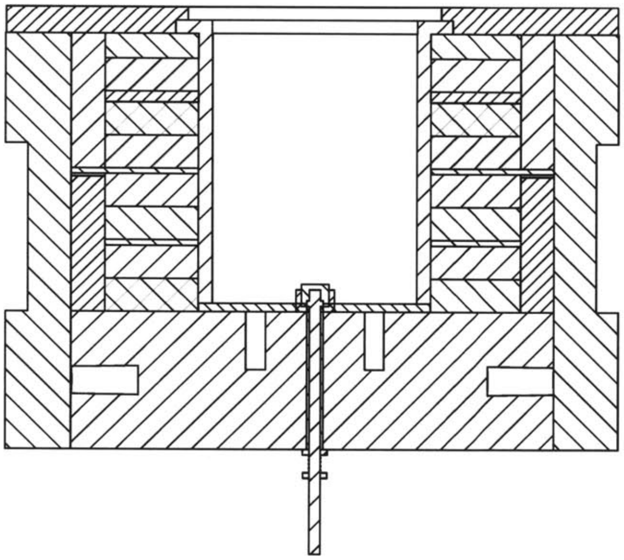

DETAIL F
SCALE 1 : 1

TITLE:		
SIZE **A**	DWG. NO. Assembly1	REV
SCALE: 1:2	WEIGHT:	SHEET 3 OF 10

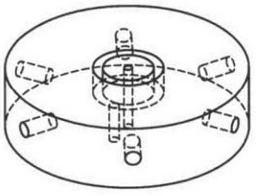

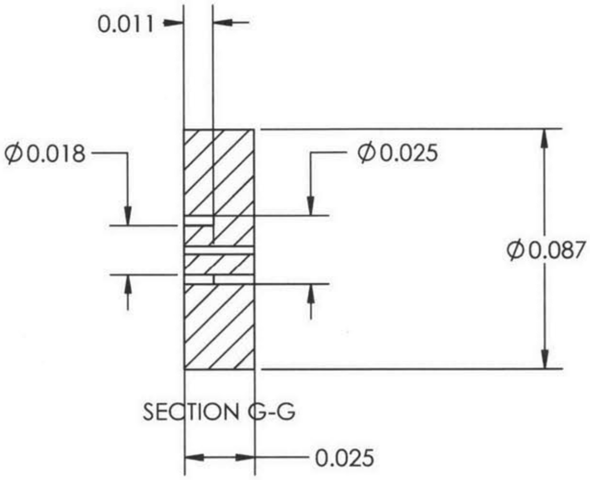

SECTION G-G

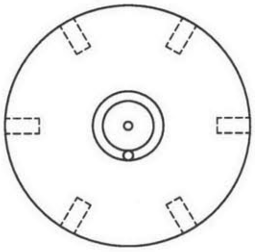

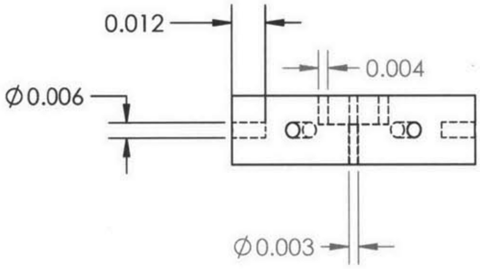

TITLE: Base Core		
SIZE **A**	DWG. NO. Assembly1	REV
SCALE: 1:2	WEIGHT:	SHEET 4 OF 10

5 4 3 2 1

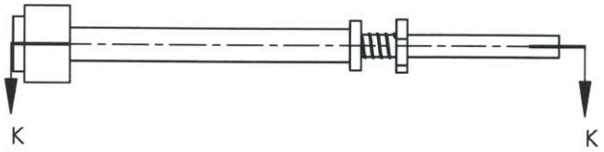

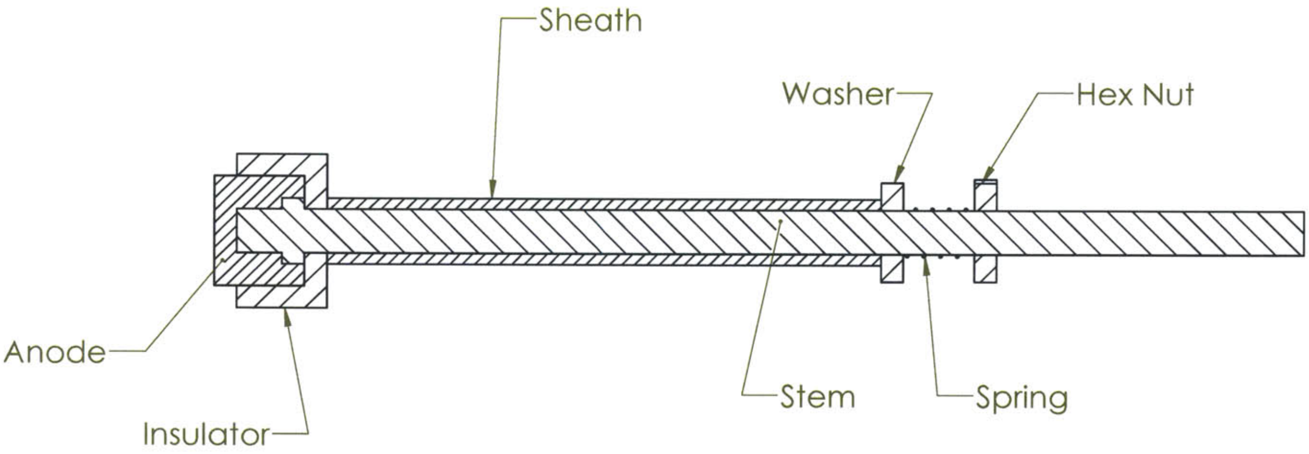

DETAIL M
SCALE 4 : 1

TITLE: Anode		
SIZE A	DWG. NO. Assembly1	REV
SCALE: 2:1	WEIGHT:	SHEET 5 OF 10

SolidWorks Student Edition.
For Academic Use Only.

5 4 3 2 1

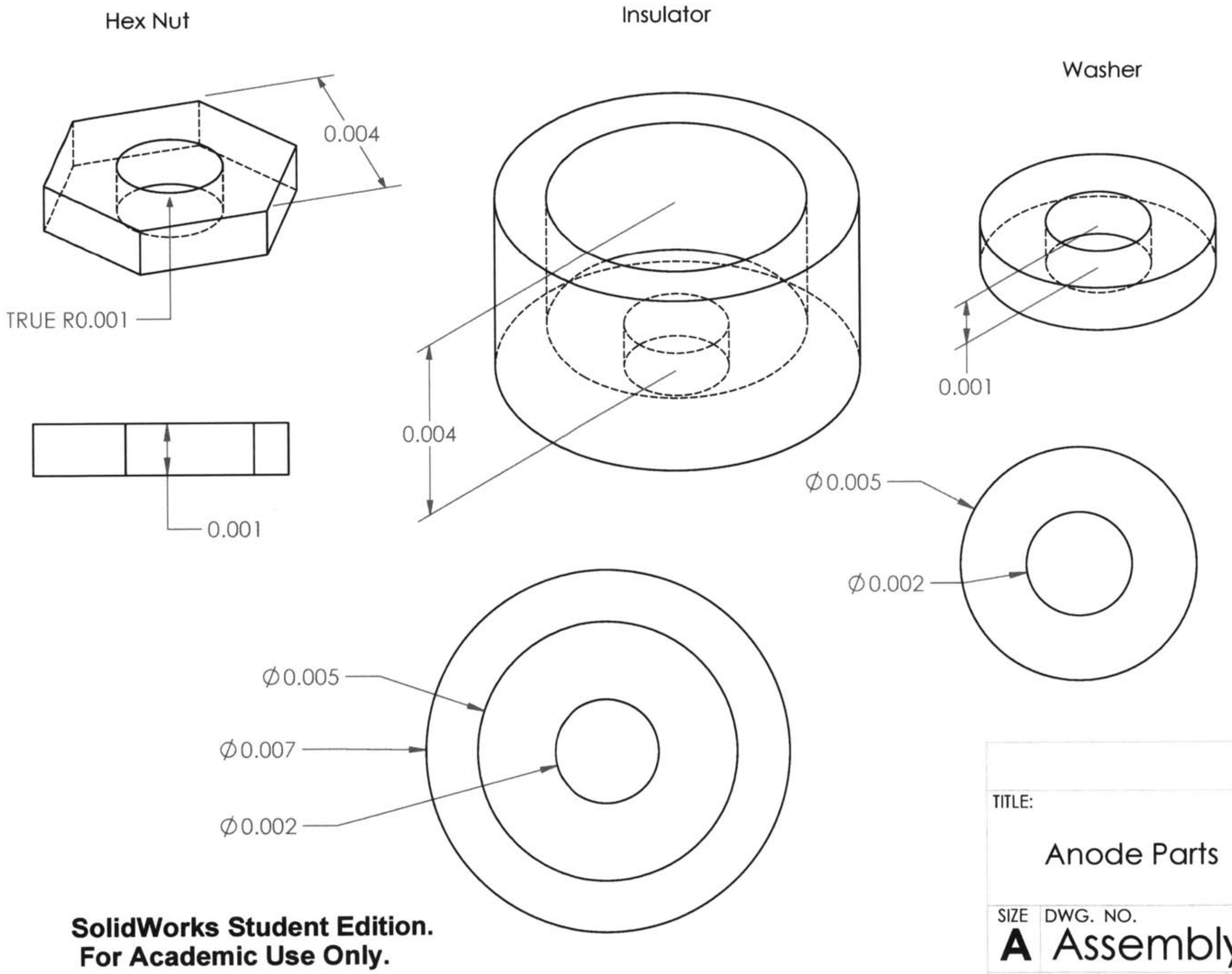

TITLE:

Anode Parts

SIZE	DWG. NO.	REV
A	Assembly1	
SCALE: 10:1	WEIGHT:	SHEET 6 OF 10

5 4 3 2 1

Anode Stem

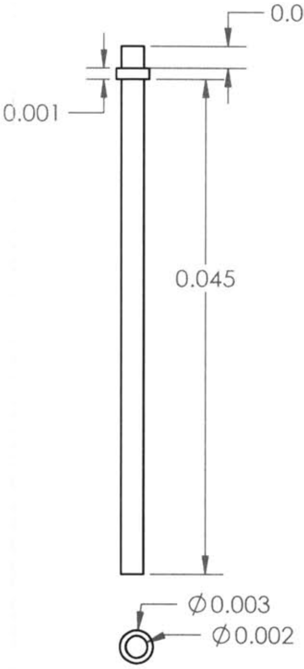

Anode

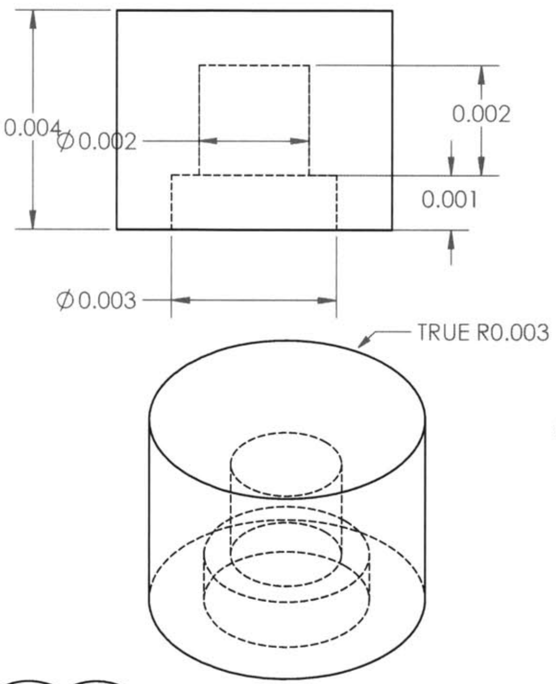

Stem Sheath

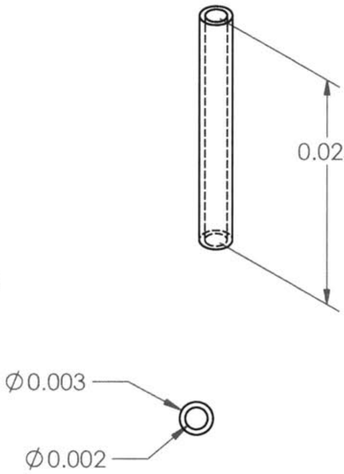

Spring

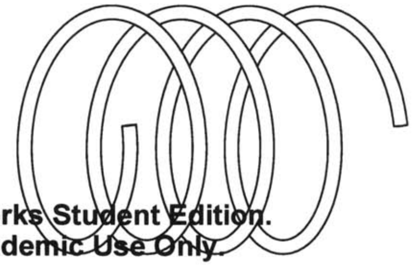

TITLE: Anode Parts		
SIZE **A**	DWG. NO. Assembly1	REV
SCALE: 2:1	WEIGHT:	SHEET 7 OF 10

5 4 3 2 1

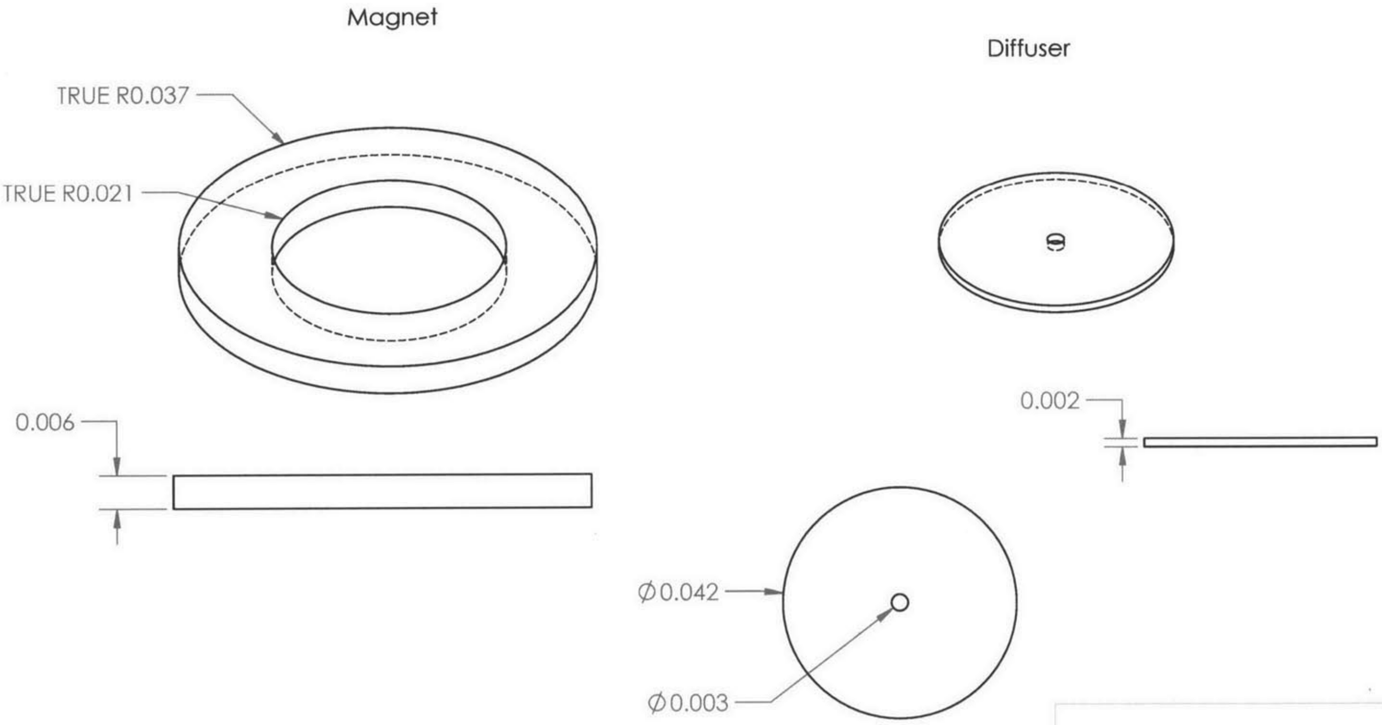

TITLE:

Magnets and Diffuser

SIZE A
DWG. NO. Assembly1
REV

SCALE: 1:1
WEIGHT:
SHEET 8 OF 10

Spacer

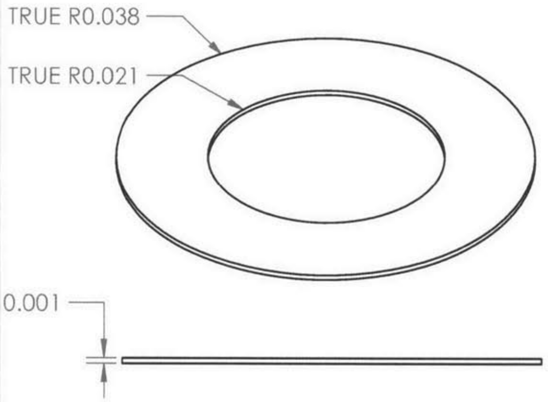

Top

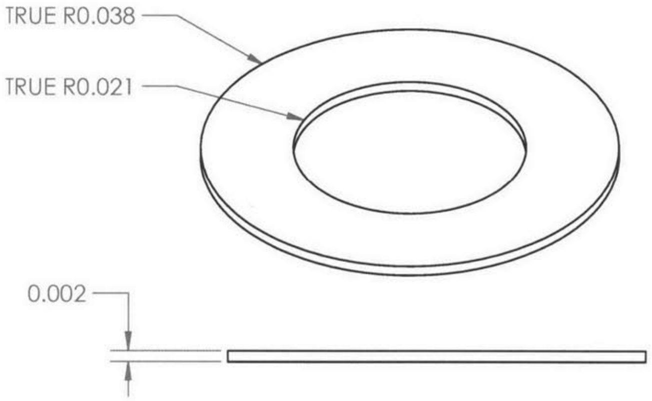

TITLE:
Aluminum Spacers

SIZE A
DWG. NO. Assembly1
REV
SCALE: 1:1
WEIGHT:
SHEET 9 OF 10

5 4 3 2 1

Steel Ring

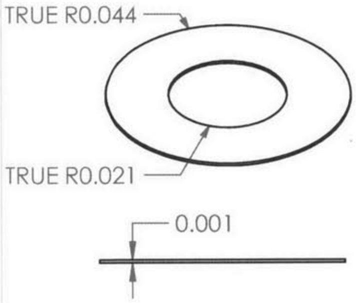

Steel Spacer

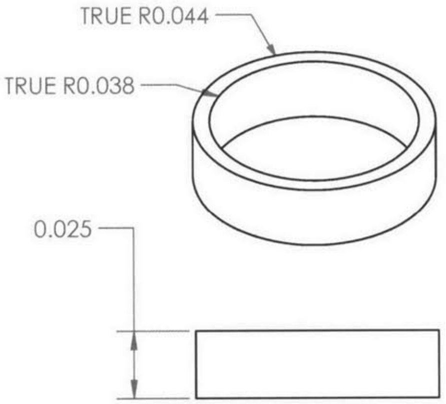

Steel Top

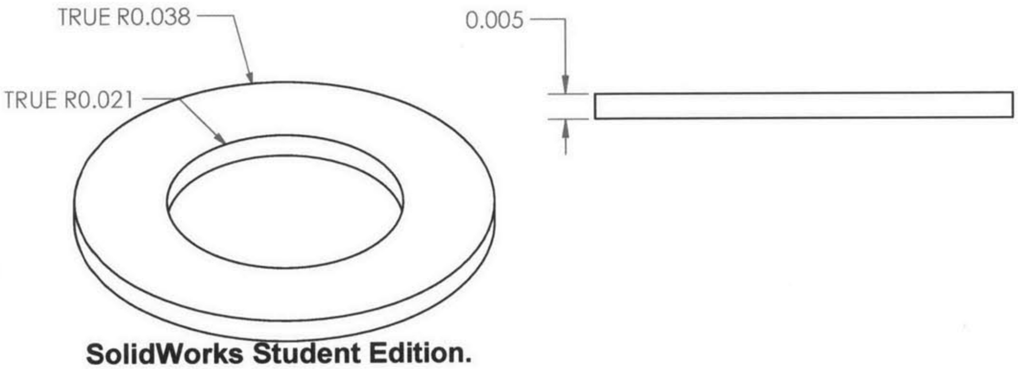

TITLE:

Steel Spacers

SIZE DWG. NO. REV
A Assembly1

SCALE: 1:2 WEIGHT: SHEET 10 OF 10

Appendix B

Instructions for CLASS Tandem Accelerator Operations

B.1 Accelerator Start-up Procedure

1. Check that the vent valves to the roughing pumps are closed.

2. Turn on the roughing pumps. If required, switch on the accelerator breaker. Note that there are separate breakers for the roughing pumps on the side of the accelerator, behind the source cabinets.

3. Plug in the cooling system, and open both cooling line valves at 45^o. Do not open the valves completely, as this will lead to large amount of condensation building up on the cooling lines.

4. Open the turbo-pump gate valves to pump down the accelerator. You may need to press the vacuum bypass button on the accelerator control panel.

5. Wait for the accelerator to reach rough vacuum (¡100 mTorr).

6. Turn on the turbo-pumps (42 kRPM).

7. Open low-energy (LE) gate valve (with turbopumps open)

B.2 Sputter Source Start-up Procedure

1. Make sure the gate valve for the sputter source is open, and that the valve to the sputter source roughing pump is closed. Note that the sputter source should always be under vacuum, even when the rest of the accelerator is up at atmosphere (it has its own roughing pump for this purpose)
2. Open HE gate valve.
3. Activate the Freon cooling system.
4. Open the valve to the nitrogen bottle to enable the stripper gas system. At this point all of the interlock lights on the main panel should be off.
5. Turn on the injector power. Doing so may trip the injector breaker (on the side of the accelerator, behind the source cabinets). Reset as needed, until lights on the injector panel turn on.
6. Turn on sputter source power.
7. Set the Cesium oven temperature to 120° C.
8. Turn on the grid lens and negative extraction (NE) voltage power supplies.
9. Set the target voltage, extraction voltage, and ionizer current slowly, until you reach the following values (approximate): $\mathrm{V}_N E = 12.5$ kV, $\mathrm{I}_i onizer = 20$ A, V_T=2.5kV.

B.3 Beam Extraction Procedure

1. Make sure that all gate valves are open and that you have high vacuum in all of the appropriate accelerator sections (¡ 5 $\mu torr$).
2. Set the voltage on the LE magnet supply to 30 V, then set Output On. This should put the supply in current control mode, with a voltage limit of 30V.

3. Turn the Y-steerer on.
4. Close the rough valve, open HV valves after the turbos set a proper pressure for the beam line
5. Set the magnet current to the desired value needed for the type of beam you want to create (2.1 A for protons, 7 A for lithium)
6. Check the beam current with the low energy (LE) Faraday cup.
7. Maximize the current read on the LE faraday by adjusting the gridded lens, LE magnet, and Y-steerer voltage and currents, accounting for the maximum allowable operating conditions (shown in Table 8.1).

Table B.1: Operating Settings for the CLASS Tandem Ion Accelerator

Operating Variable	**Maximum Value**
Temperature of Cesium Oven	150^o C
Target Voltage	3 kV
NE Voltage	15 kV
Low Energy Magnet Current	20 A
Gridded Lens Voltage	7.5 kV
Y-Steerer	100

8. Activate the magnet board, the oscillator controller and HV bias.
9. Set the acceleration voltage to the desired value. There should now be a current on the high energy Faraday cup (HEFC).
10. The HEFC current can be adjusted using the supplies listed in Step 7, and also by adjusting the X/Y source steerers, quadrupole, and tube lens settings.
11. To steer the beam into the beam line, use the HE steering magnet .
12. Maximize the current to the beam line FC using the beamline X/Y steerers, as well as all the other alignment-related techniques listed above.